EXIT PLANE PLASMA MEASUREMENTS OF A LOW-POWER HYDRAZINE ARCJET

BY

SCOTT ALLEN BUFTON

B.S., University of Illinois, 1988
M.S., University of Illinois, 1992

THESIS

Submitted in partial fulfillment of the requirements
for the degree of Doctor of Philosophy in Mechanical Engineering
in the Graduate College of the
University of Illinois at Urbana-Champaign, 1996

Urbana, Illinois

UNIVERSITY OF ILLINOIS AT URBANA-CHAMPAIGN

THE GRADUATE COLLEGE

JANUARY 1996

WE HEREBY RECOMMEND THAT THE THESIS BY

SCOTT ALLEN BUFTON

ENTITLED EXIT PLANE PLASMA MEASUREMENTS OF A LOW-POWER HYDRAZINE ARCJET

BE ACCEPTED IN PARTIAL FULFILLMENT OF THE REQUIREMENTS FOR THE DEGREE OF DOCTOR OF PHILOSOPHY

Rodney L. Burton
Director of Thesis Research

A. L. Addy
Head of Department

Committee on Final Examination†

Rodney L. Burton
Chairperson

Mark J. Kushner

† Required for doctor's degree but not for master's.

O-517

Abstract

Electric propulsion systems, and electrothermal arcjets in particular, have received considerable attention as viable systems for satellite propulsion applications. Research in this area has been fueled by recent applications of low-power arcjets aboard geosynchronous communications satellites. Recent advances made in low power (1-2 kW) arcjet numerical modeling, coupled with the demonstrated utility of arcjet thrusters, make the validation of computational models through experimentation increasingly important.

In this work, improved understanding of the flow processes in a 1-kW hydrazine constricted arcjet is achieved with multiple electrostatic probe surveys at the exit plane of a laboratory thruster. Quadruple, triple, and single electrostatic probe techniques are utilized for measurements of the electron temperature T_e, electron density n_e, and ratio of ion axial velocity to most probable thermal speed $u_i/c_{m,H^+}$. Three thruster specific power levels (19.8, 22.3, and 26.0 MJ/kg) are investigated by varying the thruster current and propellant mass flow rate. Centerline axial profiles of T_e and n_e are presented for 2.2 - 6.2 mm downstream of the exit plane, yielding $T_e \sim 7000$ K and $n_e \sim 3.6 \times 10^{12}$ cm^{-3} near the thruster exit for $P/\dot{m}$=22.4 MJ/kg.

Radial gradients in T_e and n_e for off-centerline measurement locations are shown to adversely affect the quadruple probe response in this region of the plume. The uniform plasma quadruple probe theory is modified to account for radial gradients in T_e and n_e over the probe radial dimension, and is used to extract exit plane radial T_e and n_e profiles from the raw probe data. These results indicate that the T_e radial profile is much wider than that of n_e at the thruster exit. Additionally, floating electrostatic probe measurements yield estimates of the radial electric-field profile at the thruster exit, implying

the presence of a small amount of the thruster current (~ 2%) and ohmic heating downstream of the arcjet exit plane.

A spatially-resolved time-of-flight electrostatic probe technique is developed and employed in this study for measurements of radial profiles of the plasma axial velocity u_i at the arcjet exit plane. Results indicate that the centerline axial velocities vary from 5.5 to 8.0 km/s over the 19.8-26.0 MJ/kg range of specific powers investigated. The quadruple probe results (T_e, n_e, u_i/c_m), coupled with these independent measurements of plasma velocity u_i, are used to determine the gas temperature T_g. These results reveal significant thermal nonequilibrium effects ($T_g/T_e<1$) at the thruster exit.

Exit plane probe measurements of n_e, T_e and T_g are compared with previously reported experimental data in the nozzle interior and thruster far-field plume. Finally, the results of this study are used to evaluate the performance of a comprehensive nitrogen-hydrogen arcjet model developed recently by Megli (1995). Comparisons of the experimental and predicted results indicate general agreement for the plasma parameters measured in this study.

Acknowledgments

As is often the case with work of this type, this research would have been impossible without the guidance and assistance of several individuals. Most of all, I am immensely indebted to my advisor, Professor Rodney L. Burton. His expertise in the area of electric propulsion, combined with his vast practical experience, made him invaluable in practically all aspects of this work. As a result of our interaction, I have benefited in many positive ways, both intellectually and professionally. I would also like to gratefully acknowledge the co-director of this research, Professor Herman Krier. I am certain that the quality of this research was much improved as a result of his many helpful suggestions and discussions regarding its scope.

Over the past few years I have been given the opportunity to work with several outstanding individuals who have had a positive influence on this research. For their many helpful discussions and assistance in the laboratory, I owe much gratitude to N. Tiliakos, G. Willmes, and T. Megli, who also provided the computational arcjet model results. Along the way, these individuals have become great friends as well as colleagues.

I am perhaps most indebted to my lovely wife, Tara. Her patience and the many sacrifices she has made throughout this work are practically without bound. I would also like to express immense gratitude to my parents, Richard and Ardis Bufton, who are ultimately responsible for making all of this happen. Without all of their hard work and dedication, I would never have had the opportunity to attempt to reach my goals. In addition, I owe a great deal of gratitude to my sister, Sheri, and brother, Steve, for their constant encouragement and support.

Throughout this research, I have enjoyed the friendship of many other people. My work would have been much more difficult without the

necessary balance between leisure and research that these individuals provided. They include: M. Doyle, S. Gordon, D. Jenkins, T. Megli, K. Smith, N. Tiliakos, G. Willmes, and many others. And finally, I am indebted to my best friend, M. Hites, for his sincere and unending friendship throughout the course of my graduate work. There is no finer gentleman, professional, or friend.

Support for this work was provided by the U. S. Air Force Office of Scientific Research, and their AASERT program, under contracts F49620-92-J-0448 and -0280. The program director is Dr. Mitat Birkan. Additionally, the teaching assistantship and fellowship support of the Department of Mechanical and Industrial Engineering is greatly appreciated. I gratefully acknowledge the 1-kW arcjet and PPU equipment provided by the Onboard Propulsion Branch of the NASA Lewis Research Center. J. Hamley of NASA LeRC deserves recognition for his assistance with the TOF current pulse circuitry. I also acknowledge the many artisans in the machine shops of the TAM and MIE departments, who so skillfully fabricated several aspects of the experimental hardware used in this work.

To those who have, in jest, questioned the longevity of my tenure as a student, I offer the following quotation. Unfortunately, it took me several long years to realize that Mr. Dewey intended a deeper meaning!

"Education is not preparation for life, education is life itself."

-- John Dewey

Table of Contents

List of Symbols

A	Electrode geometric surface area [m^2]
c_m	Most probable thermal speed [m/s]
E	Electric field [V/m]
e	Electron charge [coulombs]
f	Ion composition parameter ($=n_{H+}/n_e$)
g_o	Gravitational constant [m/s^2]
I	Probe electrode current [A]
I_{arc}	Arcjet operating current [A]
I_b	Bohm electrode ion current [A]
I_{sp}	Thruster specific impulse [s]
I_t	Current collected at electrode tip [A]
j	Current density [A/m^2]
j_e	Electron saturation current density [A/m^2]
j_i	Ion saturation current density [A/m^2]
k	Boltzmann constant [J/K]
L	Cylindrical electrode length [mm]
m	Particle mass [kg]
$\dot{m}$	Propellant flow rate [mg/s]
n	Particle density [cm^{-3}]
n_{Bohm}	Ion density at Bohm sheath/presheath edge [cm^{-3}]
n_o	Ion, electron density in the undisturbed plasma [cm^{-3}]
P	Thruster power [kW]
P_k	Designation for electrode "k"
Q	Collision cross section [m^2]
R	Resistance [Ω]
r	Radial distance from thruster centerline [mm]

r_p	Electrode radius [mm]
s	Electrode clearance [mm]
T	Temperature [K, eV]
t	Time [s, μs]
u	Bulk gas velocity [m/s]
u_e	Thruster exhaust velocity [m/s]
u_i	Ion flow velocity [m/s]
V	Probe electrode voltage [Volts]
V_{arc}	Arcjet operating voltage [Volts]
V_d	Electrode relative bias voltage [Volts]
V_f	Floating electrode voltage [Volts]
V_{out}	Current transducer output [Volts]
V_p	Plasma potential [Volts]
V_{pot}	Probe position signal [Volts]
V_s	Sheath potential [Volts]
V_t	Propellant calibration tank volume [cm^3]
v	Particle thermal speed [m/s]
v_{Bohm}	Bohm ion velocity [m/s]
x	Axial distance from thruster exit [mm]
x_p	Probe translational location [mm]
x_{H^+, N^+}	Wake effect collection area parameters

Greek

α	Ionization fraction
δ	Flow divergence angle [Degrees]
ε_d	Dissociation energy [eV]
ε	Emissivity
Γ	Mathematical Gamma function

γ	Ratio of specific heats
θ	Probe angle [Degrees]
κ	Correction to n_e from N^+ ions
μ	Equal to $(m_{H+}/m_{N+})^{1/2}$
τ_L	Electrode "end effect" parameter
λ_D	Debye length [m]
λ_{mfp}	Collision mean free path [m]
σ	Plasma conductivity [mho/m], Standard deviation [mm]
Φ_{Bohm}	Bohm potential drop [Volts]
ϕ	Equal to e/kT_e, $[V^{-1}]$

Subscripts

a	Anode surface
e,i,n	Electron, ion, neutral species
g	Gas
m	Measured quantity
r	Radial
1,2,3,4	Electrode designation

1. Introduction and Background

1.1 Electric Propulsion Background

The majority of space propulsion techniques generate thrust by heating a propellant and subsequently converting thermal energy to kinetic energy via a gas dynamic expansion through a nozzle. These techniques differ, however, in the physical mechanisms used to heat the propellant. For example, conventional chemical propulsion systems like the Space Shuttle main engines and solid rocket boosters utilize exothermic combustion reactions to heat the propellant and generate thrust by expelling combustion products. Electric propulsion systems, on the other hand, rely on "the acceleration of gases for propulsion by electrical heating and/or by electric and magnetic body forces" (Jahn, 1968). The research presented here concerns the arcjet thruster, which is an electric propulsion device that heats a gaseous propellant by passing it through a constricted arc discharge located in the throat of a supersonic nozzle.

1.1.1 Electric Propulsion Historical Perspective

The concept of using electrical energy to generate thrust for spacecraft was first envisioned by Robert H. Goddard in 1906, who left the task of achieving "scientific respectability" of electric propulsion systems to others (Wilbur, et al., 1991). In the decades that followed, Herman Oberth and Ernst Stuhlinger demonstrated that practical electric propulsion technologies offered respectable performance gains over the conventional systems of the time (Wilbur, et al., 1991). Investigations of electric propulsion devices continued into the 1960s, at which time research and development fell drastically. This was presumably due to several reasons, including: 1) the

prohibitive size and mass requirements placed on the spacecraft by electrical power supplies, 2) incompatibility with existing or proposed fuel storage systems, and 3) policy decisions of the era.

Recent years have seen a resurgence in electric propulsion research and application, owing to gains in electrical power technology, including drastic improvements in power supply size and efficiency, energy storage, and solar array technology. Additionally, arcjets operating on hydrazine decomposition products are compatible with current satellite propulsion systems, which presently use this fuel for conventional propulsion systems. Thus, modification of existing propellant storage and delivery systems is not required in order to apply hydrazine-fed electric propulsion devices to existing systems. Advances in electric propulsion technologies are further fueled by the improved propulsion system performance demanded by the evolution of the commercial communications satellite industry (Wilbur, 1991). The utility and reliability of arcjet systems was recently demonstrated, with the 1994 launch of the Telstar 401 satellite, which uses arcjets for North-South station keeping duties (Butler, et al., 1994).

1.1.2 Why Use Electric Propulsion?

The primary goal of all propulsion systems is to produce useful thrust by exhausting propellant at a relatively high velocity and hence, momentum. The useful thrust derived by such a process is given by $T \approx \dot{m}u = \dot{m}\, g_o\, I_{sp}$, where I_{sp} is the specific impulse of the thruster device and propellant combination. I_{sp} is also given by $I_{sp}=u/g_o$ and can be thought of as the thrust force per unit weight of propellant flow. It can be shown that $I_{sp} \sim \sqrt{T_o/MW}$, where T_o is the effective chamber stagnation temperature and MW is the

molecular weight of the propellant (Sutton, 1986). Chemical propulsion systems, due to the relatively low values of T_o (< 4000 K) and high values of MW and mass flow associated with them, are very low I_{sp} and high thrust devices. This makes them best suited for lifting large payloads into space, where large amounts of thrust are required for relatively short durations. Electric propulsion devices, however, are capable of much higher T_o, while using lower MW propellants. This leads to very high specific impulses, but very low thrust levels despite the high propellant exit velocities attainable. The I_{sp} and thrust associated with electric propulsion devices makes them attractive for orbit transfer and station keeping duties for satellites where low levels of thrust are required over the long life of the spacecraft. These arguments are summarized by Fig. 1.1, which shows the thrust-to-weight ratio versus I_{sp} for various propulsion systems (Miller, 1994 and Megli, 1995).

1.2 Arcjet Description and Key Physics

A schematic of a constricted arcjet of the type used for this research is shown in Fig. 1.2. The throat diameter is ~0.7 mm and the exit plane diameter is ~10 mm, which corresponds to an area ratio of 225 and a nozzle half-angle of 20° in the diverging section. The propellant is heated by a wall and vortex-stabilized arc discharge of ~100 V and ~10 A (power ~ 1 kW). The arc is constricted in the throat and attaches diffusely in the diverging section of the nozzle. The propellant, which is injected upstream of the cathode with an azimuthal swirl, consists of a gaseous mixture of nitrogen and hydrogen, simulating hydrazine (N_2H_4) decomposition products. The propellant mass flow rate for this device is nominally 30-60 mg/s. Typical performance

parameters for this type of device are ~0.1 - 0.2 N of thrust, 500 seconds I_{sp}, and a thrust efficiency of ~35%.

Energy is transferred to the gas in the arc via ohmic heating, with energy dissipation occurring as a result of electron collisions with the neutral and ionized propellant species. The high pressures near the inlet and in the throat (~1 atm) constrict the arc and decrease the mean free path for electron collisions with other species. This high current density at the core of the constrictor (~5 x 10^7 A/m^2) allows enough electron-heavy particle collisions that thermal equilibrium (T_e=T_i) exists in this region. These collisions act to decelerate the electrons, which are continually accelerated by the E-field imposed across the anode-cathode gap. Temperatures in the arcjet range from ~20,000 K near the cathode tip to ~1,500 K near the anode wall.

As the plasma flow enters the diverging section of the nozzle, the energy-addition mode shifts from that due to electron collisions to energy addition through recombination reactions. Additionally, the decreasing pressure in this region does not allow enough collisional coupling between the electrons and the heavy particles to cause thermal equilibrium. The above energy transfer processes tend to increase the bulk temperature of the plasma and this thermal energy is converted to kinetic energy through a rapid gas dynamic expansion process.

The thrust efficiency of these low power devices is typically ~35%, due to several energy loss mechanisms. Thermal energy is lost by conduction to the anode block and by thermal radiation losses to the space environment. Additionally, the expansion process is dominated by very thick (~1-2 mm) viscous boundary layers, a consequence of high gas temperatures, low pressures, and the small geometry of the thruster. Other causes of low arcjet

efficiencies are based on nonequilibrium effects. Thermal nonequilibrium ($T_e > T_i$) in the plasma flow represents an "incomplete" energy transfer process between high kinetic temperature electrons and lower kinetic temperature ions and neutral particles. High energy electrons that are exhausted from the thruster represent energy unavailable for conversion to useful thrust.

Some of the energy transferred to the propellant via electron collisions with neutrals is invested in electronic excitation, and molecular dissociation, vibration, and ionization. Because of the large propellant velocities in the arcjet (several km/s) and the small nozzle length (~ 1 cm), the particle residence time is on the order of 1 μs, which is less than the characteristic time required for particle recombination. This leads to a strong chemical nonequilibrium effect in the arcjet, since energy lost to ionization, dissociation and other internal modes is not available for useful thrust. These chemical nonequilibrium losses have been termed "frozen flow" losses, because the energy invested is frozen in the flow as a consequence of the short particle residence times. By some estimates, frozen flow losses may be responsible for 30-40% of the total energy input to the arcjet, or ~350 W in a 1 kW arcjet (Jack, 1961).

This work presents the results of an experimental investigation of the exit plane region of a 1-kW hydrazine arcjet plasma. Electrostatic probe diagnostics are utilized to measure electron temperatures, electron densities, plasma axial velocities, and bulk gas temperatures for the region between 2.2 and 6.2 mm downstream of the thruster exit plane. These parameters are measured over a range of thruster operating conditions by varying the thruster current and flowrate. The results of this work are compared with

previous experimental data and numerical model predictions as discussed in Chapter 6.

1.3 Literature Review

The following literature review has been divided into two sections. Included in section 1.3.1 is a general discussion of the development history of the electrostatic probing techniques utilized in this study. Additionally, a review of relevant previous research in which electrostatic probe techniques have been used for measurements in low-power arcjets is presented. In section 1.3.2, a summary of other relevant experimental techniques is presented. These techniques are primarily non-intrusive and optical in nature, and generally have been applied to low or medium power arcjets similar in to the 1-kW thruster investigated in this study.

1.3.1 Previous Electrostatic Probe Research

Electrostatic probes have found much use in experimentally determining plasma parameters in space and laboratory plasmas, both to investigate arcjet efficiency and to validate numerical models. Electrostatic probes were originally developed and used to measure plasma parameters by Langmuir and Mott-Smith (1926). Since that time, *single* electrostatic probes operating under certain conditions (see section 3.1.3) have come to be known as Langmuir probes or "classical Langmuir probes." A discussion of the theory behind Langmuir probes and the multiple probe systems (crossed, triple, and quadruple probes) referred to below is presented in Chapter 3.

Several authors have employed classical Langmuir single probes in the characterization of low-power arcjet plumes. Carney and Keith (1989), Carney and Sankovic (1989), Sankovic (1990), and Sankovic and Jankovsky (1990)

have all utilized single Langmuir probes at various locations in the plume of a 1-kW hydrazine arcjet. Two of these works, Carney and Sankovic (1989) and Sankovic (1990), correspond to conditions similar to those examined in the present study. Although these data do not correspond to the locations examined in this study, they help establish the extent of axial gradients in T_e and n_e downstream of the thruster exit when compared with data acquired in this study. Single Langmuir probes have also been implemented in 1-kW hydrogen arcjet plumes by Gallimore, et al. (1994). Although a vast majority of Langmuir probes are applied to the free stream plasma plume, their use is not limited to this region. Single Langmuir probes are currently being implemented in the *interior* of low-power hydrazine arcjets by Tiliakos, Burton and Krier (1995). They have mounted small planar probes in the nozzle of a modified 1-kW thruster for the purpose of measuring the T_e and n_e distributions along the wall of the diverging section of the thruster.

While single probes are appealing due to their relatively simple construction, interpreting the probe V-I characteristic (see section 3.1.2) can be unwieldy. A viable alternative is the triple electrostatic probe, which was developed by Chen and Sekiguchi (1965). The triple probe allows simultaneous measurement of T_e and n_e without the necessity of a voltage sweep and generation of a corresponding probe V-I characteristic. The utility of triple probes for electric propulsion devices has recently been demonstrated in MPD thruster plumes by Tilley, et al. (1990), Gallimore, et al. (1992), and Paccani (1994). Triple electrostatic probes have also been implemented in the plume of a 1-kW hydrogen thruster by Pobst, et al. (1993). Additionally, a comprehensive general review of electrostatic probe techniques and their

uses in electric propulsion devices has recently been presented by Habiger, et al. (1993).

In the work by Kanal (1964), it was shown theoretically that the current collected by a single cylindrical probe in a flowing plasma was a function of, among other plasma parameters, the angle θ between the probe and the quantity u_i/c_m (= plasma velocity/ion most probable thermal speed). The expressions derived by Kanal were manipulated by Johnson and Murphree (1969) for the limit of thin sheaths. They noted that the analytical expression for the ratio of the measured current collected by two equally biased orthogonal probes (θ=0°, θ=90°) was a function of the quantity u_i/c_m only. This technique of measuring u_i/c_m is called the crossed probe technique. Since its inception, this technique has been used on numerous occasions to measure the ion speed ratio u_i/c_m (Johnson and Murphree, 1969, Poissant and Dudeck, 1985). More recently, Habiger, et al. (1993) have used this technique in an argon MPD thruster.

The quadruple electrostatic probe, which was originally developed by Burton, et al. (1993) and DelMedico (1992), combines the crossed probe and triple probe techniques for simultaneous measurements of T_e, n_e, and the ion speed ratio u_i/c_m. The utility of the quadruple probe has been demonstrated in an MPD thruster by Burton, et al. (1993).

All of the quadruple and triple probe studies discussed above were for plasmas in which only one species of ion existed and was collected by the probe electrodes (i.e., argon or hydrogen plasmas). The nitrogen-hydrogen plasma probed in this study, however, consists of two species of ions (N^+ and H^+). The quadruple probe theory discussed above has been modified for the present study to account for the presence of more than one species of ion.

Additionally, previous uses of quadruple and triple probes have been in plasmas for which gradients in T_e and n_e over the probe dimensions can be neglected. This, in fact, is not the case for the region of the 1-kW hydrazine arcjet plume investigated in this study. As discussed in section 4.2, the effect of these gradients has been identified and accounted for by modifications made to the theory for the present study. Preliminary results of the analyses described in this study have been presented in Burton, et al. (1994 and 1995), and Bufton, et al. (1995).

1.3.2 Previous Experimental Arcjet Investigations

Low-cost diagnostic techniques like the electrostatic probe techniques described above have been used in electric propulsion research for years. Recent technological advances, however, coupled with a renewed interest in electric propulsion for flight applications, have triggered an abundance of experimental research on low power arcjets using advanced optical and other non-intrusive probing techniques. While these techniques have a large monetary overhead associated with them, they still have several advantages over electrostatic probing techniques, including: 1) they generally do not perturb the flow, and 2) the experimental uncertainties associated with them can be much smaller that those associated with electrostatic probing techniques. Several recent studies have applied these non-intrusive techniques to hydrogen and ammonia arcjets. However, as discussed below in terms of the motivations and objectives of this research, very little research has been conducted on hydrazine thrusters in addition to the electrostatic probe work discussed in section 1.3.1.

To date, the research by Zube and Myers (1992, 1993) remains one of the only works to perform a comprehensive study of the state of the plasma in a low-power *hydrazine* arcjet. They used emission spectroscopy techniques to H, NI, and NII excitation temperatures, N_2 vibrational and N_2 rotational temperatures, and electron number densities inside the diverging section of a NASA Lewis Research Center 1-kW arcjet. Optical access to the thruster interior was provided by a series of 0.25 mm diameter holes drilled through the nozzle block along the 12 mm length of the diverging section. They noted that thermal nonequilibrium was significant among the heavy particle species as well as between the heavy particles and the electrons. A similar approach was undertaken by Hargus, Micci, and Spores (1994), who applied emission spectroscopy to the interior nozzle region of a 26-kW class *ammonia* thruster. Like the study by Zube and Myers (1993), access was provided to the thruster interior via a series of small holes bored through the nozzle block. Hargus, et al. measured H and NII excitation temperatures, NH vibrational and rotational temperatures, and electron density at several axial locations in the nozzle diverging section.

Zube and Auweter-Kurtz (1993) and Zube and Messerschmid (1994) also employed emission spectroscopic techniques in their study of the plume of a 1.6-kW thruster of a different design than the thruster utilized in the present study. Results for hydrazine arcjets have also been presented by Habiger, et al. (1994) and Golz, et al. (1994), who utilized Fabry-Perot interferometry to measure translational temperatures and velocities in the thruster plume. The experiments, however, were conducted with a 100-kW class arcjet operating at very large specific powers. Fabry-Perot interferometry

was also used by Pivirotto (1986) for measurements near the exit plane of a 20-kW hydrogen thruster.

Emission spectroscopy studies were also conducted by Ruyten, Burtner, and Keefer (1993) near the exit plane a 1-kW arcjet operating on simulated *ammonia* propellant. They inferred heavy particle velocities by measuring Doppler shifts of hydrogen Balmer emission lines. Since their measurements were "line-of-sight," the measured velocity data represented an average velocity along the line-of sight. Cross-section averaged kinetic temperatures and electron densities were also determined, based on the line shape of the observed hydrogen Balmer-alpha radiation.

The group consisting of Burtner, Keefer, and Ruyten (1994) has also conducted research on 1-kW *ammonia* thrusters using the Laser Induced Fluorescence (LIF) technique. They measured heavy particle temperatures and exit plane profiles of the axial and radial velocities of atomic nitrogen and hydrogen. Results showed velocity slip between the N and H species, with the atomic nitrogen axial velocity ~ 9% larger than that of atomic hydrogen. Conversely, the measured hydrogen radial velocities were larger than those for nitrogen, indicating that the atomic hydrogen species expand radially much faster than the atomic nitrogen species. Liebeskind, Hanson, and Cappelli (1995) also investigated velocity slip in a 1-kW arcjet via LIF measurements. Their study, however, focused on a *hydrogen* arcjet. Liebeskind, et al. "seeded" the thruster propellant with small amounts of helium gas and measured the Doppler shifted fluorescence spectra of both He and H. They noted that the upper limit of the slip between the two probed species was ~2%, which was also the uncertainty of the velocity measurements. They also noted that the measured kinetic temperatures of H

and He were within 6%. Considering the 20% uncertainty in these measurements, Liebeskind, et al. were able to conclude that all species shared a common kinetic temperature.

Several other research efforts have utilized LIF to measure H species translational temperatures and velocities at the exit plane of a 1-kW hydrogen arcjet of the NASA Lewis Research Center design. Among recent efforts are those of Liebeskind, Hanson, and Cappelli (1992), who originally applied the LIF technique to arcjets, and Pobst, Wysong, and Spores (1995a, 1995b). The work of Liebeskind, et al. has been extended by Storm and Cappelli (1995) to yield velocity and temperature measurements inside the arcjet nozzle, between the near-constrictor region and the exit plane. These measurements were made through the nozzle exit plane rather than through radial holes in the nozzle as in the work by Zube and Myers (1993) and Hargus, et al. (1994). Using this "end on" approach to probing the hydrogen arcjet interior in an earlier emission spectroscopy study, Storm and Cappelli (1994) measured the operating temperature of the cathode tip in a 1-kW hydrogen arcjet. They found that the steady state cathode tip temperature was within 400 K of the melting point of the tungsten cathode (~ 3700 K).

Other non-intrusive plasma diagnostic techniques are currently being used to measure species densities in arcjet plumes. Ohler, Gilchrist, and Gallimore (1994) have recently presented the results of electron number density measurements in the far-field plume of a 1-kW hydrogen thruster using microwave interferometry. Additionally, Pobst, et al. (1994) are currently adapting a pulsed electron beam fluorescence technique for measurements of atomic ground state number densities in hydrogen arcjet plumes.

A velocity measurement technique called Current Modulation Velocimetry (CMV) has recently been developed and implemented on a 1-kW hydrogen arcjet by Pobst, et al. (1994). In this technique, a short duration current pulse is superimposed on the arcjet steady state operating current. The effect of this pulse is to cause a momentary change in the emission characteristics of the tagged flow, which is monitored optically at two axial locations in the plume. The plasma velocity is inferred by relating the time required for tagged plasma to traverse the two measurement locations to the axial separation of the detectors. This technique follows from the Emission Ripple Velocimetry (ERV) technique developed by Spores, et al. (1992) in which plasma velocities were inferred by monitoring natural fluctuations in the plasma emission. The time-of-flight (TOF) electrostatic probe technique utilized in the present study is based on techniques developed in the CMV work by Pobst, et al. (1994). Details of the CMV technique are discussed at length in section 4.3.1.

Velocities have also been measured in electric propulsion devices using time-of-flight (TOF) electrostatic probes. Hoell, et al. (1971) used two individual double probes separated by 15 cm to measure ion velocities in an MPD thruster. More recently, Habiger, et al. (1993) have also used two double electrostatic probes to measure plasma velocities. Time-of-flight velocimetry techniques have been applied to 100-kW hydrogen arcjets by Golz, et al. (1994). In that study, they also utilized two individual double probes. A time-of-flight velocimetry technique is also used in the present study. However, the technique used for this work differs from those discussed above in that the "double probe" configuration is not utilized. This is due to finite size constraints place on the TOF probe size by the small area of the plasma probed

in this study. Instead two individual electrodes, separated by only 5 mm, each collect saturation current. Fluctuations in the plasma are reflected in variations in the collected current, with the fluctuations in the downstream electrode signal being delayed in time from the those apparent on the upstream signal. This time delay, along with the axial separation of the two electrodes, is used to determine the average plasma velocity between the electrodes. The development of this technique is discussed at length in section 4.3. Preliminary results demonstrating the feasibility of this technique have recently been presented by Bufton, Burton and Krier (1995).

1.4 Motivations and Objectives of this Research

Despite the maturity of electric propulsion technologies and the deceptively simple operation of the arcjet, some of the fundamental physics of arcjet operation remain poorly understood. Additionally, many areas of arcjet operation have received little attention, and some regions of the arcjet plasma have very little documentation in terms of even fundamental plasma parameters. As discussed above, several aspects of arcjet operation are currently being experimentally investigated by a variety of authors. Many computational arcjet models have also been, or are currently being, developed in an effort to model the complex phenomena associated with arcjets. The author is of the opinion that a comprehensive understanding of the arcjet can be most efficiently realized through concurrent and interactive experimental and computational efforts.

Concurrent to the experimental research conducted in this study, a comprehensive arcjet computational model was developed and implemented by Megli, Krier and Burton (1994, 1995). However, a limited amount of

experimental data exists in the literature with which to gauge the performance of this model for nitrogen-hydrogen plasmas. One of the primary objectives of this research concerns validating the performance of this numerical model. This research will serve two purposes in this regard. First, measurements of basic plasma parameters (i.e., densities, temperatures, and velocities) will be compared with model predictions at the exit plane to evaluate the model performance. Second, measurements will be used to help validate and choose the model boundary conditions at the nozzle exit (e.g., the current distribution boundary condition at the exit).

An abundance of experimental results have been presented for low-power arcjets of the type used in this study for *hydrogen* propellant. However, a review of recent literature reveals that, despite several decades of research and development, surprisingly little data for fundamental plasma parameters exist in the very near-field plume (within 10 mm of the exit plane) of low-power *hydrazine* arcjets. It is a goal of this research to add to the base of experimental results in this area. In doing so, it is a further goal of this study to demonstrate feasibility and utility of low-cost but robust electrostatic probing techniques at the exit plane of a 1-kW arcjet.

These goals are accomplished by implementing a variety of electrostatic probe systems to simultaneously measure radial profiles of plasma parameters near the thruster exit plane. A quadruple probe technique, significantly modified for the present study, is utilized to measure T_e, n_e, and the ion speed ratio $u_i/c_{m,H^+}$. Additionally, a time-of-flight electrostatic probe technique is developed for this study and implemented to make measurements of plasma axial velocity at the thruster exit. The quadruple probe and time-of-flight probe results are combined to yield estimates of the

gas temperature T_g. Finally, the thruster operating condition is varied to study the effect of thruster current and propellant flow rate on these measurements.

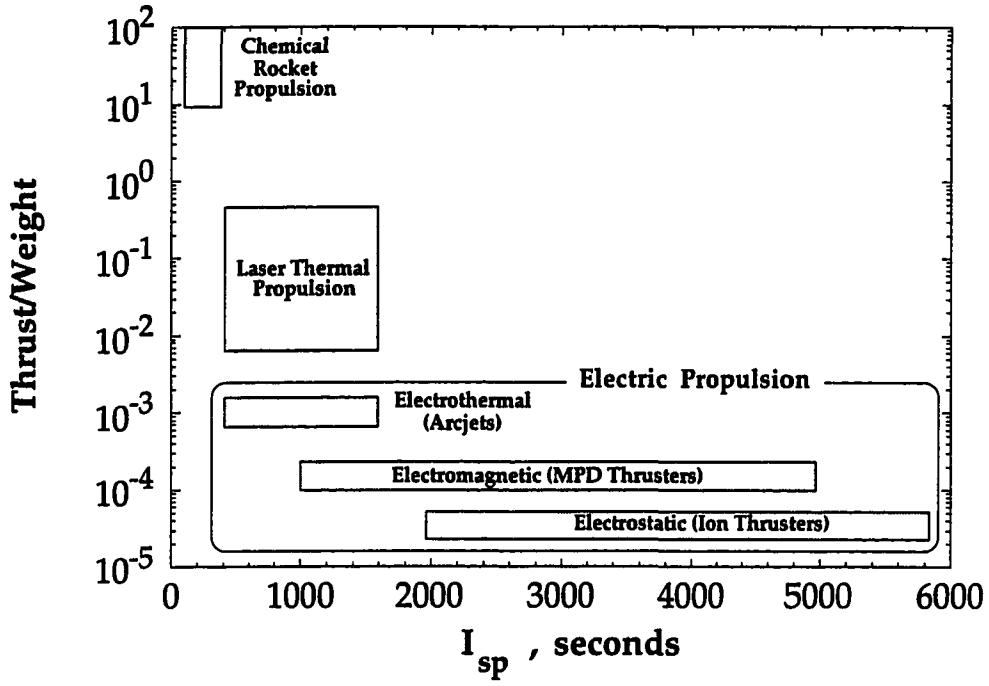

Fig. 1.1 Thrust/weight ratio versus specific impulse I_{sp} for several types of thrust systems [from Miller (1994) and Megli (1995)].

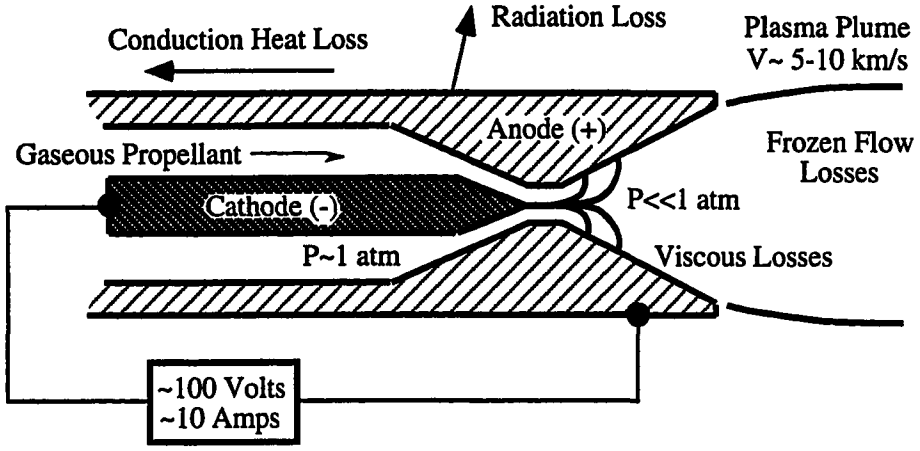

Fig. 1.2 General schematic view of a 1-kW electrothermal arcjet thruster.

2. Experimental Apparatus and Approach

2.1 Arcjet Thruster

The arcjet thruster utilized in this study is a laboratory model thruster that was designed and fabricated by NASA Lewis Research Center (NASA LeRC). To facilitate standardization of experimental research on this type of thruster, the standard NASA LeRC design is used for arcjet experiments at several research institutions. This thruster is nominally a 1-kW device operating at approximately 10 amps and 100 volts, and is commonly utilized with gaseous hydrogen, nitrogen, ammonia, or hydrazine propellant. A description of the thruster nozzle region is presented below. A more complete description of the NASA LeRC 1-kW thruster is given by Curran, et al. (1992).

2.1.1 Thruster Geometry

A schematic of the nozzle region of the thruster used in this study is shown in Fig. 2.1. The nozzle (anode) is manufactured from a 2% thoriated tungsten alloy. The nozzle half-angle in the diverging section is 20° and the half-angle of the upstream converging section is 30°. The constrictor (throat) diameter and length are 0.63 mm (0.025 inches) and 0.25 mm (0.010 inches), respectively. The exit plane diameter is 9.52 mm (0.375 inches), resulting in a nozzle area ratio of 225:1.

The cathode, which has a diameter of 3.18 mm (0.125 inches), is also fabricated from 2% thoriated tungsten. The cathode tip, like the converging (upstream) section of the nozzle, has a 30° half angle. The arc gap between the anode and cathode is set by forcing the cathode against the anode and backing the cathode up 0.58 mm (0.023 inches) before securely locking it in place. An

"as machined" cathode has a sharp point machined on it which will erode slightly during use as the cathode tip shortens due the high temperatures and erosion at the point of cathode arc emission. This has been experimentally substantiated by Storm and Cappelli (1994), who measured cathode tip temperatures in 1- and 5-kW hydrogen arcjets that were at or very near the melting temperature of tungsten (3700 K).

The thruster operates on gaseous propellant, which is introduced to the arcjet upstream of the boron nitride insulator shown in Fig. 2.1. After passing between the insulator and anode housing, the propellant passes through the propellant injection disk. The purpose of this disk is to inject the gaseous propellant tangentially upstream of the nozzle throat and cathode tip so that it has a "swirl" or azimuthal component. This is done via two diametrically opposed 0.51 mm holes that are tangential to the hole through which the cathode passes. It was originally believed that this tended to stabilize and make symmetric the arc in the constrictor region, although opinions are generally divided as to whether or not the so-called propellant swirl is necessary or beneficial for stable thruster operation. The gas paths are sealed from the ambient vacuum conditions surrounding the thruster by graphite foil gaskets (Fig. 2.1).

2.1.2 Thruster and Power Supply Operation

During this study, the thruster shown in Fig. 2.1 was operated with the anode electrically grounded to the facility ground and the cathode operating at the negative arc voltage, nominally -100 volts. This was done primarily for safety reasons as well as to minimize the amount of electrical noise

introduced to the signals of electrostatic probes that were in close proximity to the arcjet nozzle exit plane.

For a given thruster geometry and propellant composition, the arcjet steady state operating characteristics are determined only by the arc current I_{arc}, which is operator specified and regulated by the arcjet power processing unit (PPU) discussed below. The arc voltage V_{arc} is determined by I_{arc} and the plasma in the nozzle region and is a measured quantity. For all experimental results presented in this study, the thruster operated on gaseous mixtures of hydrogen and nitrogen gas in the ratio H_2:N_2 = 2:1 to simulated fully decomposed hydrazine propellant. In this study, three thruster operating conditions were utilized by varying the propellant mass flow rate $\dot{m}$ and arc current I_{arc} as shown below in Table 2.1. These operating conditions yielded a range of thruster specific power $P/\dot{m}$ as discussed in section 5.1.1 and shown in Table 2.1.

Operating Condition	$\dot{m}$ (mg/s)	I_{arc} (amps)	$P/\dot{m}$ (MJ/kg)
1	60.0	10.0	19.8
2	50.0	10.0	22.4
3	45.0	11.0	26.0

Table 2.1 Summary of arcjet operating conditions used in this study. The externally set parameters for arcjet performance are the arcjet current I_{arc} and the propellant mass flow rate $\dot{m}$.

Power was supplied to the arcjet by a power processing unit (PPU), which was also supplied by NASA Lewis Research Center. With this unit, the amount of electrical current supplied to the arcjet can be specified as an

input. For a specified arc current I_{arc}, the thruster voltage is determined by the impedance of the arcjet plasma, which is nominally 10 Ω.

Due to the switching nature of the PPU electronics, the current supplied to the arcjet has an ac "ripple" associated with it. This ripple has a frequency of 15-20 kHz and results in fluctuations in the arc current that are ±8% about the mean. Typical traces for the steady state arcjet operating current and voltage are shown in Fig. 2.2. The 180° phase difference between I_{arc} and V_{arc} is a consequence of the "negative impedance" characteristic of the arcjet. The plasma resistance, which varies inversely with the plasma electron density, decreases as I_{arc} and the number of energetic electrons available for ionizing collisions increases. Since the plasma resistance decreases faster than the arc current increases, the arc voltage also decreases with increasing I_{arc}. Figure 2.3 shows the arcjet power P_{arc} (= $I_{arc}V_{arc}$) versus time and demonstrates that the arc power is in phase with the PPU current ripple. This inherent PPU ripple can be important when making "steady-state" plasma diagnostics measurements of the arcjet. As discussed in section 5.3.1, this effect must be considered with the exit plane electrostatic probe diagnostics utilized in this study.

2.2 Plasma Diagnostic Techniques Utilized in this Study

A vast majority of recent investigations of the arcjet exit plane and plume region have utilized optical and laser based methods to make measurements of electron density, bulk gas temperature, and plasma component velocities. Although these techniques are very attractive because they are non-intrusive, they can be very costly and difficult to set-up and utilize in a laboratory environment. In this study, electrostatic probing

techniques are utilized to make measurements of plasma parameters at the exit plane region of the 1 kW hydrazine arcjet. Although these techniques are physically intrusive, measurement uncertainties can be reduced to acceptable levels through careful consideration of fundamental electrostatic probe assumptions as discussed in Chapter 3. This fact, combined with the low cost and robust qualities of these probes makes them attractive for use in this research.

Two types of electrostatic probe techniques are utilized in this study: 1) the quadruple electrostatic probe, and 2) the time-of-flight (TOF) electrostatic probe. Both of these probes, as they are utilized in this research, are summarized below and discussed at length in Chapter 4. The quadruple probe is used to make simultaneous measurements of electron temperature T_e, electron density n_e, and the ion speed ratio u_i/c_m (ion velocity/ion most probable thermal speed), while the TOF probe yields measurements of the bulk plasma velocity u_i. Measurements of the plasma velocity and the ion speed ratio are combined to yield estimates of the bulk gas temperature T_g. Both of these probes are used in this study swept across the thruster exit plane to make radial surveys of the exit plane plume region, resulting in radial profiles of the plasma parameters discussed above. Additionally, the quadruple probe is used to measure the axial centerline profile of T_e and n_e in the region downstream of the nozzle exit. Both the quadruple probe and the TOF probe are mounted on a mechanical linear translation carriage, allowing the radial and axial variation of probe location as discussed above. This mechanism is discussed in detail in section 2.3.4.

2.3 Quadruple Electrostatic Probe

The quadruple probe, which was originally developed by Burton, et al. (1993), is comprised of four individual plasma-sensing electrodes. It combines the three parallel electrodes of the triple probe (Chen and Sekiguchi, 1965) with an additional electrode that is orthogonal, or perpendicular, to the other three. The perpendicular electrode, when used in conjunction with one of the three parallel electrodes at the same bias potential, comprises a crossed probe for the determination of the ion speed ratio (Johnson and Murphree, 1969). The ion speed ratio can be measured simultaneously with the electron temperature and electron density, which are determined via the triple probe portion of the quadruple probe. The physical dimensions of the quadruple probe used in this study are presented below.

2.3.1 Quadruple Probe Geometry and Construction

A schematic of the sensing tip of the quadruple probe used in this study is shown in Fig. 2.4. The probe is comprised of 4 individual tungsten wire electrodes of 0.25 mm diameter with an exposed length of 2.5 mm for electrodes 1-3 and 2.0 mm for electrode 4. Tungsten probe electrodes are used due to their excellent durability in the high temperature plasma environment at the thruster exit plane. The three parallel electrodes are aligned with the axis of the arcjet while the probe is swept through the thruster plume during data surveys. The axial location of the perpendicular electrode (P_4) corresponds with the axial location of the probe center.

Each quadruple probe electrode is mounted in round single-bore alumina (Al_2O_3) tubing (0.8 mm o.d. x 0.5 mm i.d.). The electrodes are mounted in the alumina tubes with Omega CC high temperature ceramic-

based cement and binder (Omega Engineering, Inc., Stamford, CT). The alumina tubes which insulate electrodes 3 and 4 are further supported by thin-wall stainless steel tubing (1.3 mm o.d. x 0.9 mm i.d.). The exposed length of the alumina tubes surrounding electrodes 3 and 4 is ~ 5 mm. The two thin-wall stainless steel tubes, while providing rigid support for the very brittle alumina tubing, also help provide a secure fit of the four electrode supports inside the larger stainless steel tube (4.8 mm o.d. x 3.3 mm i.d.) that is the main probe support (Fig. 2.4). Inside this larger tubing is a four-bore alumina tube (3.2 mm o.d. x 0.5 mm i.d.) that electrically insulates the four probe leads inside of the larger stainless steel probe support tube. All of the stainless steel and alumina tubes are held in place using the high temperature ceramic-based adhesive discussed above. A small quantity of this adhesive is also placed at the junction between the perpendicular electrode (P_4) and its single bore alumina tube to electrically insulate the bent portion of the electrode, thereby reducing the error associated with determining its geometric surface area (see Fig. 2.4).

In an effort to minimize the effect of the probe geometry on the plasma flow, a gradual transition between the electrodes and the probe support has been implemented. The radius of the single-bore alumina electrode supports is 0.4 mm, which minimizes perturbations of the plasma flow at the junction between the electrodes and their support, as discussed in section 3.5. Additionally, the ceramic-based high temperature adhesive is used to fill the void, and ease the transition, between the 4.7 mm o.d. stainless steel tube and the probe electrode support tubing as shown in Fig. 2.4. Due to the large axial separation (~ 10 mm) between the main stainless steel support tube and the

quadruple probe sensing electrodes, plasma flow perturbation by the relatively large probe support arm (4.7 mm dia.) is minimal.

The center-to-center separation between electrodes 1 and 2 is 1.4 mm. This spacing, coupled with the electrode lengths (2.5 mm), allows the quadruple probe to handle misalignments between the probe axis and the plasma flow angle as large as 30° without "shadowing" of one electrode by the other during measurements away from the thruster centerline.

2.3.2 Quadruple Probe Electrode Contamination

It has been shown that probe electrode contamination in an MPD thruster plume can have a drastic effect on the triple probe and, hence, quadruple probe response (Tilley, et al., 1990). Tilley, et al. noted that probe contamination occurs through two primary mechanisms for the type of plasma environment investigated in this study: 1) coating of the electrode supports (alumina tubes) with conductive material, and 2) a covering of the electrode surface areas by thin resistive surface layers. Each of these scenarios is discussed below, as it pertains to the arcjet plume region probed in the present study.

Coating the electrode supports with a conductive material:

When a conducting material is deposited on the probe insulating supports, the effective current collection area of the electrode can be increased drastically if the conducting contaminant comes in contact with the electrode. Since this area increase is not accounted for, this type of contamination can lead to large errors in n_e through erroneous measurements in the probe electrode current I_3. The source of this contaminant is generally erosion of the thruster tungsten anode and cathode and subsequent deposition of this

material on the probe supports. However, ion sputtering of the electrode material upstream of the probe supports can also be a cause. Although thruster component erosion is generally not prevalent in the 1-kW arcjet used in this study, a dark "charred" coating was observed on the originally white ceramic adhesive and alumina electrode supports. It is unclear if this coating was deposited on the alumina via ion sputtering of the electrode surface during probe cleaning (see below) or if it was merely a discoloration of the ceramic-based adhesive that was used to mount the electrodes in place. Nonetheless, the ion saturation current I_3 collected by the quadruple probe was carefully observed over the course of the experiments and did not change, even when a well-worn probe was replaced with a new "un-charred" probe. Similarly, applying a fresh coat of ceramic adhesive over the insulator coating consistently had no effect on the measured current I_3, indicating that the layer was not acting as an extension of the probe electrodes current collection area.

Electrode thin resistive surface layers:

Probe electrodes are generally assumed to be fully catalytic surfaces (Chung, et al., 1975). A fully catalytic conducting surface that attracts ions will allow recombination between the attracted ions and electrons released from the conductor surface for every ion present at the electrode surface. Similarly, an electron-attracting conducting surface will, by definition, collect all of the electrons present at the conductor surface. Chung, et al. point out that a probe electrode that has been contaminated by a thin resistive layer does not act in a fully catalytic capacity as discussed above. The causes of these resistive layers are commonly difficult to identify, but are sometimes attributed to the deposition of sputtered material from elsewhere in the plasma.

Contamination can also come from the sorption of neutral species into the electrodes from the gas surrounding the probes (Szuszczewicz and Holmes, 1975). These "monolayers," if nonconductive, can form a partial insulator around the electrode. Additionally, probe contamination may have been caused in this study by a minute layer of vacuum pump oil, as a very fine mist was observed on occasion emanating from the vacuum line after the tank was vented to atmosphere.

With reasoning similar to that of Szuszczewicz and Holmes (1975), Tilley, et al. (1990) point out that electrode contamination by a layer of material dissimilar to the electrode material may introduce a "contact potential difference" to contaminated electrodes in triple probes. They also describe the mechanism by which this type of contamination can affect the response of multiple electrode probes like the triple and quadruple probe. As discussed in chapter 4, the electron temperature is uniquely determined from a measurement of the potential *difference* between the quadruple probe electrodes 1 and 2. Also, the potential of electrode 1 is determined by the amount of electron current required at that electrode to offset the ion current drawn by electrodes 3 and 4 (see Fig. 4.1). The larger the ion current I_3+I_4, the more positive the potential of electrode 1, so that more electrons are attracted to electrode 1 to offset the ion collection at electrodes 3 and 4. When electrode 1 is contaminated by a resistive layer, the electron current to that electrode is impeded, forcing it to become more positive than an uncontaminated electrode so that it can collect the requisite electron current dictated by the quadruple probe circuit. Since $T_e \sim |V_{d2}|$ $(=V_2-V_1)$, increases in the electrode potential V_1 due to electrode contamination cause corresponding increases in the "measured" electron temperature T_e.

A generally accepted way of decontaminating probe electrodes is to use ion bombardment cleaning (Chung, et al., 1975). In this method, a large negative voltage (100-200 V) is applied to the electrode to produce sufficiently energetic ion bombardment so that contaminants are sputtered off of the probe surface. It has been experimentally verified, both in this study and by Tilley, et al. (1990), that this method of probe cleaning has no effect on the currents drawn by ion attracting probes (i.e., the ion saturation current I_3). Tilley, et al. argue that this is because ion-collecting electrodes are continually being decontaminated to a certain extent by ion bombardment cleaning during the data acquisition process.

2.3.3 Quadruple Probe Operation in this Study

During this study, the quadruple probe (see Fig. 2.4) was operated so that the three aligned electrodes (1-3) were aligned with the thrust axis of the arcjet. To obtain radial profiles of the measured quantities, the probe was mechanically swept through the thruster plume in a horizontal plane, so that probe motion was perpendicular to the arcjet axis. This approach to moving the probe quickly through the plume is necessary so that the probe is not destroyed in the high enthalpy plasma environment of the thruster plume. The probe translation mechanism used to mount and sweep the probe is discussed below.

The quadruple probe circuitry (Fig. 4.1) is isolated from the probe electrodes and the thruster to minimize the effect of electronic noise associated with thruster and its power supply on the probe signals. This is accomplished by feeding the probe electrode leads through the vacuum tank

wall before connecting them to the probe circuitry, which can then be located immediately adjacent to the data acquisition system.

During this study, the probe electrodes were cleaned thoroughly before each data acquisition session using ion bombardment cleaning at 200 V below facility ground. Cleaning was performed while the probe electrodes were immersed in the arcjet plasma stream so that the electrodes would glow bright orange during the decontamination process, almost immediately after being placed in the plume. Due to the close proximity of the probe to the arcjet exit plane, care was taken not to leave the probe in the arcjet plume long enough for the tungsten probe electrodes to melt. This was accomplished by easing the probe into the cooler edge of the plasma stream and leaving it there for ~30 seconds at a time. This process was repeated two to three times before the probe was moved to the other side of the plume and the process was repeated, insuring that probe electrodes 1 and 2 (se Fig. 2.4) each received a thorough cleaning. Electrodes 3 and 4 are also cleaned during this process, but it was observed that they did not get quite as hot as the other two electrodes. However, since they collect ion current, contamination of these electrodes is not a large concern, as discussed above.

Quadruple probe sweeps performed prior to this cleaning process at the beginning of a data acquisition session consistently yielded electron temperatures that were approximately twice the post-cleaning values. This is presumably due to burning or sputtering off of vacuum pump oil and other contaminant layers that had built up since the last probe use. In fact, the first "cleaning" of the session was always the most dramatic, as the plume color downstream of the electrodes would change from the normal reddish hue of

the hydrazine plume to orange and yellow while contaminants were removed.

Quadruple probe sweep data were acquired beginning after the cleaning process, and repeated every 1-3 minutes, which was the amount of time required for the probe data from a previous sweep to be viewed and saved to disk. Although data were acquired throughout the thruster warm-up period, all data presented in this study are for steady state thruster operation unless otherwise specified. Data acquired during this warm-up period allowed the effectiveness of the probe cleaning process to be evaluated. After the cleaning process, the indicated electron temperatures would approach a constant value for several minutes before probe re-contamination effects were noted, causing the measured value of V_{d2} to increase drastically. For the low and intermediate values of $P/\dot{m}$ (19.8 and 22.4 MJ/kg) investigated in this study (see Table 2.1) the measured values of T_e would remain constant for ~10 minutes of steady state arcjet operation before contamination effects became evident. After this point, the apparent T_e values increased from ~0.5 eV to quite unrealistic values greater than 2 eV over the span of several minutes. A subsequent re-cleaning of the quadruple probe decreased the measured electron temperatures to their pre-contaminated values. This process was repeated over several different data acquisition sessions, with repeatable results, for the intermediate $P/\dot{m}$ case.

Similar effects were observed for the highest thruster $P/\dot{m}$ (26.0 MJ/kg) investigated, although contamination effects were evident much sooner after probe cleaning than in the first two $P/\dot{m}$ cases, presumably due to the higher operating temperatures of the thruster plume and anode nozzle block. During arcjet operation, the probe tip was located ~5 cm from the arcjet thrust

axis with no thermal radiation shielding between the probe electrodes and the glowing (1320 K) nozzle. The anode temperature for the highest $P/\dot{m}$ case was 100 K and 160 K hotter that the intermediate and lower $P/\dot{m}$ cases, respectively. Since the radiation heat transfer to the probe electrodes scales as T^4, it is suspected that the higher plume temperatures and increased radiative heat transfer increased the operating temperature of the probe electrodes, which in turn affected the rate of contamination of these surfaces. Also, these higher temperatures may have increased the evaporation rates of other materials near the probe (plastic, tape, etc.), increasing the amount of the contaminants in the vacuum chamber.

2.3.4 Probe Mounting and Linear Translation System

The quadruple probe (Fig. 2.4) and the time-of-flight (TOF) probe discussed below (Fig. 2.8) are mounted in the vacuum tank by the probe mount mechanism depicted schematically in Fig. 2.5. The probe mount mechanism and the probe translation mechanism discussed below were fabricated specifically for this study. The thin-wall stainless steel support tubing common to both of these probes is rigidly connected to two retrofitted ceramic thermocouple plugs with a compression-type fitting that also fastens the two thermocouple plugs together. Each of the two plugs houses screw terminal connections for two tungsten wires. The four screw terminal connectors double as a receptacle, allowing connection to the probe lead wires by a single four-prong plug located at the rear of the ceramic thermocouple plugs (Fig. 2.5). This plug is connected to an electrical feedthrough in the tank wall by a 45 cm long four-conductor cable. To protect the probe leads from thermal damage in the thruster plume, the cable was constructed from

individual teflon coated wires. These wires were then wrapped in teflon tape, inserted into a 4.8 mm diameter flexible teflon tube, and surrounded by heat resistant fiberglass braided tubing. The resulting "cable" was flexible enough that it did not prevent the step motor discussed below from freely rotating the probe assembly.

The ceramic thermocouple plugs are mounted from below onto a 1.6 mm (1/16") thick stainless steel plate that has been bent as shown in Fig. 2.5. This plate is mounted via a brass coupling to the shaft of a step motor as shown. The brass coupling is "clamp-fit" onto the motor shaft so that the elevation of the probe can be changed by simply changing the position of the coupling on the motor shaft. The apparatus was designed so that the assembly comprised of the probe, the thermocouple plugs, and the compression fitting could be assembled on the bench and mounted as a complete unit onto the motor shaft coupling. The probe mount was designed so that the probe tip is directly over the axis of the motor shaft. This allows the angle of the probe to be varied by rotating the motor shaft without changing the location of the probe center. The step motor assembly allows rotation of the probe angle in both directions with a step motor controller that was constructed in the Electric Propulsion Laboratory for the purpose of this study. The controller allows the operator to select the angular step size (0.9° or 1.8°) and the rotation direction of the motor shaft.

For all of the results presented in this study, the quadruple and time-of-flight probes are *elevated* such that each probe is centered on the axis of the thruster. More specifically, electrodes 1 and 2 of the quadruple probe are elevated into the same plane as the thruster axis. Similarly, the two electrodes of the time-of-flight probe are positioned so that the thruster axis is

centered between them. This is accomplished by aligning the probe centers with a line etched on the outside edge of the thruster nozzle, near the exit plane. With this method, probe elevation is repeatably located to within 0.5 mm by aligning the probe center with the line etched on the arcjet anode.

The axial separation between the probe tips and the thruster exit plane, which varies from 1-5 mm for this study, is reliably set to within 0.1 mm with a spark gap gauge. The arcjet mount has been shown experimentally to deflect toward the probe ~0.7 mm while the tank is under vacuum. This deflection is accounted for when the probe tip location is set while the vacuum tank is vented to atmosphere. Any error associated with the arcjet exit plane position because of this deflection is systematic and, hence, does not affect the relative spacing of subsequent axial measurement positions.

The motor and probe assembly shown in Fig. 2.5 is mounted to a carriage platform capable of a ± 5 cm linear translation perpendicular to the arcjet axis. A picture of this apparatus is shown in Fig. 2.6 as it appears prior to being mounted in the vacuum tank. The relationship between this equipment and the thruster is depicted in Fig. 2.7, which shows the apparatus as it appears when mounted in the vacuum tank. The silhouettes of the TOF probe and the thruster can be seen through the window in the foreground. This apparatus allows the probe and motor assembly to be swept radially through the plume. The carriage platform rides along to two parallel 6.35 mm diameter shafts, or rails, that are aligned with the direction of the desired probe translation direction. The carriage is connected to one of the shafts by a precision linear ball bearing assembly, allowing smooth and repeatable carriage and probe movement. Connection to the remaining shaft is made via a teflon bushing that surrounds the 6.35 mm diameter rail. The purpose

of the teflon bushing and the redundant second rail is to keep the carriage from rotating about the first shaft.

Carriage and, hence, probe motion is controlled manually by a 12.7 mm stainless steel shaft that passes through a vacuum feedthrough in the tank wall (see Fig. 2.7) and is connected to the side of the carriage. The seal around this drive shaft, which is accomplished with an o-ring, proved to make an excellent vacuum seal as long as the shaft was kept well greased. With this arrangement, the probe could be comfortably swept through the plume at speeds of ~20 cm/s, thus insuring that the probe would not be damaged by exposure to the thruster plasma.

Carriage and probe position are determined by a precision 10 kΩ linear potentiometer that is coupled to the manual carriage drive shaft as shown in Figs. 2.6 and 2.7. The shaft of the potentiometer is coupled to the drive shaft by an aluminum coupling, so that a displacement of the carriage position causes a similar movement of the potentiometer shaft. The probe position is determined to within 0.25 mm relative to the arcjet nozzle by calibrating the voltage output of the 10 kΩ linear potentiometer against the outer diameter of the nozzle. This is accomplished by moving the probe axially toward the arcjet so that the probe electrodes make contact with the arcjet anode block when swept toward the thruster, a process that was utilized on both sides of the arcjet.

Since the probes were quite fragile and because probe construction was very tedious, extensive precautions were taken during the position calibration process to prevent damage as the probe electrodes came in contact with the arcjet. By connecting the probe leads to facility ground and monitoring for continuity between the thruster anode and ground, the exact

point of contact between the probe electrodes and the thruster anode could be determined. By using a digital multimeter with an audio tone to indicate continuity, the probe could be delicately eased up to the arcjet and stopped at the precise moment at which the tone was observed and continuity was established. The voltage output of the potentiometer was recorded at this location and at the corresponding location on the other side of the nozzle exit. Given the potentiometer outputs at these two locations, the outer diameter of the arcjet anode, the probe dimensions, and the excellent linearity of the transducer output, the probe radial position could be calibrated against the potentiometer output. For a regulated voltage of 5.0 V across the 10 kΩ potentiometer, the above procedure resulted in a position calibration typified by

$$x_p = V_{pot} \times \left(20.36 \frac{mm}{V}\right) - 49.97 \text{ mm} \qquad (2.1)$$

where x_p is the positive or negative probe position relative to the thruster axis and V_{pot} is the potentiometer output in volts. The constants in Eq. (2.1) vary based on the size of the probe used, but are consistently near the values given. From the calibration equation given above, it is apparent that the center of the potentiometer range of motion corresponds closely with the thruster centerline location. Using the procedure discussed above, probe locations are known to within 0.25 mm during probe radial surveys.

2.4 Time-of-Flight Electrostatic Probe Geometry

In addition to the quantities n_e and T_e, the quadruple probe also yields the ion speed ratio $[u_i/(2kT_i/m_{H+})^{1/2}]$, so that knowledge of the heavy particle velocity u_i can be used to determine the heavy particle temperature

$T_g = T_i$. To this end, a time-of-flight (TOF) velocimetry technique has been designed and implemented in this study for measuring spatially resolved axial velocities in the arcjet plume. This technique is derived from a previous Current Modulation Velocimetry (CMV) method which was developed by Pobst, et al. (1993). Both the TOF method developed for this study and the CMV technique are discussed in depth in Chapter 4. In this study, a short duration current deficit pulse is superimposed on the arcjet operating current, the effect of which is monitored by an electrostatic time-of-flight probe as it convects axially in the thruster plume.

Figure 2.8 shows a schematic of the electrostatic time-of-flight sensing probe used in this study. It consists of two 0.76 mm diameter tungsten wires which are electrically insulated along most of their length by two 1.57 mm o.d. x 0.79 mm i.d. alumina (Al_2O_3) tubes. The exposed length of each tungsten electrode is 0.25 mm and the axial separation between the two is 5.0 mm. The tungsten electrodes fit tightly inside the alumina tubing inner diameter, allowing each of the electrodes to be held firmly in place without the use of adhesive. The exposed length of each of the electrodes was monitored carefully during the period of time that the TOF probe was utilized and absolutely no movement of either of the electrodes was noted.

In a manner similar to the quadruple probe construction discussed above, the TOF probe sensing tip is supported by a large diameter stainless steel tube (4.75 mm o.d. x 3.35 mm i.d.). This tube is used to mount the TOF probe to the probe translation mechanism discussed above. The alumina tubes that insulate the electrodes extend into this stainless steel tube and are held in place by high temperature cement that fills the void between the stainless steel tube i.d. and the alumina tubes. The exposed lengths of the

alumina tubes are 8 and 13 mm for the downstream and upstream electrode insulators, respectively. The electrode leads are insulated inside of the stainless steel support tube by a double-bore alumina tube (3.18 mm o.d. x 0.79 mm i.d.) that extends the length of the support tube as shown in Fig. 2.8.

Although this probe is physically intrusive, the probe electrodes (0.76 mm dia.) are in the near-free molecular flow regime based on the collision mean free paths presented in section 3.5, and are thus expected to have little effect on the flow. Additionally, any plasma perturbations due to the electrodes are expected to have a similar result at each electrode, thereby having minimal effect on the measurement of the convective time delay between the two TOF electrodes.

2.5 Experimental Facilities

All of the original experimental data presented in this study were acquired in a vacuum tank of the Electric Propulsion Laboratory at the University of Illinois at Urbana-Champaign. Descriptions of the various subsystems of these facilities are presented in the sections that follow.

2.5.1 Vacuum System

To simulate the operating environment of the arcjet, the thruster was operated so that it exhausted into a 1 m diameter x 1.5 m long vacuum tank. The tank was evacuated and kept under vacuum conditions by a 2500 cfm Roots-type blower. Backing for this blower was provided by a second 1300 cfm Roots blower and two 150 cfm mechanical displacement pumps. With no arcjet propellant flow, this pumping system was capable of holding a pressure of 0.025 Torr on the ~1.2 m^2 vacuum tank volume. During steady state arcjet

operation, the tank pressure was nominally ~0.2 Torr for the propellant flowrates utilized in this study.

As shown in Fig. 2.7, mounting of the arcjet in the vacuum tank was accomplished by using a 5-way stainless steel cross, which had an inner diameter of 8". This cross allowed easy access to the thruster and probes without the need to climb into the tank or remove apparatus. The arcjet was mounted opposite the vacuum tank port in the cross, so that the plume flowed unimpeded into the larger tank volume to cool down. The access ports on either side of the thruster were outfitted with 6" dia. x 0.5" thick quartz windows so that the thruster and probes could be viewed during the experiments. The quartz window mount shown in the foreground in Fig. 2.7 has been modified for the probe carriage manual drive shaft and position transducer as discussed above in section 2.3.4. The vacuum system discussed above is connected to the vacuum tank volume through the remaining port, on the bottom of the 5-way cross. Evacuating the arcjet exhaust gases from below the thruster plume had no effect on the plume, which could be observed as far as 30 cm downstream of the arcjet exit plane.

2.5.2 Thruster Propellant Supply

The thruster propellant used in this study was a gaseous mixture of nitrogen (N_2) and hydrogen (H_2) to simulate fully decomposed hydrazine (N_2H_4) propellant. To approximate N_2H_4, a molecular mixture of 2/3 hydrogen and 1/3 nitrogen was used. These gases were supplied from industrial gas cylinders, each with a 99.95% purity. The nitrogen supply was stored near the gas metering system discussed below. However, for safety reasons the hydrogen was stored in a remote tank farm and piped into the

laboratory, which is equipped with hydrogen alarms connected to the H_2 supply solenoid. Each component of the propellant was individually metered by mass flow controllers and mixed in the 8 meter propellant line feeding the arcjet from the flow controllers.

The hydrogen gas was metered by a Unit Instruments, Inc. model UFC-1510A mass flow controller with a maximum capacity of 10 SLM, or approximately 15 mg/s of H_2. The nitrogen was metered by a model UFC-1500A controller that had a maximum capacity of 5 SLM, which corresponds to approximately 80 mg/s of N_2. These devices were calibrated at the factory, but independent calibrations were frequently conducted in the Electric Propulsion Laboratory to insure that the behavior of the controllers did not shift during the experiments. This was accomplished using an ideal gas law approach, along with measurements of the time required for the gas to effect a certain pressure rise in a small tank. The gas temperatures were monitored during this process by a type K thermocouple that was inserted into the middle of the calibration tank. Since the temperature varied by no more than a few degrees K during the fill process, the average of the initial and final temperatures was used to calculate the gas mass flow rate $\dot{m}$. The calibration equation used to calculate $\dot{m}$ is given by

$$\frac{dm}{dt} = \dot{m} = \frac{V_t \, \Delta P}{R \, (T_{ave}) \, \Delta t} \tag{2.2}$$

where V_t is the volume of the calibration tank (17080 cm^3), R is the gas constant for the gas being calibrated, T_{ave} is the average gas temperature during the fill process, and Δt is the time required to change the pressure in

the tank ΔP. Using this method, the mass flow rates of the individual gases supplied to the thruster are known to within ± 2%.

The calibrations for each of the mass flow controllers were very linear over their full range as shown in Figs. 2.9 and 2.10. For a desired propellant $\dot{m}$, the flow rates of the individual components are specified as a percentage of the total capacity of the flow controllers, as shown in the calibration plots. After the desired flow rates are set, the total $\dot{m}$ supplied to the arcjet is kept quite constant during the course of the experiments by feedback loops built into the flow controller units. The thruster mass flow rates used in this study, along with the corresponding amounts of H_2 and N_2 are given below in Table 2.2.

Total $\dot{m}$ (mg/s)	$\dot{m}$ of H_2 (mg/s)	FC #1 (%)	$\dot{m}$ of N_2 (mg/s)	FC #2 (%)
45	5.6	37.4	39.4	50.9
50	6.3	41.6	43.7	56.4
60	7.5	49.8	52.5	67.3

Table 2.2 Summary of the flow controller (FC) settings for the hydrazine propellant mass flow rates used in this study.

2.5.3 Data Acquisition Equipment

Probe signals, including the probe radial position signal, were recorded during the quadruple, triple, and single electrostatic probe experiments with a Soltec, Inc. ADA-FE-08R four-channel digitizing oscilloscope. This device is capable of up to 10 MHz sampling with storage capacity for 64 K samples on each of four channels. Probe sweep data were sampled at several times the

PPU ripple frequency (16 kHz), and the effects of this PPU ripple on the probe response were smoothed unless otherwise noted (see section 5.3.1). Signal traces were transferred to a personal computer for processing via an IEEE-488 bus with a connection between the scope and the computer.

During the time-of-flight experiment, the TOF probe electrode signals were recorded with a Hewlett Packard HP 54510A high speed digital oscilloscope. This scope was used because the 10 MHz speed of the Soltec scope describe above was not fast enough to capture the TOF signal time delay with reasonable resolution. The HP 54510A scope recorded the TOF signal data at a rate of 250 MHz. Every other point of these data traces were saved to disk, for an effective sampling rate of 125 MHz. As discussed in section 4.3.6, this temporal resolution (8.0×10^{-9} s) was more than adequate for the ~1 μs time delay measured with the TOF technique. The arcjet voltage V_{arc} and current I_{arc} were recorded during the current deficit pulse with the Soltec, Inc. equipment discussed above. The HP 54510A and the Soltec scopes were triggered simultaneously during this experiment by the gate pulse supplied from the HP 214A pulse generator shown in Fig. 4.14.

To provide signal level for the arc voltage V_{arc} that was suitable for the data acquisition system, a simple voltage divider was placed in parallel with the arcjet. The divider is comprised of a series of two 2 Watt carbon resistors (1.04 kΩ and 10.15 kΩ) so that the voltage divider draws less than 0.1% of the total PPU current supplied for the arcjet. The arc voltage measurement is made across the 1.04 kΩ resistor so that the voltage divider reduction ratio is 10.75:1. During arcjet start-up, a 4 kV starting pulse is supplied to the arcjet by the PPU, requiring that a mechanical isolation switch be placed between the

arcjet and the voltage divider to protect the laboratory data acquisition equipment from this high voltage starting pulse.

The current supplied to the arcjet by the PPU was measured by an active Hall-effect current sensor. A LEM USA, Inc. model LTA 100P 1:1000 current transformer was used, which produced an output of 0.001 amps for each amp of arc current passing through the transducer coil. The output current was measured by recording the voltage drop due to the current across a 34.6 Ω resistor. To increase the transducer output signal to a manageable level (1.5-2.0 V), the arcjet current lead was looped through the current transformer 5 times. The resulting conversion for the arc current was $I_{arc} = 5.78 \times V_{out}$, where V_{out} is the voltage drop across the 34.6 Ω resistor.

Anode temperature measurements (T_{anode}), reported in section 5.1, were measured with an Ircon, Inc. Ultimax infrared thermometer. This device was focused on the anode insert (see Fig. 2.1), through a quartz window (Fig. 2.7), from a distance of ~3 feet. The focused spot size on the anode was ~ 1/8" diameter at this distance. An assumed value for the emissivity of the thoriated tungsten anode of $\varepsilon = 0.38$ was used. However, the measured values of T_{anode} were found to be insensitive to this parameter.

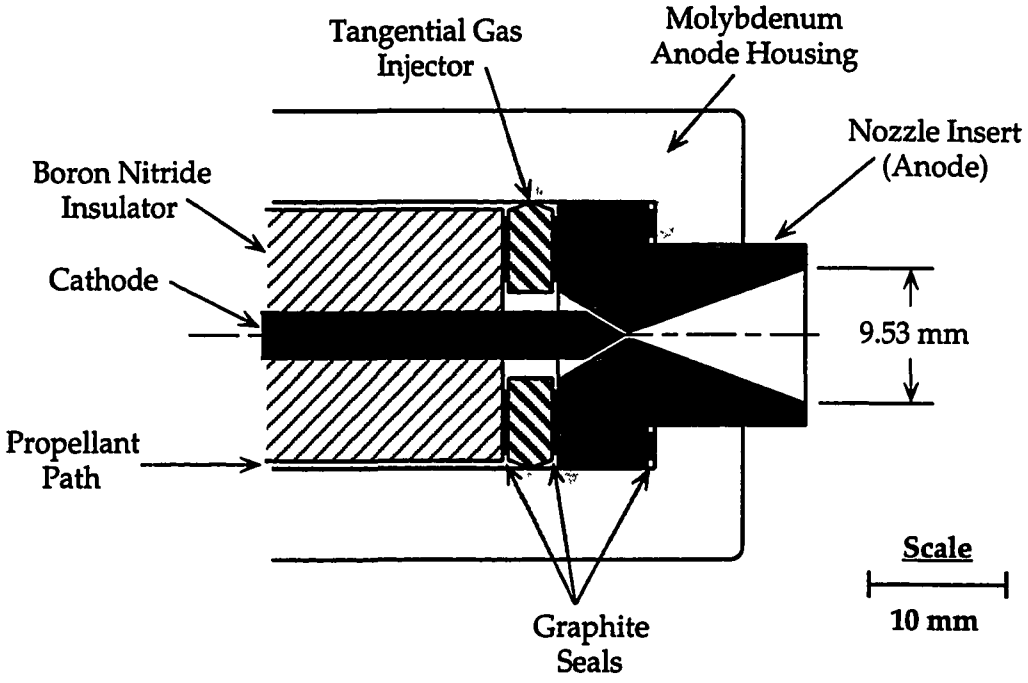

Fig. 2.1 Cross-sectional schematic view of the NASA Lewis Research Center 1-kW arcjet used in this study.

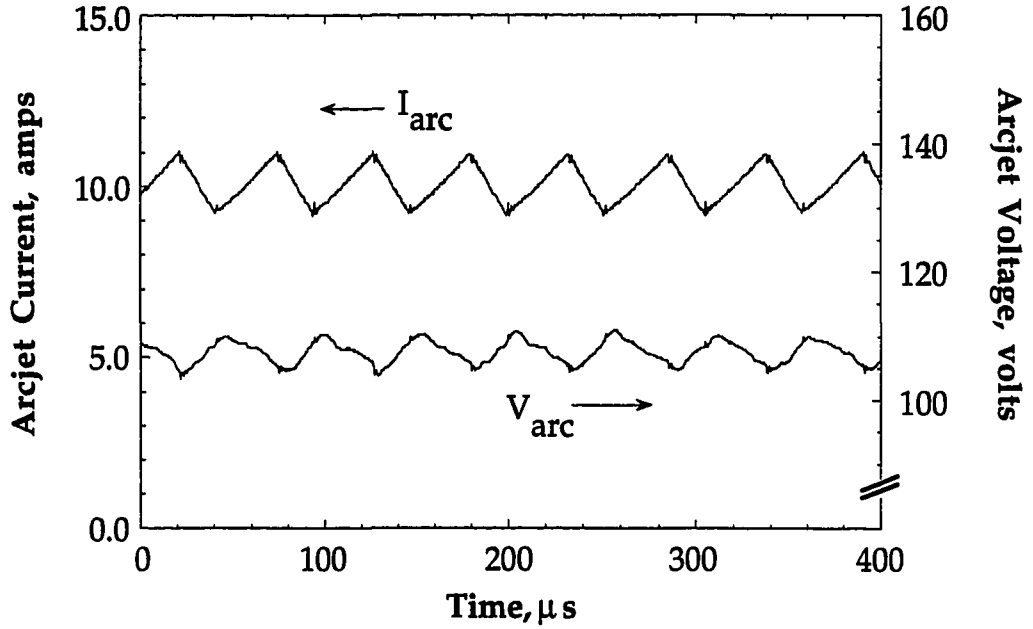

Fig. 2.2 Arcjet current and voltage traces showing the effect of the power processing unit (PPU) ripple.

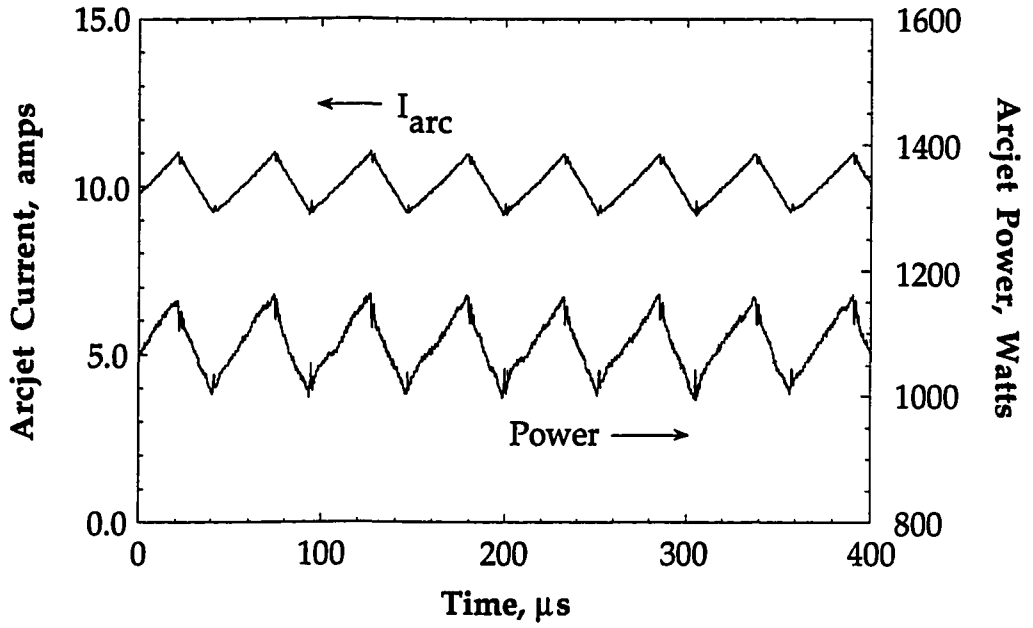

Fig. 2.3 Arcjet current and power (= I_{arc} x V_{arc}) traces showing that the thruster power input varies with the arcjet current.

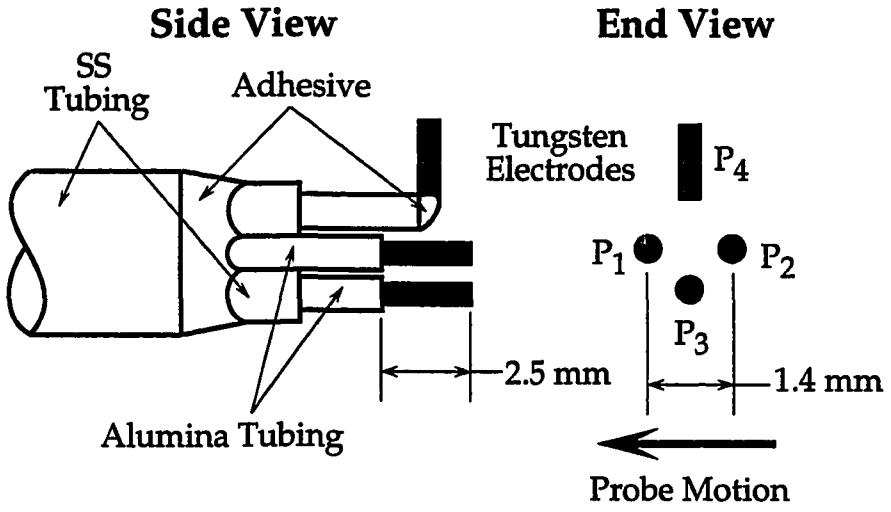

Fig. 2.4 Schematic view of the quadruple probe used in this study. The probe is swept through the plume with the three aligned electrodes parallel to the thruster axis.

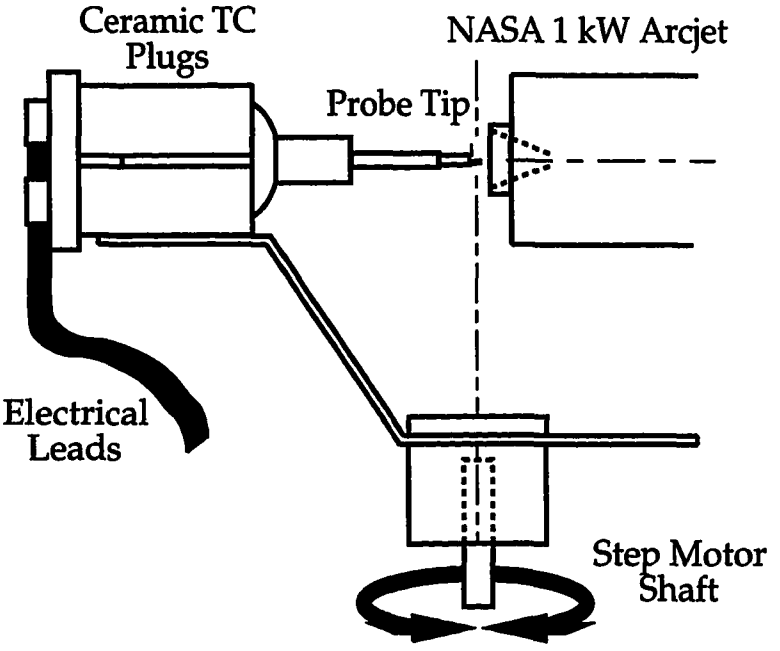

Fig. 2.5 Schematic view of the probe mount apparatus used to mount the quadruple and time-of-flight probes used in this study.

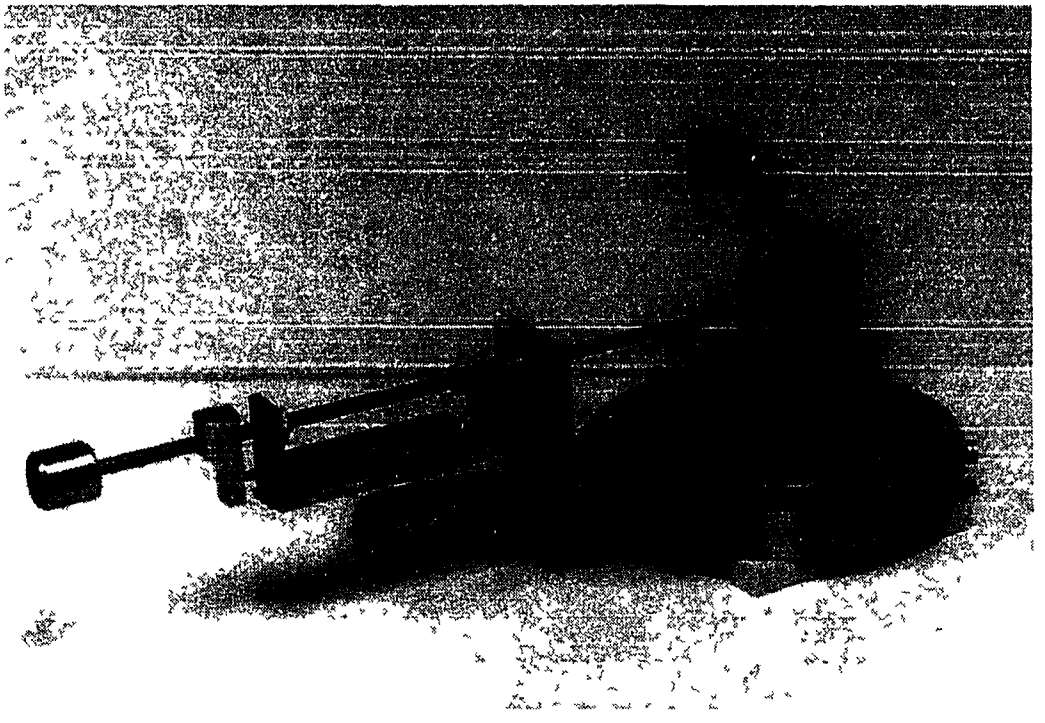

Fig. 2.6 Photograph of the linear translation carriage used to sweep the probes through the arcjet plume. This apparatus mounts in the vacuum tank as shown in Fig. 2.7.

Fig. 2.7 Photograph of the linear translation carriage mounted in the vacuum tank. Silhouettes of the TOF probe and arcjet are visible through the quartz window.

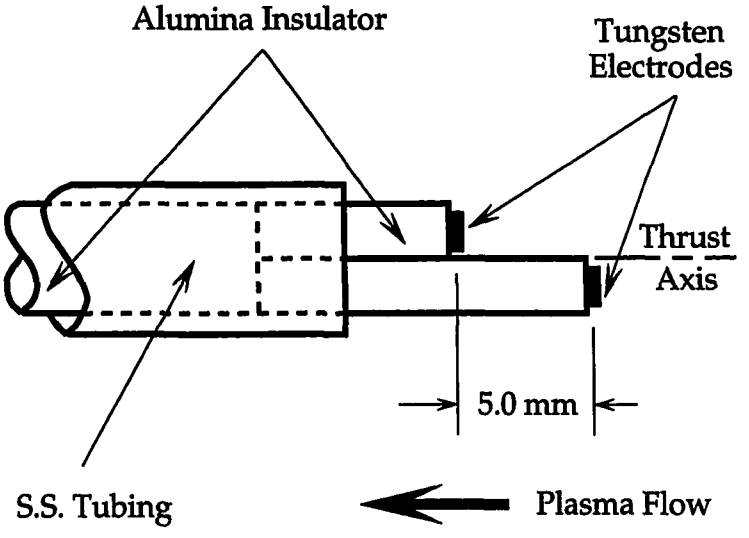

Fig. 2.8 Side view schematic of the time-of-flight electrostatic probe developed for this study

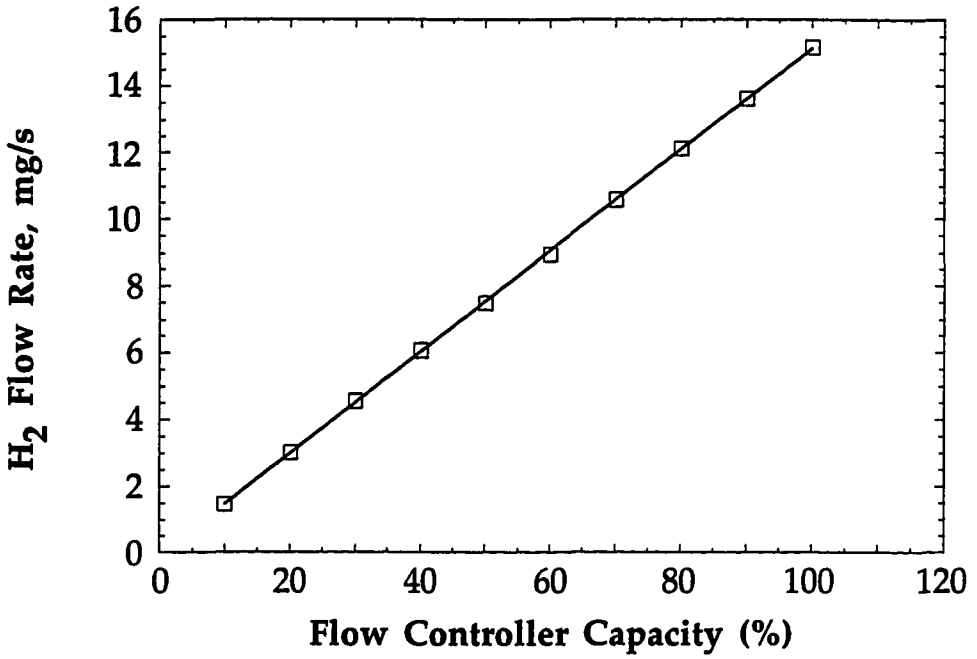

Fig. 2.9 Hydrogen (H_2) gas calibration plot for the 10 SLM mass flow controller.

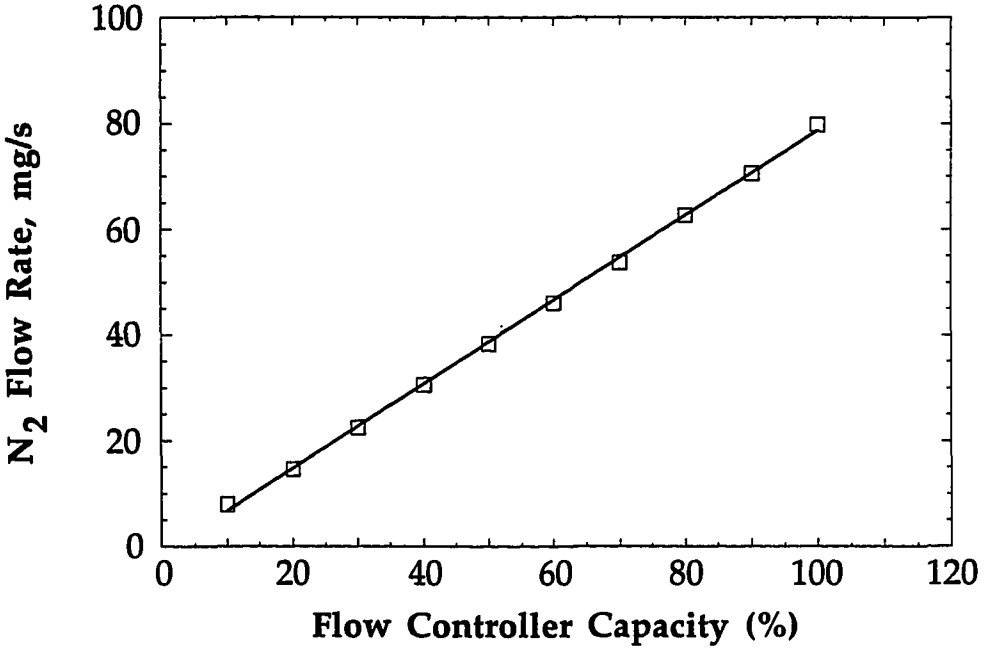

Fig. 2.10 Nitrogen (N_2) gas calibration plot for the 5 SLM mass flow controller.

3. General Electrostatic Probe Theory

3.1 Single Langmuir Probe Theory

Despite the attractiveness of modern optical techniques for making measurements of plasma parameters, one of the simplest and most inexpensive ways to make these measurements remains the electrostatic probe. This method of plasma probing, first introduced by Irving Langmuir (1926), is appealing because electrostatic probes directly sense plasma particle fluxes by collecting charged particles (ions, electrons) while immersed in the probed plasma. By the same reasoning, however, the electrostatic probe technique is physically intrusive. Fully understanding the extent to which the probe interacts and perturbs the plasma can be a non-trivial matter that requires thorough consideration. Also, because this is an intrusive technique, the application can be limited to use in plasmas in which the probe can physically survive the high temperature plasma environment.

The simplest electrostatic probe consists of an electrode which is connected to a power supply and immersed in a quiescent plasma, as shown in Fig. 3.1. Probe electrode geometry is generally a planar, cylindrical, or spherical, although any geometry can be utilized. The power supply is grounded to an electrode that is in intimate contact with the plasma (e.g., one of the plasma generating electrodes). The plasma between the probe electrode and the power supply ground completes the probe electrical circuit. The probe collects the charged ions and/or electrons that comprise the plasma, the relative amounts of which are determined by the probe bias voltage relative to the potential of the plasma. Collection of charged particles at the probe electrode surface results in an electrical current in the probe circuit, which can

be measured by passing the current through a small shunt resistor or through some other means. By measuring the amount of current collected by the electrostatic probe as a function of the probe bias voltage, information about the plasma potential V_p, electron temperature T_e, and electron density n_e can be determined. The resulting plot of probe current versus probe voltage is commonly called a probe voltage-current (V-I) characteristic. A discussion of the shape of the V-I curve and the method by which V_p, T_e, and n_e are extracted from the V-I characteristic are discussed below in sections 3.1.2 and 3.1.4.

3.1.1 Perturbing Effect of the Probe on the Plasma

A probe that is placed in a plasma to measure a plasma parameter almost always perturbs or alters the quantity being measured. This is because a probe electrode acts as a boundary region of the plasma where normal plasma behaviors like plasma quasineutrality (the assumption that $n_e = n_i$) do not hold. Additionally, large electric fields can be sustained by the plasma near a plasma boundary. This region of plasma perturbation is generally referred to as a plasma sheath or a Debye sheath.

As an illustration of how an electrode sheath perturbs the plasma, consider an electrode that has been insulated from ground so that it draws zero net current, as shown in Fig. 3.2. Despite the fact that the electrode draws no current, charged particles will still initially hit its surface due to the random thermal motion of the particles. Because the electrons are lighter and have a much greater mobility than the ions, the flux of electrons hitting the electrode surface will be much greater than that of the ions. However, the zero current requirement of the floating electrode forces the flux of ions and

electrons at the electrode surface to be equal. To satisfy this requirement, the electrode acquires a negative potential relative to the plasma potential so that some of the electrons are repelled from the electrode surface. The potential difference between the plasma and electrode potentials that satisfies the requirement of zero current collection is the sheath potential V_s. For a floating electrode, the sheath potential drop V_s can be solved analytically by summing the ion and electron current into the probe and solving for the potential that satisfies the zero net current requirement (Schott, 1968). This yields an electrode sheath potential of

$$V_s = -\frac{kT_e}{2e} \ln\left(\frac{m_i}{m_e}\frac{T_e}{T_i}\right) \tag{3.1}$$

The sheath potential drop is a downhill potential that attracts ions and an uphill potential that repels all but the most energetic electrons. The variation in potential between the undisturbed plasma and the plasma boundary represents a large electric field ($E = - dV_x/dx$). The spatial extent of this electric field determines the size of the electrode sheath. The Debye length λ_D, which is defined as

$$\lambda_D = \left(\frac{\varepsilon_o\, kT_e}{n_e\, e^2}\right)^{1/2} \tag{3.2}$$

represents the spatial extent over which a quasineutral plasma can violate charge neutrality. When the condition of charge neutrality is violated (e.g., near a plasma boundary), the plasma adjusts itself over the region of a few Debye lengths to shield the undisturbed plasma from the sheath electric field.

(Hutchinson, 1987). Hence, it is generally acknowledged that the size of the electrode sheath is on the order of a few Debye lengths.

3.1.2 Single Probe Voltage-Current (V-I) Characteristic

A schematic of the general form of a typical probe V-I characteristic is shown in Fig. 3.3. The unique shape of the V-I curve is a reflection of its ability to attract and repel ions and electrons at varying probe bias voltages. In Fig. 3.3, the potential of the undisturbed plasma surrounding the probe is denoted by V_p, which is also called the plasma potential. When the probe electrode is biased at the same voltage as the plasma potential, the probe neither attracts or repels charged particles. Since the probe voltage and plasma potential are the same, there is no sheath formation and as such, no corresponding electric field surrounding the electrode to accelerate charged particles as shown in Fig. 3.3. Despite the fact that particles are not attracted to the probe, electrons and ions still collide with the probe due to random thermal diffusion. Since the electrons are much more mobile than the much larger and heavier ions, the net flux of electron charge to the probe surface will greatly exceed that due to ions and the probe will draw a net electron current when biased at the plasma potential V_p.

As the probe bias voltage is decreased from the plasma potential, the electrons begin to be repelled, and ions are attracted to the probe, which is now more negative than the surrounding undisturbed plasma. This trend continues while the probe bias is decreased to the probe floating potential V_f, where the net current drawn by the probe is zero. Here, equal numbers of electrons and ions are collected at the probe surface. The region of the V-I characteristic between V_p and V_f is called the transition region or the electron

retarding region. A probe biased at the floating potential V_f is equivalent to an electrode immersed in a plasma that is perfectly insulated from ground, which is forced to collect zero net current by its lack of an external path to ground. At the point V_f in the V-I characteristic, all but the most energetic electrons are repelled by the probe negative potential hill.

As the probe potential is made more negative than V_f, all of the electrons are repelled and the probe collects only ion current. This part of the characteristic is known as the ion saturation current region. One would expect the ion current in the ion saturation region to be constant with potential since all of the electrons are being repelled and all of the ions that can possibly be collected are collected. The slight increase in ion saturation current with increasing negative potential is due to the fact that the sheath surrounding the probe is increasing, which in turn increases the effective current collection area of the probe. As discussed below, this effect is minimal in the case of very thin sheaths.

In a manner similar to that of the ion saturation current region, the electron current is saturated when the probe is biased at a potential greater than the plasma potential V_p and all of the ions are repelled. The slope of the V-I curve in the electron saturation region has been shown to be dependent on the probe geometry (Fig. 3.3), due to the effect of increasing sheath thickness with potential on the various geometrical surface areas (Kushner, 1994).

For a single electrostatic probe immersed in a plasma environment, generation of the V-I characteristic can immediately yield the plasma potential V_p. Additionally, the characteristic can also yield measurements of

the electron temperature T_e and the electron density n_e, as discussed below in section 3.1.4.

3.1.3 Regimes of Probe Electrode Operation

Electrostatic probe performance can be influenced by several different lengths and length scale ratios. Among these lengths are the relevant collision mean-free-paths λ_{mfp}, the Debye length λ_D, and the probe electrode dimension or radius r_p. For this discussion, λ_{mfp} refers in general to particle collision mean-free-paths, where the relevant particle collisions depend on whether the probe is collecting ions or electrons. For ion collection, ion-ion and ion-neutral collisions are important while electron-electron and electron-neutral collisions are most important for a probe collecting electron current (Carney and Sankovic, 1989). The regimes of cylindrical electrode performance are summarized in Fig. 3.4 for the full ranges of the ratios λ_{mfp}/λ_D and r_p/λ_D (Chung, et al., 1975). The ratio λ_{mfp}/λ_D, which is a measure of the relative size of particle collision mean-free-paths and the sheath thickness, determines the extent to which collisions in the sheath affect charged particle collection by the probe. For very small λ_{mfp}/λ_D, a particle attracted to the probe is expected to undergo several collisions in the sheath before it reaches the probe. If these sheath collisions are ionization or recombination collisions, the number of particles collected at the probe will not be a good representation of the number of the those particles in the undisturbed plasma. Similarly, large λ_{mfp}/λ_D corresponds to the collisionless sheath regime (Fig. 3.4) where all of the particles present at the sheath edge are accelerated to the probe and collected without undergoing collisional processes.

Within the collisionless sheath regime ($\lambda_{mfp}/\lambda_D >> 1$), probe performance is further dictated by the ratio of the probe radius to the sheath thickness r_p/λ_D. For $r_p/\lambda_D < 1$, the sheath thickness is a significant fraction of the probe radius so that the effect of the sheath geometry on charged particle collection cannot be ignored. In the limit $r_p/\lambda_D \rightarrow 0$, this corresponds to the Orbital Motion Limit of electrostatic probe operation (Chung, et al., 1975). In this limit, individual particle trajectories, or orbits, within the thick sheath must be considered. A much simpler analysis can be employed in the Conventional Langmuir Probe regime, which occurs when the sheath surrounding the electrode is thin ($r_p/\lambda_D > 1$) and collisionless ($\lambda_{mfp}/\lambda_D > 1$). It is this regime of electrostatic probe operation that will be discussed here, since this is the regime of probe electrode operation expected near the exit of the arcjet thruster as discussed below in section 3.5.

In addition to the length scale ratios discussed above, the parameter λ_{mfp}/r_p is also important to Langmuir probe operation. For $\lambda_{mfp}/r_p < 1$, the probe electrode is in a regime where particle collisional effects are important. The effect of collisions on probe response is to reduce the current collected by the probe since the charged particles must diffuse to the sheath edge rather than arriving by free flight (Hutchinson, 1987). In the case of $\lambda_{mfp}/r_p > 1$, the probe electrode is operating in the free molecular regime and the effect of particle collisions with the probe can be ignored.

3.1.4 Extracting T_e and n_e from the V-I Characteristic

For the plasma conditions at the thruster exit measured in this study, the probe electrodes are in the Classical Langmuir Probe (Fig. 3.4) regime, as discussed in section 3.5. More specifically, the plasma sheath surrounding the

probe electrodes is thin and collisionless. Additionally, collision mean-free-paths in the vicinity of the probe are sufficiently large that the probe electrodes operate in the free molecular regime and collisional effects can be neglected. It is this regime of operation that will be discussed in the context of extracting T_e and n_e information from a single Langmuir probe V-I characteristic.

For a plasma-probe system in which the electrode sheath is thin and collisionless, the electrode is operating in the free molecular regime ($\lambda_{mfp} >> r_p$), and the electrons have a maxwellian energy distribution, the electron current I_e collected by the probe in the electron transition region ($V_f<V<V_p$) is given by (Swift and Schwar, 1969)

$$I_e = n_e e A \left(\frac{kT_e}{2\pi m_e}\right)^{1/2} \exp\left[-\frac{e}{kT_e}(V - V_p)\right] \tag{3.3}$$

where V is the single probe bias voltage, V_p is plasma potential of the unperturbed plasma, and A is the collection area of the probe electrode, including the sheath area. Due to the thin sheath assumption, the increase in collection due to the presence of the sheath is small and to a good approximation the collection area is merely the geometric surface area of the probe electrode. Equation (3.3) can be applied to Langmuir probes of planar, cylindrical, and spherical electrodes. The electron temperature can be determined from Eq. (3.3) by taking the natural logarithm and taking the derivative of both sides with respect to the probe bias voltage V. This yields the following expression for T_e:

$$\frac{d(\ln I_e)}{dV} = -\frac{e}{kT_e} \tag{3.4}$$

By Eq. (3.4), the electron temperature can be determined from the inverse slope of a ln(I) versus probe voltage plot of the Langmuir probe current in the transition region of the V-I characteristic.

Equation (3.3) can be evaluated at the plasma potential and rearranged to solve for the electron density

$$n_e = \frac{I_e(V_p)}{e\,A}\left(\frac{2\,\pi\,m_e}{kT_e}\right)^{1/2} \tag{3.5}$$

where $I_e(V_p)$ is the probe electron current evaluated at the plasma potential, which is determined by the "knee" in the V-I characteristic (Fig. 3.3). The electron density is determined using the electron temperature found from Eq. (3.4) in conjunction with Eq. (3.5).

3.2 Bohm Sheath Criterion

The electron saturation current drawn by a probe can be quite accurately represented by the thermal diffusion of electrons to the probe surface via the electron thermal velocity. However, the ion saturation current has been shown experimentally to be much larger than that due to ion random thermal motion. This phenomenon can be explained by the Bohm Sheath Criterion (Bohm, et al., 1949). Figure 3.5 shows the sheath schematic used to demonstrate the physics governing the Bohm analysis. The Bohm sheath consists of two distinct regions: 1) The sheath region characterized by $n_i > n_e$ and a large sheath electric field, and 2) the quasineutral "presheath" region with $n_i \approx n_e$, which serves as bridging region between the sheath and the undisturbed plasma ($n_i = n_e = n_o$) to facilitate matching boundary conditions between the two regions. From Poisson's

equation, noting that $n_i > n_e$ in the sheath, Bohm calculated the ion velocity at the sheath/presheath boundary v_{Bohm} as

$$v_{Bohm} = \left(\frac{kT_e}{m_i}\right)^{1/2} \tag{3.6}$$

which is commonly called the Bohm velocity. The fact that the ions have been accelerated from the ion thermal velocity in the undisturbed plasma to the Bohm velocity at the sheath edge is an indication that there is a potential gradient or electric field present in the presheath. From energy conservation across the presheath, the potential drop between the undisturbed plasma and the sheath edge is

$$\Phi_{Bohm} = \left(\frac{kT_e}{m_i}\right)^{1/2} \tag{3.7}$$

The significance of the potential drop Φ_{Bohm} across the presheath is that ions collected at the sheath edge have been accelerated through the presheath electric field, rather than having arrived at the sheath edge at the ion thermal diffusion velocity.

At any point x in the sheath, the electron density $n_e(x)$ is reduced by the Boltzmann factor due to the repulsive sheath electric field such that

$$n_e(x) = n_o \exp\left(\frac{e\,V(x)}{kT_e}\right) \tag{3.8}$$

where $V(x)$ is the negative potential relative to the plasma potential V_p and n_o is the electron density in the undisturbed plasma. At the sheath edge, $V(x) = \Phi_{Bohm}$ and $n_i \approx n_e$ such that Eq. (3.8) reduces to the following expression for the ion density n_{Bohm} at the sheath/presheath boundary:

$$n_{Bohm} = n_o \exp\left(\frac{e\,\Phi_{Bohm}}{kT_e}\right) = n_o \exp\left(-\frac{1}{2}\right) \tag{3.9}$$

By forming the expression $I=eA(v_{Bohm})(n_{Bohm})$, Eqs. (3.6) and (3.9) yield the following expression for the ion saturation current density j_i passing through the sheath edge and being collected by the probe electrode

$$j_i = \frac{I}{A} = e\,n_e\left(\frac{kT_e}{m_i}\right)^{1/2}\exp\left(-\frac{1}{2}\right) \tag{3.10}$$

where n_e ($=n_i$) is the electron density in the undisturbed plasma. Note that, since the Bohm ion velocity is related to the electron temperature through Poisson's equation, the ion saturation current density j_i is a function of T_e rather than T_i.

Clearly, the very presence of an electrostatic probe in a plasma severely alters the values of plasma parameters such as n_e in the vicinity of the probe. It is only through understanding the extent of these effects through approaches like the Bohm analysis that probe measurements can be related to the unperturbed plasma conditions. The Bohm criterion, specifically Eq. (3.10), will be utilized in the quadruple electrostatic probe theory for this purpose in section 4.1.

3.3 Cylindrical Probes in a Flowing Plasma

Although the technique of using electrostatic probes for measuring plasma parameters was originally developed for use in quiescent plasmas, cylindrical probes have seen much use in high-speed flowing plasmas. For many applications, Langmuir probe theory can be used without modification with cylindrical probes aligned with the plasma flow, as long as all relevant

collision mean-free-paths are large compared with the probe radius (Chung et al., 1975). For a cylindrical Langmuir probe aligned with the flow vector, current collection is due to particle diffusion radial to the probe and subsequent capture by the sheath surrounding the probe, as shown in Fig. 3.6. Aside from the exceptions discussed below, superimposing a drift velocity parallel to the cylinder has little effect on this radial particle motion current collection.

3.3.1 Cylindrical Probe "End Effect" Parameter

For certain plasma conditions, some experimental efforts have shown that a cylindrical probe in flowing plasma can be very sensitive to slight misalignments between the probe and the plasma flow (Chung, et al., 1975). Chung et al. argue that this phenomenon occurs when the sheath surrounding the probe becomes significantly large. They state that the probe can collect particles through the end of the sheath as well through the lateral sheath surface via the Bohm phenomenon. If the sheath is thick enough and the directed velocity u_i is large compared with the Bohm velocity, then a large number of ions will can reach the probe through the end of the sheath. It is this effect that causes a large peak in the measured ion current for probes at small angles of attack. The so-called end effect parameter τ_L, which is a measure of the sheath thickness and the relative magnitudes of the directed ion velocity u_i and the Bohm velocity v_b, has been suggested as a means of characterizing this effect (Chung et al. 1975). The end effect parameter is given by

$$\tau_L = \frac{L}{\lambda_D} \frac{(kT_e/m_i)^{1/2}}{u_i} \tag{3.11}$$

where L is the length of the probe and λ_D is the Debye length, which is a measure of the sheath thickness as discussed above. The term L/λ_D, when expressed as $(L/r_p)(r_p/\lambda_D)$, demonstrates dependencies on both the sheath thickness and the aspect ratio of the probe. Chung, et al. (1975) state that in order to eliminate this effect in high speed plasma flows, the end effect parameter [Eq. (3.11)] should be large, $\tau_L>50$. The magnitude of this parameter for the conditions at the arcjet thruster exit is discussed below, in section 3.5.

3.3.2 Current Collection at the Cylindrical Probe Tip

When used in a flowing plasma, cylindrical probe theory does not provide for an accounting of the magnitude of the current collected at the probe tip due to charged particles convected to the tip by the plasma flow velocity. It is important to assess the extent of the error introduced to Langmuir probe current measurements by the probe tip current. Although the parameter τ_L provides an accounting for the effect of ions collected through the sheath end at small angles of incidence, it is not immediately clear that it accounts for the magnitude of the probe tip current. A simple expression has been developed to examine the effect of probe tip current for the present study. For a single ion plasma, the ion current convected to the cylinder tip is given by

$$I_t = e\, n_i\, u_i\, \pi(r_p)^2 \tag{3.12}$$

where n_i is the ion density, which is $n_i = n_{H^+} + n_{N^+}$ for this study as discussed in Chapter 4. The Bohm current collected along the cylinder lateral surface for a two ion species (H^+ and N^+) plasma is given by

$$I_b = e\,2\pi r_p\,L\left[(v_{b,H^+})n_{H^+} + (v_{b,N^+})n_{N^+}\right] \tag{3.13}$$

where L is the electrode length and v_{b,H^+} and v_{b,N^+} are the Bohm velocities for H^+ and N^+, respectively. For a quasineutral ($n_i=n_e$) plasma with an ion composition defined by $f = n_{H^+}/n_e$ ($1-f = n_{N^+}/n_e$), the ratio of ion tip current to the Bohm current I_t/I_b is

$$\frac{I_t}{I_b} = \frac{u_i\, r_p}{2\,L\left[f\,(v_{b,H^+}) + (1-f)\,(v_{b,N^+})\right]} \tag{3.14}$$

From Eq. (3.14), the error introduced by ion current collected at the probe tip can be clearly seen. For large values of I_t/I_b, the percentage of total probe ion current originating from the probe tip is large, introducing large errors into the probe measurements. A similar expression for electron current is less prohibitive because the term I_t will remain the same (by quasineutrality) while the denominator in Eq. (3.14) will be much larger because electron saturation current is much larger than ion saturation current. Equation (3.14) is evaluated for the quadruple probe electrodes in section 3.5.

3.4 Multiple Electrode Probing Systems

Although the single Langmuir probe technique discussed above can be a very useful technique for measuring T_e, n_e and V_p, there are cases in which the method is undesirable. In situations where the measured quantities are fluctuating much faster than a reasonable probe voltage sweep rate, for example, the single Langmuir probe loses its utility. Also, single probe use is difficult in plasmas where the thermal load on the probe is too great to allow the probe to be stationary during the time required for the probe voltage sweep. Finally, it can be a time consuming process to extract T_e and n_e data

from a single Langmuir probe characteristic. Often times, it is desirable to have an instant and simultaneous indication of T_e and n_e during the data acquisition process. It is also desirable in some instances to obtain spatial profiles of the measured quantities as an electrostatic probe is physically swept through a plasma at a high rate of speed to prevent probe destruction. By using multiple electrode probe systems like the triple probe (Chen and Sekiguchi, 1965 and Tilley, 1990) and the quadruple probe (Burton, et al., 1993), these shortcomings of the classical single Langmuir probe can be avoided.

3.4.1 Triple Probe

The triple probe utilizes three individual electrodes, each similar to the single electrode used in the classical Langmuir probe method described above. Derivation of the triple probe response is very similar to that of the quadruple probe response, which is thoroughly discussed in section 4.1. As such, this technique will be only summarized here for the purpose of demonstrating the benefits of the multiple electrode probing systems. The reader is referred to Chapter 4 or the reference by Chen and Sekiguchi (1965) for a more in-depth discussion of the derivation.

The electrical configuration of the triple probe is shown schematically in Fig. 3.7. The probe consists of three cylindrical electrodes which are aligned with the plasma flow and connected to the electrical circuit as shown in the figure. The current I_2 forced to be zero by the floating nature of electrode 2. Electrode 3 is biased below electrode 1 by the prescribed voltage V_{d3}. The potential difference V_{d2} between electrodes 1 and 2, and the probe current I_3 are the measured quantities.

Analytic expressions can be written for the probe currents I_1, I_2, and I_3 in terms of the electron temperature T_e and electron density n_e (Chen and Sekiguchi, 1965). These expressions can be manipulated, based on the circuit constraints shown in Fig. 3.7, to solve for T_e and n_e directly, without the need to reduce a V-I characteristic as in the single Langmuir probe technique. Since the probe bias voltage is a prescribed potential, the triple probe can yield spatially resolved, nearly real-time measurements of T_e and n_e as the probe is translated through a plasma.

Manipulation of the analytic electrode current expressions for a single-component plasma yields the expression (Chen and Sekiguchi, 1965)

$$\frac{1}{2} = \frac{1 - \exp(-\phi V_{d2})}{1 - \exp(-\phi V_{d3})} \tag{3.15}$$

where $\phi = e/kT_e$. Since the quantity V_{d3} is a prescribed probe voltage, Eq. (3.15) is an implicit expression for T_e ($=e/k\phi$) in terms of the measured quantity V_{d2}. The electron temperature T_e determined from Eq. (3.15) is a smooth, monotonic function of the measured probe voltage V_{d2} (Del Medico, 1992).

The electrode current expressions can also be manipulated, using the Bohm sheath criterion discussed above, to yield the following expression for the electron density n_e:

$$n_e = \frac{\left(\frac{I_3}{A_3}\right)\exp\left(\frac{1}{2}\right)(m_i)^{1/2}}{e(kT_e)^{1/2}\left[\exp(\phi V_{d2}) - 1\right]} \tag{3.16}$$

In Eq. (3.16), V_{d2} and I_3 are measured quantities, m_i is the ion mass, A_3 is the current collection area of electrode 3, and T_e is the electron temperature previously determined via Eq. (3.15).

3.4.2 Quadruple Probe

Another of the multiple electrode probe systems, the quadruple electrostatic probe, is comprised of four sensing electrodes compared with the three electrodes of the triple probe. The quadruple probe, developed originally by Burton, et al., (1993), utilizes the three parallel electrodes of the triple probe with the addition of one perpendicular electrode (see Fig. 2.4). The addition of the fourth electrode allows determination of the ion speed ratio u_i/c_m (=ion directed velocity/ion most probable thermal speed) by the crossed probe technique. The crossed probe theory, which is discussed in section 4.1.4, is used to determine u_i/c_m by measuring the ion currents collected by both the perpendicular electrode and one of the aligned electrodes. The advantage of the quadruple probe is that it provides simultaneous measurements of T_e, n_e and u_i/c_m. The derivations of the crossed probe and quadruple probe theories, appropriately modified for this study to account for a two ion species plasma, are presented in section 4.1.

3.5 Length Scales for the Quadruple Probe used in this Study

The design and operation of the quadruple probe used in this study is based on several length scales determined by the plasma condition in the vicinity of the probe electrodes. For the conditions expected at the exit plane probe location (T_e~0.6 eV, $n_e \sim 4 \times 10^{12}$ cm^{-3}), the Debye length λ_D is ~3×10^{-4} cm and the ratio of electrode radius to Debye length $r_p/\lambda_D \sim 45$, so that the ion sheath surrounding the electrodes can be characterized as thin. For probe

measurements 5 mm downstream, this ratio increases to $r_p/\lambda_D \sim 55$, improving the thin sheath assumption for the downstream measurement locations investigated in this study.

Despite the validity of the thin sheath assumption, the possibility of sheath interactions between adjacent electrodes in the quadruple probe must be investigated (Tilley, et al., 1990). The clearance s between electrodes 1 and 3 (Fig. 2.4) is s~1 mm so that $s/\lambda_D > 250$. Since the sheath thickness is on the order of a few Debye lengths thick, it is clear that sheaths on adjacent quadruple probe electrodes do not interact for the plasma conditions at the arcjet exit.

To avoid strong sensitivity of the ion current to small misalignments between the flow vector and the electrode axis, the so-called end effect parameter τ_L discussed above should be > 50 (Chung, et al., 1975). For the plasma conditions at the probe measurement locations, this parameter is conservatively estimated at $\tau_L > 250$. The electrodes ideally should also be long enough that the Bohm sheath ion current collected along the cylinder length I_b is much larger than the current collected at the probe end due to the convection of charged particles into the probe tip I_t. A first-order analysis of the ratio I_b/I_t [using Eq. (3.14)] from section 3.3.2 shows $I_b/I_t > 30$, so that the error introduced to the collected ion current by neglecting the probe tip current is ~ 3%. By the reasoning in section 3.3.2, the error introduced in the electron current by the probe tip is much smaller.

The radius r_p of the tungsten electrodes (Fig. 2.4) was chosen as a compromise between the thin sheath requirement ($r_p/\lambda_D >> 1$) and the condition of free molecular flow over the probe electrodes ($\lambda_{mfp}/r_p >> 1$). For the seven-species plasma expected at the exit plane (H_2, N_2, H, N, H^+, N^+, e),

all relevant collision mean free paths were calculated. The following assumptions are made in calculating mean free paths: T_e=7000 K, T_g=2500 K, $n_e = 4 \times 10^{12}$ cm^{-3}, and $n_{neutral} = 3 \times 10^{15}$ cm^{-3} with 10% dissociation at the thruster exit. The following worst case electron (e), ion (i), and neutral (n) mean-free-path ratios were calculated: $\lambda_{n\text{-}n}/r_p$=20, $\lambda_{i\text{-}n}/r_p$=5, $\lambda_{i\text{-}i}/r_p$=30, $\lambda_{i\text{-}e}/r_p$=20, $\lambda_{e\text{-}n}/r_p$=20, and $\lambda_{e\text{-}e}/r_p$=30. Clearly, the probe electrodes operate in the collisionless regime. Additionally, λ_{mfp}/λ_D >200 for all collisions, with an overwhelming majority of the collisions having λ_{mfp}/λ_D >1000, indicating that the collisionless sheath assumption is also appropriate.

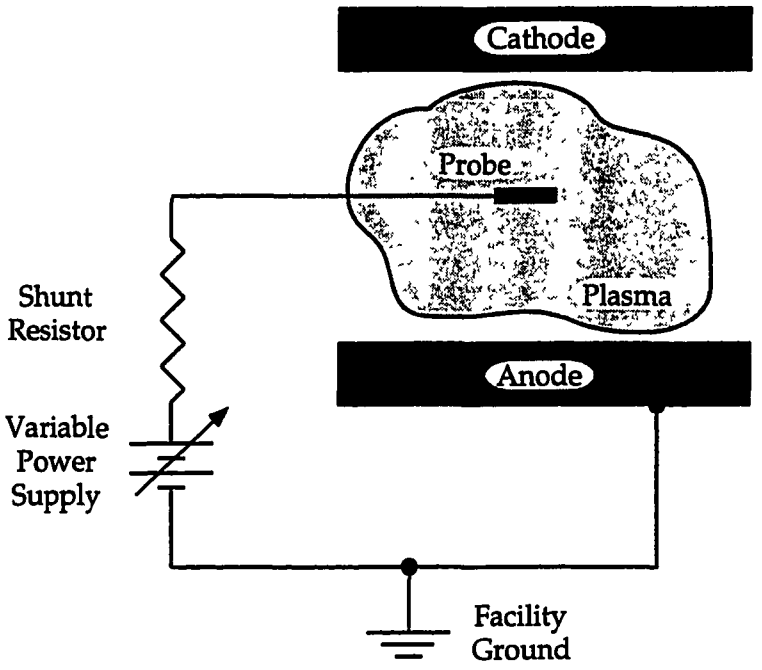

Fig. 3.1 Schematic of a single electrostatic probe showing the simple electrical circuit used for measurements of plasma parameters.

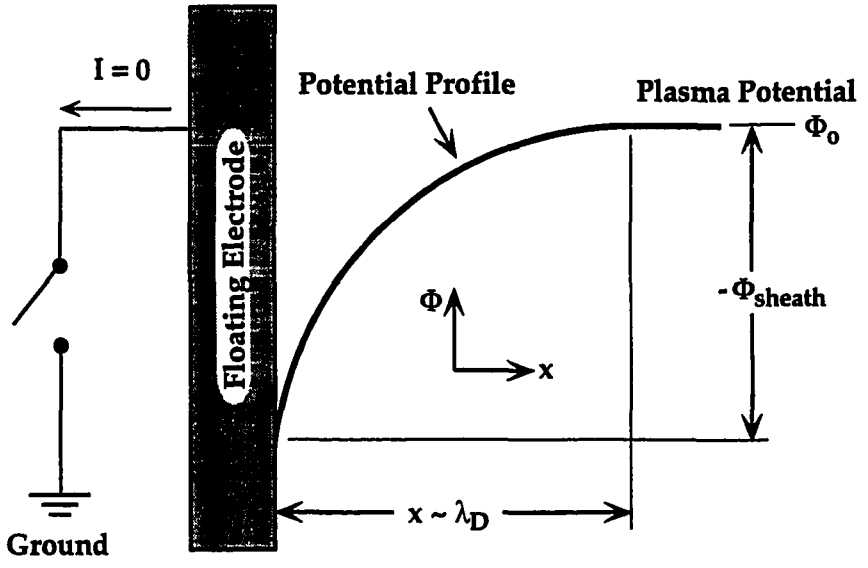

Fig. 3.2 Plot of electrical potential Φ versus distance x demonstrating the perturbing effect of a boundary on the plasma.

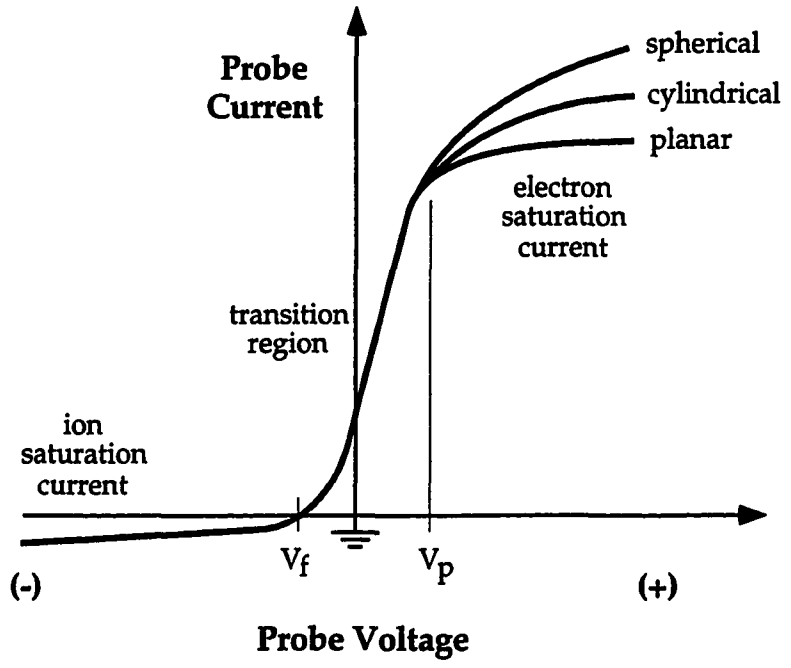

Fig. 3.3 Typical shape of a single probe voltage-current (V-I) characteristic showing the ion saturation, transition, and electron saturation regions.

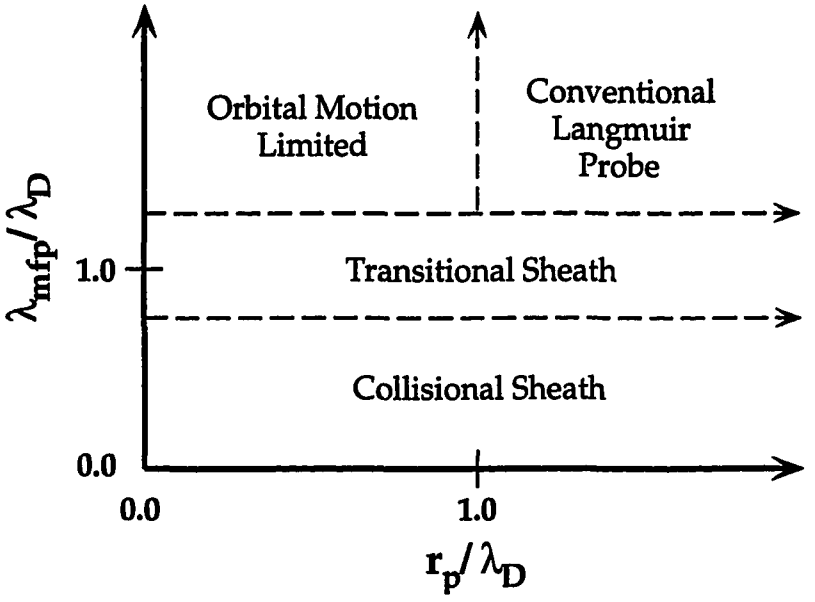

Fig. 3.4 Domains of probe electrode performance. The Orbital Motion Limited and Conventional Langmuir Probe regimes together comprise the collisionless sheath domain (Chung, et al. 1975).

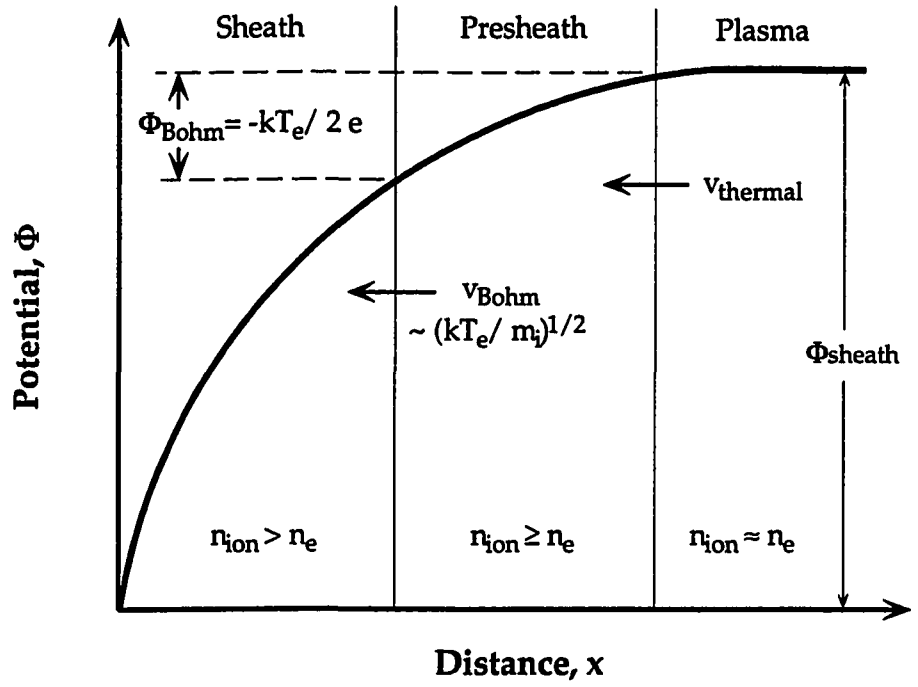

Fig. 3.5 Schematic illustration of the Bohm sheath showing the Bohm velocity v_{Bohm} and the potential drop across the presheath Φ_{Bohm}.

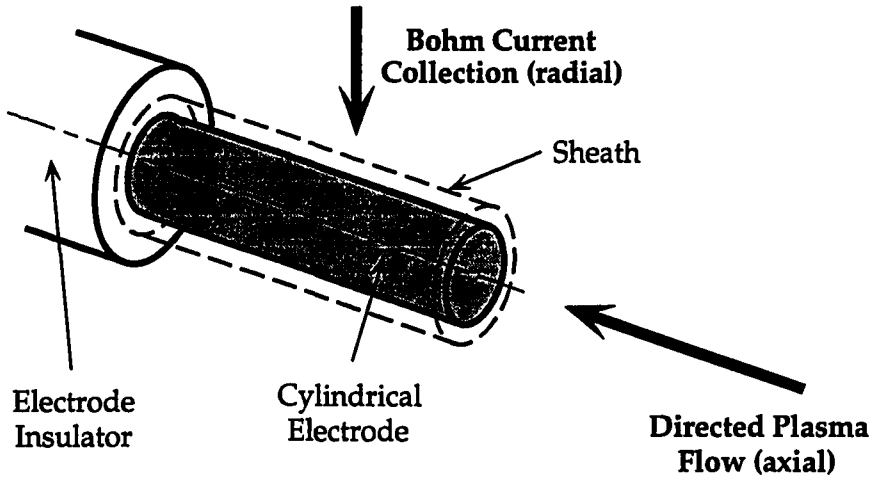

Fig. 3.6 Cylindrical electrostatic probe in a flowing plasma. The Bohm current is collected through the sheath and perpendicular to the electrode.

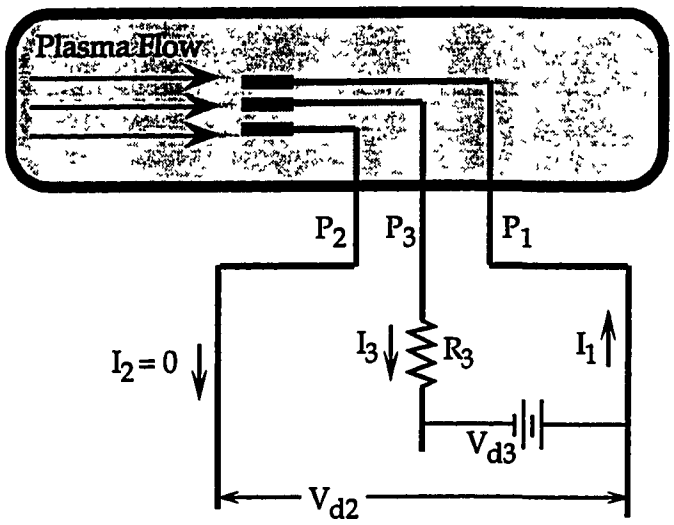

Fig. 3.7 Electrical circuit schematic of the triple electrostatic probe. The current I_3 and voltage V_{d2} are measured quantities and V_{d3} is prescribed.

4. Arcjet Near-field Plume Diagnostics

4.1 Quadruple Probe Theory for a Uniform N_2-H_2 Plasma

Figures 4.1. and 4.2. show an electrical schematic and potential plot of the quadruple probe, consisting of three cylindrical electrodes (P_1, P_2, P_3) which are aligned with the plasma flow vector and one electrode (P_4) which is perpendicular to the plasma flow. P_3 and P_4 are biased at constant voltages V_{d3} and V_{d4} relative to P_1, and P_2 assumes the floating potential V_f of the local plasma (I_2=0). The circuit comprised of electrodes 1, 3 and 4 is electrically floating such that ion current collected at P_3 and P_4 is balanced by the electron current collected at P_1, thereby determining the potential difference V_{d2} [=$V_{d2}(T_e)$]. The three aligned electrodes 1-3 are similar to the triple probe and yield simultaneous measurements of n_e and T_e. The addition of the perpendicular electrode P_4 allows the measurement of the parameter u_i/c_m, determined from the ratio I_4/I_3 for crossed electrostatic electrodes with V_{d3} = V_{d4}. For the quadruple probe, the measured quantities are the electrode currents I_3 and I_4 and the potential difference between electrodes 1 and 2, V_{d2}. Currents I_3 and I_4 are determined by measuring voltage drops across resistors (R_3 = R_4 = 100 Ω). The electrode bias voltages V_{d3} and V_{d4} are provided by batteries, with V_{d3}=V_{d4}=12V.

4.1.1 Derivation of the Quadruple Probe Response

Quadruple probe analysis assumes: 1) The ion sheath surrounding the tungsten wires is thin compared to the wire radius ($r_p >> \lambda_D$); 2) Each probe wire and sheath are collisionless ($\lambda_{mfp} >> r_p >> \lambda_D$); 3) The electron energy distribution is Maxwellian; 4) Velocity slip between plasma species is

negligible; and 5) A wake region of low ion and electron density exists downstream of the perpendicular electrode P_4.

Derivation of quadruple probe response is similar to that of the conventional triple probe (Chen and Sekiguchi, 1965). However, prior to this study all applications of the quadruple probe (Burton, et al., 1993, DelMedico, 1992) concerned single component (argon) plasmas with only a single species of ion present. It is one of the objectives of this work to present the revisions necessary to allow the application of triple and quadruple probe theory to multicomponent (N_2-H_2) plasmas. In the present study, the probe is utilized in a simulated hydrazine ($2H_2+N_2$) plasma, with multiple species of ions present. Single Langmuir probes have been used in nitrogen and hydrogen-based arcjet plumes in the past (Sankovic, 1990, Carney and Sankovic, 1989), but their use is not contingent on knowledge of the species since T_e and n_e are determined primarily by electron current collection. Conversely, use of the quadruple probe requires a more detailed knowledge of the plasma composition, since two of the electrodes collect primarily ion current.

The quadruple probe response is derived by first writing an analytic expression for the current collected at each probe electrode. As in the triple probe technique, the current collected by the three parallel electrodes (P_1, P_2 and P_3) is given by

$$I_1 = A_1 j_e \exp(-\phi V_1) - A_1 j_{i1}(V_1) \tag{4.1}$$

$$I_2 = A_2 j_e \exp(-\phi V_2) - A_2 j_{i2}(V_2) \tag{4.2}$$

$$I_3 = -A_3 j_e \exp(-\phi V_3) + A_3 j_{i3}(V_3) \tag{4.3}$$

where

$$\phi = \frac{e}{kT_e} \tag{4.4}$$

$$j_e = e\, n_e \left(\frac{kT_e}{2\,\pi\, m_e}\right)^{1/2} \tag{4.5}$$

and the parameter ϕV is a non-dimensional electrode potential. The individual electrode voltages $V_{1\text{-}3}$ are defined as the potential differences between the electrode potential and the local plasma potential V_p. These voltages cannot be measured directly, but potential differences (e.g., V_2-V_1) are measurable and are used in the quadruple probe analysis discussed below. The first and second terms in expressions Eq. (4.1)-(4.3) represent the contribution to the collected current from electrons and ions, respectively. The electron contribution consists of the electron saturation current density j_e due to thermal motion of the electrons, reduced by the appropriate exponential Boltzmann factor to account for electron repulsion resulting from the probe bias potential. The contribution of the ions to the total current I is given by the saturation current density j_i. Strictly speaking, j_i is a function of electrode potential since electrode sheath thickness and, hence, electrode current collection area, increase with the magnitude of the negative electrode bias potential. However, in the thin sheath limit, variation in sheath thickness with electrode bias potential is negligible and $j_{i1}=j_{i2}=j_{i3}=j_i$.

The quadruple probe theory presented in this study represents a significant modification of the theory used previously by Burton et. al (1993), in the manner that the current to the perpendicular electrode P_4 is addressed. Rather than utilizing an analytic expression similar to Eq. (4.3) for the current collected at electrode P_4, the current I_4 is related to the current collected at P_3 through the ratio of the measured currents I_3 and I_4 so that

$$I_4 = I_3 \times \left(\frac{I_4}{I_3}\right)_{meas.} \tag{4.6}$$

The quadruple probe is essentially two probes: 1) a triple probe (electrodes 1-3) for determining T_e and n_e (Chen and Sekiguchi, 1965) and 2) a crossed probe (electrodes 3 and 4) for determining the ion speed ratio u_i/c_m (Johnson and Murphree, 1969). Due to the wake effect that is presumed to exist behind the perpendicular electrode, the crossed probe technique requires an assumption regarding the effective current collection area of electrode 4. The significance of Eq. (4.6) is that it completely removes errors in T_e and n_e measurements due to assumptions regarding effective current collection area of P_4. In the present scheme, these assumptions have implications for the ion speed ratio measurement only.

From Figs. 4.1 and 4.2, the following conditions and constraints are apparent:

$$I_1 = I_3 + I_4 \tag{4.7}$$

$$I_2 = 0 \tag{4.8}$$

$$V_{d2} = V_2 - V_1 \tag{4.9}$$

Additionally, electrodes 3 and 4 are equally biased such that

$$V_{d3} = V_{d4} = V_3 - V_1 = V_4 - V_1 \tag{4.10}$$

4.1.2 Electron Temperature Determination

Forming the ratio $(I_1-I_3)/I_4$, along with Eqs. (4.1), (4.3), and (4.6) and $A_1 = A_2 = A_3$, yields the following expression:

$$\frac{I_1 - I_3}{I_4} = \frac{j_e\left[\exp(-\phi V_1) + \exp(-\phi V_2)\right] - 2\, j_i}{\left[j_i - j_e \exp(-\phi V_3)\right] \times (I_4/I_3)_{meas.}} \tag{4.11}$$

From Eqs. (4.2) and (4.8), with j_i independent of electrode potential, the expression for the ion saturation current density is

$$j_i = j_e \exp(-\phi V_2) \tag{4.12}$$

Substituting Eqs. (4.7) and (4.12) into Eq. (4.11) yields the following expression:

$$1 = \frac{\exp(-\phi V_1) + \exp(-\phi V_3) - 2\exp(-\phi V_2)}{(I_4/I_3)\left[\exp(-\phi V_2) - \exp(-\phi V_3)\right]} \tag{4.13}$$

Multiplying the numerator and denominator of Eq. (4.13) by $\exp(\phi V_3)$ and applying Eqs. (4.9) and (4.10) yields the following relation:

$$1 = \frac{1 + \exp(\phi V_{d3}) - 2\exp\left[\phi(V_{d3}-V_{d2})\right]}{(I_4/I_3)\left\{\exp\left[\phi(V_{d3}-V_{d2})\right] - 1\right\}} \tag{4.14}$$

Since V_{d3} is a prescribed probe bias and the quantities V_{d2} and I_4/I_3 are experimentally determined, Eq. (4.14) uniquely determines $T_e = e/k\phi$ as a function of V_{d2} through iteration. The relationship between T_e and the measured potential difference V_{d2} is shown in Fig. 4.3 for the case of an externally applied electrode bias voltage V_{d3} = 12 volts and a current ratio of I_4/I_3 = 0.6. The electron temperature is a smooth, monotonically increasing function of V_{d2} for the 0.5-1.0 eV range of T_e expected in the arcjet near-field plume.

4.1.3 Electron Density Determination

Solving Eq. (4.12) for j_e, substituting into Eq. (4.3), and solving for the ion saturation current density results in the following expression for j_i:

$$j_i = \frac{(I_3/A_3)}{1 - \exp(\phi V_{d2}) \exp(-\phi V_{d3})} \tag{4.15}$$

Equation (4.14) can be solved for $\exp(V_{d3})$ in terms of V_{d2} and T_e and the result applied to Eq. (4.15) so that j_i is given in terms of measured quantities and T_e, which is determined with Eq. (4.14). The resulting expression for the ion saturation current density is

$$j_i = \frac{(I_3/A_3)\,(1 + I_4/I_3)}{\exp(\phi V_{d2}) - 1} \tag{4.16}$$

Eq. (4.16) is used to determine n_e from I_3, I_4 and V_{d2} by relating j_i to the electron density through the Bohm sheath analysis (Chen and Sekiguchi, 1965). As discussed in Chapter 2, the Bohm sheath criterion relates the ion saturation current to T_e, n_e and the ion mass m_i for a single ion species plasma through the following expression:

$$j_i = e\, n_e \left(\frac{kT_e}{m_i}\right)^{1/2} \exp\left(-\frac{1}{2}\right) \tag{4.17}$$

For a plasma with more than one species of collected ion, the Bohm analysis must be modified to account for the collection of each ion species via the Bohm sheath. Assuming that each collected positive ion behaves

independently (i.e., behaves in a collisionless manner) as it accelerates through the Bohm sheath toward the probe, the general expression for j_i becomes:

$$j_i = e\,(kT_e)^{1/2} \exp(-\tfrac{1}{2}) \left[\sum_{j=1}^{\#\,species} \left(\frac{n_j}{(m_j)^{1/2}} \right) \right] \tag{4.18}$$

For the region of the hydrazine arcjet plume of interest, equilibrium codes predict that H^+ and N^+ are the only ion species present in measurable amounts (Nachtrieb, 1993), and the Bohm expression becomes:

$$j_i = e\,(kT_e)^{1/2} \exp(-\tfrac{1}{2}) \left(\frac{n_{H^+}}{(m_{H^+})^{1/2}} + \frac{n_{N^+}}{(m_{N^+})^{1/2}} \right) \tag{4.19}$$

Invoking quasineutrality ($n_e = n_{H^+} + n_{N^+}$), Eqs.(4.16) and (4.19) yield

$$n_e = \frac{\kappa \left(\frac{I_3}{A_3} \right) \left(1 + \frac{I_4}{I_3} \right) \exp\left(\frac{1}{2} \right) (m_{H^+})^{1/2}}{e(kT_e)^{1/2} \left[\exp(\phi V_{d2}) - 1 \right]} \tag{4.20}$$

In Eq. (4.20), the factor κ represents the effect of multiple ion species on the probe response to electron density:

$$\kappa = \frac{1 + \left(\frac{n_{N^+}}{n_{H^+}} \right)}{1 + \mu \left(\frac{n_{N^+}}{n_{H^+}} \right)} \tag{4.21}$$

where $\mu = (m_{H^+}/m_{N^+})^{1/2}$. The functional dependence of κ on the plasma composition is shown in Fig. 4.4. For a plume containing only H^+, $n_{N^+} = 0.0$ and κ reduces to unity, such that Eq. (4.20) reduces to single component (H^+) form. The relationship between I_3 and n_e [Eq. (4.20)] is shown in Fig. 4.5 for several values of T_e and $\kappa = 1.07$, as discussed below.

Experimental observations show that low nitrogen ion densities are found near the exit plane in ammonia and hydrazine arcjets (Hargus, et al., 1994, Keefer, et al., 1994). It is suggested that this is consistent with a plasma dominated by charge exchange collisions in the expanding nitrogen-hydrogen propellant and, as demonstrated in Fig. 4.6, with the preferential dissociation of H_2 ($\varepsilon_d = 4.48$ eV) over N_2 ($\varepsilon_d = 9.61$ eV) (Burton, 1994). The arcjet exit plane plasma is highly dissociated and partially ionized, with $T_e > T_g$, and the estimated range of gas temperature is $T_g < 6000$ K. Dissociation and ionization by electron collisions are negligible, due to low electron density and temperature, and atomic nitrogen rapidly undergoes charge-exchange collisions with hydrogen, the cross-section for which is on the same order of magnitude as N-H momentum transfer collisions. Neglecting radial species diffusion and convective effects, charge-exchange gives $H + N^+ <---> H^+ + N$, and the two charge-exchange reactions balance in steady state. Writing these volumetric collision rates in the form nQv, with relative thermal speeds $v_{H,N} \approx v_H$, and cross sections $Q_{H\text{-}N^+} \approx Q_{N\text{-}H^+}$ gives:

$$\frac{n_{N^+}}{n_{H^+}} = \frac{n_N}{n_H} \tag{4.22}$$

which directly implies a low nitrogen ion density in the exit plane (see Figs. 4.6 and 4.7). Thus, the relative nitrogen ion density is effectively determined

by dissociation through the gas temperature T_g and not the electron temperature. For $T_g < 6000$ K, $n_{N^+}/n_{H^+} < 0.1$ and $\kappa < 1.07$, indicating a less than 7% increase in n_e due to the presence of nitrogen ion probe current.

4.1.4 Crossed Electrostatic Probe Technique

In addition to the quantities T_e and n_e, the quadruple probe also yields the ion speed ratio u_i/c_m, where u_i is the heavy particle directed velocity and c_m is the most probable thermal speed of the collected ions. For a cylindrical electrode oriented at an angle θ relative to the plasma streamline, the collected ion current has been shown to be a function of the quantity $(u_i/c_m)\sin\theta$, where $c_m = (2kT_i/m_i)^{1/2}$ (Kanal, 1964). For the case of two equally biased probes, with one probe aligned with the flow vector and the other one normal to it, the collected ion current ratio for single species ion collection through thin sheaths is (Johnson and Murphree, 1969):

$$\frac{I_4}{I_3} = \frac{2\,A_4}{\sqrt{\pi}A_3} \exp\left[-\left(\frac{u_i}{c_m}\right)^2\right] \sum_{n=0}^{\infty} \left[\frac{\left(\frac{u_i}{c_m}\right)^n}{n!}\right]^2 \Gamma(n+\frac{3}{2}) \qquad (4.23)$$

In order to apply the crossed probe technique to the multicomponent (H_2-N_2) plasmas of interest here, significant revisions have to be made to Eq. (4.23). This study presents a modified theory for the crossed probe method in which an accounting is made for current collection due to *two* ion species (H^+ and N^+). In the original derivation of the crossed probe technique, a maxwellian velocity distribution is assumed for the single component ion collection (Kanal, 1964). For the present study, the collected current ratio expression has been rederived using a two-component form of the Maxwellian velocity

distribution. The derivation follows the single component case, and results in a contribution to the ratio I_4/I_3 from each of the two collected ion species. For the ion species assumed present, the ion composition is defined by $f = n_{H^+}/n_e$ and, since by quasineutrality $n_e = n_{H^+} + n_{N^+}$, $(1-f) = n_{N^+}/n_e$. The resulting expression for the measured current ratio I_4/I_3 is

$$\frac{I_4}{I_3} = C_1 \Bigg\{ f(x_{H^+}) \exp\left[-\left(\frac{u_i}{c_{m,H^+}}\right)^2\right] \sum_{n=0}^{\infty} \left[\frac{\left(\frac{u_i}{c_{m,H^+}}\right)^n}{n!}\right]^2 \Gamma(n+\tfrac{3}{2}) \\ + \mu(x_{N^+})(1-f) \exp\left[-\left(\frac{u_i}{\mu c_{m,H^+}}\right)^2\right] \sum_{n=0}^{\infty} \left[\frac{\left(\frac{u_i}{\mu c_{m,H^+}}\right)^n}{n!}\right]^2 \Gamma(n+\tfrac{3}{2}) \Bigg\} \tag{4.24}$$

where the constant C_1 is given by

$$C_1 = \frac{2\,A_4}{\sqrt{\pi}\,A_3[f + (1-f)\,\mu]} \tag{4.25}$$

In Eq. (4.24), the first term in the brackets { } is the H^+ contribution and the second term is the N^+ contribution to the measured ion current collection. The most probable thermal speed for N^+ (c_{m,N^+}) has been written in terms of c_{m,H^+} (since $c_{m,N^+} = \mu\, c_{m,H^+}$). Note that each of the terms is weighted by the relative density of its corresponding ion [i.e., f and (1-f)].

Because a wake region of low plasma density is formed behind the perpendicular electrode P_4, a portion of the electrode area A_4 does not collect ions. The parameters x_{H^+} and x_{N^+} are the fractions of the electrode geometric area A_4 available for H^+ and N^+ collection, respectively. Because the extent of the wake effect is determined by the relative magnitudes of the directed ion

velocity u_i and the average thermal speeds of the ions, x_{H^+} and x_{N^+} are not necessarily equal. For the conditions anticipated at the thruster exit ($T_g = T_i = 2500$ K, $u_i \sim 6500$ m/s), $u_i/c_{m,H^+} \sim 1$ and $u_i/c_{m,N^+} \sim 4$. The nitrogen ions, with their larger particle mass and lower mobility, have a much lower average thermal speed than hydrogen ions at the same kinetic temperature. Several references discuss the wake effect for high speed flows. Among these are the works by Johnson and Murphree (1969), Poissant and Dudeck (1985) and Burton, et al. (1993). It has been postulated and experimentally verified for an argon plasma at $u_i/c_m \sim 1$, that the wake effect causes the effective collection area to be half of the geometric electrode area (Johnson and Murphree, 1969). Since $u_i/c_{m,H^+}$ is expected to be ~ 1, x_{H^+} is assumed to be 1/2 so that only the front half of P_4 collects ions. For the nitrogen ions, the wake effect reduction in collection area is expected to be more pronounced. Since the directed velocity u_i is several times c_{m,N^+} (i.e., N^+ is "hypersonic"), the nitrogen ions are assumed to be collected by the projected area of the perpendicular electrode only, such that $x_{N^+} = 1/\pi$ (Burton, et al., 1993).

Given an estimate of the plasma composition f, Eq. (4.24) is an expression for $u_i/c_{m,H^+}$ versus the measured current ratio I_4/I_3. Equation (4.24) is plotted in Fig. 4.8 for $0 \le f \le 1$, for the case of $x_{H^+} = 1/2$ and $x_{N^+} = 1/\pi$. Pure H^+ collection is represented by f=1.0, $2H^+ + N^+$ collection by f=0.67, and pure N^+ collection by f=0.

If an independent measure of the directed plasma velocity u_i is known, and if f is known, Fig. 4.8 can be used to determine c_{m,H^+} $[=(2kT_i/m_{H^+})^{1/2}]$ and, hence, the gas temperature $T_g = T_i$. As discussed above, a value of $\kappa = 1.07$ is used in this study, corresponding to a value of f = 0.9. This research

describes plasma velocity measurements leading to an estimate of T_i and, hence, the degree of thermal nonequilibrium (T_g/T_e) at the thruster exit.

4.1.5 Quadruple Probe Measurement Uncertainties

Uncertainties in centerline quadruple probe measurements in T_e and n_e are due to uncertainties in the measured quantities I_3, I_4, and V_{d2} as well as the probe geometry. Of primary concern is the length of the perpendicular electrode (see Fig. 2.4), which measures current I_4 based on a distribution of T_e, n_e and u_i along its 2 mm length. However, the quadruple probe theory has been modified for the present study so that the quantity I_4 enters into the equations for T_e and n_e as a measured input. That is, the functional dependency of I_4 on plasma parameters is not a concern for T_e and n_e quadruple probe measurements, since I_4 is not expressed as an analytic function of T_e and n_e during the development of the quadruple probe expressions for T_e and n_e [Eqs. (4.14) and (4.20)]. Independent quadruple and triple probe measurements confirm this argument, with T_e and n_e results consistent within 5%. This result is not surprising, since in the limit I_4/I_3 --> 0, the quadruple probe equations [Eqs. (4.14) and (4.20)] reduce to the triple probe equations for T_e and n_e. Single Langmuir probe surveys also verify the multiple probe T_e measurements, as described above. Uncertainty in the quadruple and triple probe T_e values is estimated as ± 15%, due to uncertainty in the V_{d2} measurement, and to assumptions in the quadruple and triple probe analyses. An uncertainty of ± 17% in the ratio I_4/I_3 only results in a ± 4% sensitivity in T_e in Eq. (4.14).

Experimental uncertainty in n_e results from the determination of electrode surface area, the current I_3, propagated uncertainty in T_e, and

fundamental assumptions in the quadruple and triple probe theories. It is generally accepted that, due to these assumptions (e.g., the Bohm sheath model for current collection), the uncertainty in n_e measurements is at best ± 50% (Tilley, et al., 1990). As such, minor uncertainties due to measured quantities like the currents I_3 and I_4 and the potential V_{d2} are negligible compared with the uncertainties associated with the quadruple probe assumptions for the determination of n_e.

Uncertainty in the ion speed ratio $u_i/c_{m,H^+}$ measured by the quadruple probe is determined by estimates in the plasma composition factor f ($=n_{H^+}/n_e$), uncertainties associated with the crossed probe theory, and in some cases, uncertainties associated with the measured quantity I_4/I_3. The error due to variations in the plasma composition can be bounded by considering realistic limits of the factor f. For f ranging from 0.7 (2:1 hydrazine composition ratio of H and N) to 1.0 (pure H^+ collection), the uncertainty in $u_i/c_{m,H^+}$ about the assumed value of f=0.9 is ± 10%.

Uncertainty in $u_i/c_{m,H^+}$ measurements can also be attributed to errors in assumptions in the development of the crossed probe technique. The ion current collection expressions developed by Kanal (1964) and Johnson and Murphree (1969), and extended to multiple ion species collection in the present study, neglect variation of the sheath geometry due to the plasma flow past the perpendicular electrode. Additionally, the extent of the wake effect and uncertainty in the appropriate current collection area of electrode 4 further complicate the issue. A conservative estimate of the errors introduced by these assumptions in the crossed probe theory yields an additional ± 10% uncertainty. Physical measurement of the quantities I_3 and

I_4 are certain to within a few percent, giving an overall root-mean-square uncertainty of ± 15% for quadruple probe measurements of $u_i/c_{m,H+}$.

The uncertainty analysis discussed above pertains to quadruple probe measurements made at the thruster centerline. For off-centerline positions, where the probe electrodes 1-3 are not aligned with the plasma flow divergence angle and radial gradients exist over the width of the probe, the uncertainties are expected to be somewhat larger. As such, results are presented in this work only for regions near the thruster centerline (r<3 mm).

4.2 Quadruple Probe Theory for Plasma Gradients

Quadruple probe measurements at the thruster exit plane show smooth symmetric profiles for the measured electrode currents I_3 and I_4, as shown by Fig. 5.13 in Chapter 5. However, the measured quantity V_{d2} has a very asymmetric profile, which can be shown to be a result of the steep radial gradient in n_e off-axis, and to a lesser extent, the radial gradient in T_e. These gradients are perpendicular to the quadruple probe electrodes and the arcjet thrust axis. The asymmetric behavior of the V_{d2} signal results as the individual electrodes of the quadruple probe are swept through the parabolic T_e and n_e profiles that occur at the thruster exit. Due to the 1.4 mm separation between electrodes 1 and 2, each probe electrode sees a different local T_e and n_e, as demonstrated in Fig. 4.9. This research will present a modified quadruple probe model that accounts for these radial T_e and n_e gradients that are transverse to the probe electrode axes.

4.2.1 Influence of T_e and n_e Radial Gradients

To derive the quadruple probe response in the presence of radial T_e and n_e gradients, the individual electrode current equations discussed in section 4.1 [Eqs. (4.1)-(4.3)] are first rewritten in terms of the local plasma parameters (T_e, n_e) at each electrode:

$$\frac{I_1}{A_1} = e\, n_{e1} \left(\frac{kT_{e1}}{2\pi m_e}\right)^{1/2} \exp\left(\frac{-eV_1}{kT_{e1}}\right) - \frac{e\, n_{e1}}{\kappa} \left(\frac{kT_{e1}}{m_H}\right)^{1/2} \exp\left(-\frac{1}{2}\right) \tag{4.26}$$

$$\frac{I_2}{A_2} = e\, n_{e2} \left(\frac{kT_{e2}}{2\pi m_e}\right)^{1/2} \exp\left(\frac{-eV_2}{kT_{e2}}\right) - \frac{e\, n_{e2}}{\kappa} \left(\frac{kT_{e2}}{m_H}\right)^{1/2} \exp\left(-\frac{1}{2}\right) \tag{4.27}$$

$$\frac{I_3}{A_3} = -e\, n_{e3} \left(\frac{kT_{e3}}{2\pi m_e}\right)^{1/2} \exp\left(\frac{-eV_3}{kT_{e3}}\right) + \frac{e\, n_{e3}}{\kappa} \left(\frac{kT_{e3}}{m_H}\right)^{1/2} \exp\left(-\frac{1}{2}\right) \tag{4.28}$$

In Eqs. (4.26)-(4.28), the first and second terms represent current due to electron and ion current collection, respectively. The numeric subscripts on T_e and n_e denote the local value of those parameters at each of the electrodes (1-3) of the quadruple probe. The term κ is dictated by the plasma composition, as defined by Eq. (4.21) in terms of H^+ and N^+ number densities.

4.2.2 Probe Response to Specified T_e and n_e Profiles

As a demonstration of how radial gradients manifest themselves in the quadruple probe response, Eqs (4.26)-(4.28) are rearranged to solve explicitly for the quantities V_{d2} and I_3 in terms of $T_e(r)$ and $n_e(r)$. Since electrode 2 is electrically floating (Fig. 4.1), the net current collected is $I_2 = 0$ and Eq. (4.27) can be solved explicitly for the potential V_2:

$$V_2 = -\frac{kT_{e2}}{e} \ln(C_2) \tag{4.29}$$

where the constant C_2 is given by

$$C_2 = \frac{\exp(-1/2)}{\kappa}\left(\frac{2\pi m_e}{m_H}\right)^{1/2} \tag{4.30}$$

Since electrode 2 is not influenced by any other electrodes, and because n_{e2} cancels in the above equation, the value of V_2 is determined by T_{e2} only.

Using Eqs. (4.26) and (4.28), an expression similar to Eq. (4.29) can be derived for the potential V_1. Forming the ratio given by Eq. (4.11) and neglecting the electron current drawn by the ion attracting electrode 3, Eqs. (4.6), (4.26), (4.28) can be solved to yield the following expression for V_1:

$$V_1 = -\frac{kT_{e1}}{e}\ln\left[\frac{C_2\left(\frac{I_4}{I_3}+1\right)\left\{n_{e1}(kT_{e1})^{1/2} + n_{e3}(kT_{e3})^{1/2}\right\}}{n_{e1}(kT_{e1})^{1/2}}\right] \tag{4.31}$$

Recall that the current ratio I_4/I_3 is measured, the constant C_2 is given by Eq. (4.30), and κ is a function of the plasma composition, as discussed above.

For specified T_e and n_e radial profiles, the quadruple probe gradient model (Eqs. (4.28)-(4.31)) is summarized symbolically below:

$$V_2 = V_2\,(T_{e2}, \kappa) \tag{4.32}$$

$$V_1 = V_1\,(T_{e1}, T_{e3}, n_{e1}, n_{e3}, I_4/I_3, \kappa) \tag{4.33}$$

$$V_{d2} = V_2 - V_1 \tag{4.34}$$

$$I_3 = I_3\,(T_{e3}, n_{e3}, \kappa) \tag{4.35}$$

Equations (4.32)-(4.35) can be used to predict the extent to which a non-uniform plasma influences the quadruple probe response. Figure 4.10 displays the predicted V_{d2} versus radial position for the quadruple probe of

Fig. 2.4, for flat and Gaussian n_e and T_e radial profiles. In the case of a uniform plasma (i.e., constant $T_e(r)$ and $n_e(r)$), the predicted V_{d2} response is flat, as expected. For Gaussian n_e and constant T_e, V_{d2} increases monotonically across the thruster face. For a Gaussian T_e distribution broader than n_e, the V_{d2} profile shows more asymmetry. To gain a clearer understanding of the cause of the asymmetry in V_{d2}, the constant T_e case can be solved analytically for V_{d2}, $=V_2-V_1$, giving:

$$V_{d2} = \frac{kT_e}{e} \ln\left[\left(1 + \frac{I_4}{I_3}\right)\left(\frac{n_{e3}}{n_{e1}}\right) + 1\right] \tag{4.36}$$

In this equation the effect of the density gradient can be clearly seen. As the swept probe starts outside the plume and enters it, $n_{e3}/n_{e1} < 1$. At the axis $n_{e1} = n_{e3}$, and as the probe leaves the plume, $n_{e3}/n_{e1} > 1$. The result [Eq. (4.36)] is a monotonically increasing V_{d2} across the thruster face.

4.2.3 Extracting $T_e(r)$ and $n_e(r)$ from Raw Probe Data

Given arbitrary profiles of $T_e(r)$ and $n_e(r)$, we see that $V_{d2}(r)$ and $I_3(r)$ can be predicted (Fig. 4.10). The inverse problem, of extracting n_e and T_e profiles from measured V_{d2} and I_3, can also be solved. Since V_{d2} [Eq. (4.34)] is a strong function of T_e, and I_3 [Eq. (4.35)] is a strong function of n_e, there is sufficient uncoupling that an iterative routine can be used to find the unique $T_e(r)$ and $n_e(r)$ profiles which produce the traces of V_{d2} and I_3 measured by the quadruple probe. Despite the large off-axis radial gradients in T_e and n_e, the uniform plasma quadruple probe equations [Eqs. (4.14) and (4.20)] can be used to determine *centerline* values by taking advantage of the symmetry of the plume. Starting with these measured centerline T_e and n_e values and an initial guess for the n_e radial profile, an iterative routine can be used to march

the probe position across the thruster face while generating a new T_e profile. This T_e profile is used with Eq. (4.35) to update $n_e(r)$, and the process is repeated until both radial profiles converge. As shown in Fig. 4.11, the quadruple probe is approximated during this "marching" technique by assuming that the locations of all four probe electrodes are collinear. This assumption is warranted by the symmetry of the arcjet and the parabolic nature of the expected profiles. This technique is summarized by the steps outlined below with reference to Fig. 4.11. These procedures are separately applied to each radial half of the plume.

Step 1: Calculate T_e and n_e from centerline measurements of I_3, I_4, and V_{d2} using quadruple probe theory for a uniform plasma Eqs. (4.14) and (4.20).

Step 2: Generate a Gaussian profile, with a centerline value determined in Step 1, which is to be used as the initial guess for the shape of the radial profile of n_e.

Step 3: For the most recent profile of $n_e(r)$, march the quadruple probe across the region, away from the centerline, as shown in Fig. 4.11. A value of T_e is calculated via Eq. (4.34) and the measured data I_3, I_4, and V_{d2} at each new location occupied by the leading edge of the probe (electrode 1 in Fig. 4.11). This "marching" procedure is continued in 0.7 mm increments (=0.5 x probe width) until the probe position reaches the end of the measured data at a point far past the edge of the thruster exit. The electron temperature calculated in the first increment in Step 3 (increment #1 in Fig. 4.11) depends on T_{e3} (=T_{e4}) and T_{e1}, which are both initially unknown. Therefore a value of $T_{e3} = (T_{e1}+T_{e2})/2$ is assumed for the first spatial increment only. This is

not required for all subsequent spatial increments, since the only unknown is the electron temperature T_{e1} at the leading edge of the probe. This approximation for $T_{e3,4}$ is only necessary for the initial pass through this procedure for the first half of the plume examined.

Step 4: Update the $n_e(r)$ profile using Eq. (4.35), the measured quantities I_3 and I_4, and the latest radial profile of T_e calculated above in Step 3. Typically five numerical iterations are required to reach convergence.

Step 5: Repeat Step 3 until the calculated profiles of $T_e(r)$ and $n_e(r)$ are unchanged from the previous iteration.

The procedure described in Steps 1-5 above is used separately for the two regions of the plume on each half of the thruster çenterline. The resulting half-profiles for T_e and n_e are combined to form the full radial profiles of these parameters. Results of this iterative process for a typical quadruple probe sweep are shown in Figs. 4.12 and 4.13 for an axial location of 2.2 mm. These data correspond to the $P/\dot{m}$=22.4 MJ/kg case (see Table 2.1) investigated in this study. The initial guess for the $n_e(r)$ is a Gaussian profile as shown in Fig. 4.12. The n_e radial profile converges in fewer than five iterations. For the sake of this discussion, results of the procedure are presented over the range r<6 mm. However, T_e and n_e data are valid only near the thruster centerline (r<3 mm) since the misalignment between the probe electrodes and the flow divergence convolutes the results for larger radii. Results of this iterative process for T_e are shown in Fig. 4.13. Like the n_e results above, the electron temperature profile converges after fewer than five iterations. These results indicate that the T_e profile is much wider than

the n_e profile and nearly uniform at the centerline temperature. However, Tilley, et al. (1994) have shown that misalignments between a triple probe and the plasma streamlines can artificially inflate the measured values of T_e. They noted that a 30° misalignment caused a ~6% increase in the indicated T_e. Based on these results, it is likely that the actual T_e radial profile is slightly concave downward.

Despite the uncertainties in T_e and n_e due to probe misalignment, it is apparent from the above results that the asymmetry in the measured quadruple probe response V_{d2} can be accounted for by radial gradients over the probe width. Further, these radial gradients are a result of fairly symmetric, or normal, profiles of T_e and n_e.

4.2.4 Effect of Plasma Potential Radial Gradients

We have so far considered the effect of radial gradients in T_e and n_e on V_{d2}, which produce a large non-intuitive asymmetry in the measured quadruple probe response. However, an effect can also be produced by a gradient in plasma potential V_p in the radial direction, since the individual electrode potentials ($V_{1\text{-}4}$) are defined relative to the plasma potential. The general triple and quadruple probe theories assume zero gradient in V_p, strictly true only on-axis. Figure 4.14 shows a potential plot (see Fig. 4.2) for the quadruple probe with non-zero plasma potential gradient. Because the negative biasing voltages V_{d3} ($=V_3-V_1$) and V_{d4} ($=V_4-V_1$) are large, small changes in V_p have little effect on the ion current drawn at electrodes 3 and 4. However, the T_e ($V_{d2}=V_2-V_1$) measurement can be affected by a radial gradient in the plasma potential. In Fig. 4.14, the local plasma potential at electrodes 1 and 2 is V_{p1} and V_{p2}, respectively. For this case, the actual

potential difference V_{d2} is related to the measured potential difference $(V_2 - V_1)_m$ through the difference in the local plasma potentials $(V_{p2} - V_{p1})$ by

$$V_{d2} = (V_2 - V_1)_m - (V_{p2} - V_{p1}) \tag{4.37}$$

so that the measured quantity $(V_2 - V_1)_m$ can be a misleading representation of the electron temperature $[T_e = T_e(V_{d2})]$.

4.3 Time-of-Flight Electrostatic Probe Velocimetry

In addition to T_e and n_e, quadruple probe measurements also yield the ion speed ratio $u_i/c_{m,H+} = u_i/(2kT_i/m_{H+})^{1/2}$. Ion speed ratio measurements, when coupled with independent heavy particle velocity u_i measurements, can be used to estimate the heavy particle temperature $T_g = T_i$. Through the course of this research, a time-of-flight velocimetry technique for measuring spatially resolved axial velocities in arcjet plumes has been designed and implemented. In this method, a short duration current deficit pulse is superimposed on the arcjet operating current, thus "tagging" the plasma flow. The effect of the arcjet current pulse is convected downstream and monitored by an electrostatic time-of-flight probe comprised of two individual electrodes. The temporal separation of the two electrode signals and the known axial electrode separation are used to determine the axial plasma velocity.

4.3.1 Background

The technique utilized in the present study is derived from previously-developed optical time-of-flight methods called Emission Ripple Velocimetry (ERV) (Spores, et al. 1992) and Current Modulation Velocimetry (CMV) (Pobst, et al., 1993, 1994). Both of these methods were developed and utilized

on a 1-kW NASA Lewis Research Center arcjet operating on hydrogen propellant. These techniques are optical in nature, and infer velocity by monitoring fluctuations in the plasma plume emission at two axial observation positions. In particular, line-of-sight measurements of fluctuations in emitted hydrogen Balmer-alpha radiation are made with photomultiplier tubes (PMT's) at different axial measurement locations.

In ERV, fluctuations in the plume radiation due to the 16 kHz, ±10% current ripple inherent in the arcjet power processing unit (PPU) (see section 2.1.2) are monitored by a PMT at a position downstream of the thruster exit. The PMT signal shows a "sawtooth" signal, which is in phase with the PPU current ripple except for the time required for the plasma to convect from the cathode tip to the observation location. The measured time delay is used with the axial location of the PMT to determine the average plasma axial velocity between the cathode and the measurements location.

Although the ERV technique was relatively simple to implement, the relatively large period of the arcjet PPU current ripple (~60 μs) compared with the expected signal time delay (~3 μs) compromised the resolution of the convective time delay measurement. Additionally, the resolution of the measurement was compromised by the use of only one PMT. As an improvement to ERV, the Current Modulation Velocimetry (CMV) technique was developed by Pobst, et al. (1993). In this method, a short duration (~ a few μs) current pulse is superimposed on the arcjet current. This pulse momentarily decreases the arcjet current by diverting 20-30% of the arcjet current into a resistive-capacitive (RC) circuit that is in parallel with the arcjet. Immediately after its charging period of a few RC time constants, the RC circuit caused a sharp positive ring in the arcjet current as the

capacitor discharged and the excess current was routed back into the arcjet. The current pulse shape observed by Pobst, et al. was very similar in behavior to the current pulse shown in Fig. 4.17. This process effectively "tagged" the plasma flow at the cathode tip, or the arc-heating region. It was the effect of this current pulse on the hydrogen Balmer a radiation that was monitored with PMTs in a manner similar to that used in ERV.

In the CMV studies two PMTs were utilized, which were separated by a fixed distance along the axis of the thruster. Each sensor recorded an increase in the measured radiation signal as the tagged flow convected past each of the PMT line-of-sight measurement locations. Pobst, et al. (1994) argued that the positive ring of the arcjet current spike (Fig. 4.17) caused a momentary increase in electron recombination which populated the uppermost energy levels. These electrons, it was believed, cascaded downward in energy level, giving off radiation consistent with each respective electron energy level transition. In the CMV technique, only changes in hydrogen Balmer-alpha radiation were monitored by using PMTs, hydrogen Balmer-alpha notch filters and the appropriate optics. While optically monitoring the effect of the electron recombination usually proved useful in measuring plasma velocities with the CMV technique, it was noted that the positive ring of the current modulation did not always trigger the electron cascade phenomenon necessary to cause the requisite Balmer-alpha emission. In fact, it was found that for hydrogen arcjet operating voltages below a certain minimum voltage, the CMV technique described above did not work, despite the presence of the current pulse. The CMV technique used by Pobst, et al. (1993, 1994), while non-intrusive, is a line-of-sight optical technique that precludes the direct

measurement of spatially resolved axial velocities. The measured velocity is a radially integrated value over the PMT line-of-sight.

With significant modifications, the velocimetry technique based on CMV has been made spatially resolved in this study by implementing electrostatic time-of-flight probes. In doing so, the need to Abel-invert the data as required by previous line-of-sight optical methods has been eliminated. The electrostatic probe approach affords several advantages over CMV: 1) It is very low-cost and relatively robust, 2) Measurements can be spatially resolved, allowing measurements of axial velocity radial profiles, 3) Momentary changes in basic plasma parameters (T_e, n_e, etc.) can be monitored to indicate passage of the tagged flow, and 4) Successful velocity measurements are not contingent upon causing observable radiation via electron cascade, a problem encountered by Pobst, et al. (1994) with the CMV technique. For this research, a new electrostatic probe velocimetry method has been developed and implemented for plasma axial velocity measurements at the exit plane of a 1-kW arcjet operating on simulated hydrazine. The new method combines arcjet current pulse technology similar to that used in CMV with the time-of-flight electrostatic probe discussed in section 2.4.

Monitoring natural fluctuations in the ion saturation current has been previously suggested as a means of using time-of-flight electrostatic probes to measure velocities in perturbed plasma flows (Habiger, 1993, and Hoell, 1971). This method is implemented in the present study, but instead is used with artificially supplied current fluctuations. The two time-of-flight probe electrodes (Fig. 2.8) are biased sufficiently positive with respect to the plasma potential V_p such that they measure the local electron saturation current.

The collected electron saturation current j_e is proportional to the local electron density and temperature (i.e., $j_e \sim n_e(T_e)^{1/2}$). In previous work, Sankovic (1990) showed that, for a 1-kW hydrazine arcjet, the electron density in the plume (~10 cm from nozzle exit) was a strong function of the thruster specific power. More specifically, it was demonstrated with steady state measurements that a 20% decrease in arc current caused nearly a 30% change in the measured electron density. Therefore, superimposing a current pulse on the steady arcjet operating current is expected to cause a measurable fluctuation in the measured saturation current, through changes in T_e and n_e as the tagged flow passes each electrode.

4.3.2 Description of the Time-of-Flight Method

The arcjet power processing unit (PPU) produces current with a high frequency ripple (~ 16 kHz, ± 10% about the mean, see Fig. 2.2) which causes "natural" fluctuations in n_e and T_e. These inherent fluctuations are difficult to utilize due to their long period (~ 60 μs), compared with the expected convective time delay of the TOF probe (~ 1 μs). Instead, fluctuations are artificially introduced to the arcjet plasma flow by superimposing a short duration (~ few μs) current deficit pulse on the arcjet operating current. The effect of the current deficit pulse on electron saturation current is monitored at each of the two time-of-flight electrostatic probe electrodes.

The circuit used to modify the arc current is similar to that used in previous CMV studies (Pobst, et al. 1994) and is shown in Fig. 4.15. The current pulse is initiated by closing a switch to a fast RC circuit in parallel with the arcjet, causing a sudden decrease in arc current while the capacitor charges. This short duration (~ 4 μs) current deficit results in a "tagging" of

the plasma in the arc-heating region near the cathode tip. Switch closure is accomplished with an IRF-350 field-effect transistor (FET), which is closed by the gate pulse supplied by a HP214A pulse generator shown in Fig. 4.15. Originally, the RC circuit element was replaced by a 20-30 Ω single resistor, but ringing on the edges of the resulting square current pulse obscured the desired time-of-flight probe signals.

Spatially resolved axial velocities are measured by triggering the arcjet current deficit pulse at several different TOF probe locations. Since the probe is swept radially through the plume during the experiment, it is necessary to trigger the current deficit pulse repeatably at each desired radial location. Probe location is measured by monitoring the voltage of a precision potentiometer (Fig. 4.15) which has been calibrated against the arcjet anode for probe position. The position (voltage) of the desired measurement location is set at the voltage comparator circuit, so that a trigger signal is issued to the HP214A pulse generator when the probe reaches the desired radial location. In turn, the pulse generator supplies a square pulse to "close" the FET and initiate the arcjet current deficit. Because 1) the gate pulse must be positive (relative to the FET voltage), and 2) the arcjet cathode (and FET) operates at ~ 100 V below anode ground, the FET Driver Circuit (Fig. 4.15) is a necessary buffer between the FET and the HP pulse generator. Since the probe is swept relatively slowly (~ 20 cm/s), the probe location is effectively "frozen" during the ~ 3-4 μs elapsed time between the initial trigger and the monitoring of the tagged plasma at the TOF electrodes.

4.3.3 Effect of the Current Pulse on Arcjet Operation

The effect of the time-of-flight current pulse on the 1-kW hydrazine thruster used in this study is demonstrated in Fig. 4.16, which shows the arcjet current I_{arc} and voltage V_{arc} versus time during a typical pulse. The current drops suddenly as the FET switch closes (Fig. 4.15) and the 0.1 μF capacitor begins to charge. As the capacitor nears the end of the charge cycle (a few 1 μs RC time constants), the current through the FET leg of the circuit decreases so that the arc current resumes the normal PPU ripple after a small positive ring. The width of the arcjet current deficit pulse is ~ 4 μs. The nature of the behavior of V_{arc} is not immediately clear from Fig. 4.16. However, the derivative of the arc current (dI_{arc}/dt) has the same qualitative behavior as V_{arc}, implying an inductive effect resulting from the arcjet geometry and/or the pulse circuitry. It is also possible that the arc cools down during the current deficit pulse, temporarily increasing the plasma resistivity and causing the arc voltage to overshoot until the plasma recovers its original pre-pulse temperature.

The behavior of the arcjet current I_{arc} during the current pulse used in this study (Fig. 4.16) was qualitatively very different from the current pulse observed by Pobst, et al. (1994) in their hydrogen arcjet CMV work. This is in spite of the inherent similarity between the current pulse circuits and arcjet geometries used in the two studies. Pobst, et al. observed a narrow positive current spike of several amps immediately before the thruster current resumed its normal PPU ripple. This phenomenon was not observed during the pulses used in the axial velocity measurements presented here. During the present study, the current pulse was always triggered at the same phase of the PPU ripple, which was ~ 4 μs after the peak of the current ripple.

However, in an attempt to measure the dependence of the measured velocity on the location of the current pulse relative to the PPU ripple, an arcjet current trace was observed which was qualitatively similar to that demonstrated by Pobst, et al. (1994). The resulting pulse, demonstrating the large positive ring in the current similar to that seen by Pobst, et al., is shown in Fig. 4.17. In this instance, the only difference between the pulses shown in Figs. 4.16 and 4.17 is that one was triggered near the top of the PPU current ripple, while the other was initiated near the minimum of the ripple.

It was suspected that the change in the pulse characteristics shown in Figs. 4.16 and 4.17 was caused by the extinction of the plasma during the latter pulse (Fig. 4.17). It was hypothesized that this was due to the current passing below the minimum threshold necessary to sustain the plasma during the pulse in question. To investigate this phenomenon, experiments were conducted in which the arcjet was intentionally extinguished while the thruster voltage and current were measured. The results of this experiment are shown in Fig. 4.18, which demonstrates the effect of turning off the thruster PPU on the arcjet operating voltage and current. The power supply was manually turned off at time t~70 μs. For the next ~ 100 μs, the current supplied to the arc decreases nearly linearly while the arc voltage increases gradually, a consequence of the negative impedance characteristic of arc discharges. When the current reaches ~2.5 amps, the electron density has decreased to the point where conductivity of the gas in the constrictor is too low to sustain the arc discharge and the plasma extinguishes. The location of this plasma extinction threshold was repeatable over several repetitions of this experiment. During the plasma extinction process, the increasing

impedance of the plasma causes a sudden increase in the arc voltage before it gradually decreases to the open circuit voltage of the PPU of ~ 170 volts.

The results of the plasma extinction experiments discussed above account for the differences in the varying behavior of the arcjet depicted in Figs. 4.16 and 4.17. When the current pulse is triggered at the top of the PPU ripple, the current deficit does not decrease the thruster current to the plasma extinction threshold shown in Fig. 4.18. When the pulse is triggered near the PPU ripple minimum, which is ~ 2 amps below the PPU current maximum, the current deficit results in a net current that is temporarily below the threshold necessary to sustain the plasma. The pulse shown in Fig. 4.17 shows that the plasma extinguishes for ~10 μs prior to the positive ring of the current, before the plasma restarts and the PPU resumes its normal ripple behavior. It is interesting to note that, despite the momentary absence of a plasma in the thruster constrictor, the plasma re-establishes itself the moment that the PPU current is resumed. A cold arcjet requires a 4000 volt starting pulse to generate electrons with energies large enough to initiate the plasma. Considering this, Fig. 4.17 is strong evidence that the cathode tip is thermionically emitting enough electrons such that the plasma restarts immediately when the PPU current is resumed, without the necessity of a large starting voltage.

4.3.4 Broadening of the Current Deficit Pulse

An analytical investigation of the effect of the plasma acceleration processes in the arcjet on the width of the current deficit pulse has been performed for this study. Using computational model predictions of the centerline axial velocity generated by Megli (1995), a distance versus time (x-t)

diagram of the plasma flow between the arcjet constrictor and the time-of-flight measurement location was generated. The details of this work are described below.

Figure 4.19 shows the axial velocity in the arcjet predicted by Megli (1995) for a 1-kW hydrazine thruster operating at 10 amps and 50 mg/s of propellant. Axial velocity results are shown along the thruster centerline and along a line 12° from the centerline, drawn from the constrictor. The centerline velocity data shown in Fig. 4.19 represent the axial velocity distribution u(x) in the thruster interior. Since u(x)=dx/dt, the velocity data can be integrated according to

$$t(x) = \int_{x_o}^{x} dt = \int_{x_o}^{x} \frac{dx}{u(x)} \tag{4.38}$$

resulting in an expression t(x) for the time required for a parcel of plasma to travel from the cathode tip ($x=x_o$) to some downstream axial position x. The integration shown in Eq. (4.38) was performed on a curve fit of the data in Fig. 4.19, using an initial condition consistent with the model prediction of ~800 m/s at the cathode tip x_o. Experimental results for a 1-kW hydrogen thruster have shown that the centerline axial velocity decreases slightly with distance from the thruster exit plane (Pobst, et al., 1993). Assuming similar behavior for the hydrazine thruster, the slope of u(x) predicted by the model at the exit plane was used to extend the axial velocity profile into the plume. As shown below, this assumption has a negligible effect on the results of this analysis.

The results of Eq. (4.38) are presented in Fig. 4.20, which shows an x-t diagram of the plasma as it flows downstream from the cathode tip. If the arc

is assumed to attach at x~1.5 mm downstream of the constrictor exit, the length of the arc-heating region is approximately 2 mm. The solid line represents the motion of a parcel of plasma that originates at the cathode tip at time t=0. The dashed line denotes a similar motion, but it represents plasma that was at the cathode tip at t~ -0.4 μs and resides at the end of the arc heating region (x=2 mm) at time t=0. Figure 4.20 indicates that the thruster residence time of any plasma on axis is less than 2 μs. At any given axial location x, the temporal separation of the two curves represents the width (in time) of an instantaneous current pulse applied to the plasma over the length of the arc-heating region. At the axial location of the time-of-flight probe (x~16 mm) this width is Δt~0.4 μs. Based on these results, one would expect a current pulse of a given width to stretch in time no more than ~0.4 μs by the time it reached the axial location of the TOF probe. Examination of the shape of the x-t curves reveals that this Δt is determined primarily by the initial acceleration of the plasma in the region 0<x<1.5 mm. In fact, because the flow decelerates for x>1.5 mm, the temporal width of the current pulse is decreasing when it reaches the time-of-flight probe.

4.3.5 TOF Data Reduction

The TOF probe response is shown in Fig. 4.21 for a typical centerline axial velocity measurement. The signal measured at the downstream electrode has been scaled to account for the lower electron current (lower T_e and n_e) 5 mm downstream of the upstream electrode. Both the upstream and downstream electrodes show noise beginning at t ~ 2 μs that corresponds with the action of closing the FET switch (Fig. 4.15). Approximately 3 μs later, the effect of the arcjet current pulse is monitored as a decrease in the electron

current measured by the upstream electrode. After a time delay of several hundred nanoseconds for the tagged flow to traverse the 5 mm electrode separation, a similar decrease is noted at the downstream electrode. For both of the signals, the width of the decrease in the measured electron current is ~ 4 μs, approximately the same as that of the current deficit pulse.

Axial velocities are inferred from the convective time delay demonstrated in Fig. 4.21 and the known separation (5.0 mm) between the two TOF electrodes. The time delays are derived from the probe response using the temporal separation between the minima (due to the decrease in electron current) measured at each electrode. This is accomplished by taking the derivative of each (smoothed) signal as shown in Fig. 4.22. The difference in the locations of the zero crossings is interpreted as the time required for the tagged flow to travel the 5.0 mm electrode separation.

4.3.6 TOF Probe Measurement Uncertainties

The experimental uncertainty of the axial velocity results measured with the time-of-flight probe has four sources. These consist of: 1) Uncertainties in the measurement of the TOF electrode axial separation, 2) The temporal resolution of the digitizing scope used to record the two TOF signals, 3) Uncertainty due to the method used to interpret the time delay between the TOF signals, and 4) Errors in axial velocity results due to estimates of the plasma flow divergence angle for off-axis measurements. Since interpretation of the TOF signal *magnitudes* is not a prerequisite for determining the convective time delay, there are no uncertainties associated with either the method of measuring the collected current or theories

governing the charged particle collection. The magnitude of each of the uncertainties listed above is summarized individually below:

1) The 5 mm spatial separation of the time-of-flight electrodes was repeatably measured with calipers to be 5.0 ± 0.1 mm, giving an uncertainty in this measurement of ± 2%. Since the TOF velocity measurement (=distance/time) is linear with this distance, the corresponding uncertainty in the velocity results is ± 2%.

2) The time-of-flight electrode signals were sampled at 250 MHz. Exactly one-half of these data were written to computer disk, with every other point in the original time series being saved. This results in an effective sampling rate of 125 MHz, which corresponds to a period of 8×10^{-9} seconds. Based on the expected convective time delay, which is on the order of 1×10^{-6} seconds, this results in an additional 1% uncertainty due to the scope resolution.

3) The methods used to discern the convective time delay between the two time-of-flight signals is estimated to be accurate to within ± 10 sampling intervals, or ~0.08 μs. Based on the measured time delays on the order of 1 μs, this leads to an ~ 8% uncertainty due to the method used to extract the convective time delay from the two TOF electrode signals.

4) Because the plasma streamlines are not known *a priori,* there is an additional uncertainty associated with misalignment between the TOF probe axis and the flow divergence angle. This uncertainty relates only to the off-centerline measurement locations, as the flow divergence on the thruster centerline is likely very near 0° due to the symmetry of the arcjet, and therefore known. An upper limit can be placed on the magnitude of the associated error by considering realistic limits of the misalignment for each

radial measurement location for which $r \neq 0$. For locations near the thruster axis where the flow divergence is expected to be slight, the uncertainty is small as well, since the error ~ cos γ, where γ is the difference between the assumed flow divergence and the actual direction of the flow. For a TOF probe perfectly aligned with the flow, $\gamma = 0°$ and cos $\gamma = 1$. For locations far from the centerline (i.e., r = 3 and 4 mm), the uncertainty in the flow divergence angle is much larger, due simply to the much larger margin of error in this region. Since the axial component of the measured velocity is largely determined by the assumed probe angle for large r, uncertainty in the axial velocity is much larger here as well. Additionally, for probe misalignments greater than ~10°, the width of the probe "seen" by the plasma becomes a significant percentage of the thruster diameter and the spatial resolution of the probe is compromised. Based on these arguments, the additional uncertainties in the axial velocity measurements due to TOF probe misalignment are 0%, 2%, 5%, 15%, and 30% for measurements made at radial locations of 0, 1, 2, 3, and 4 mm, respectively (the nozzle edge is at r = 4.76 mm). The very large uncertainty at r=4 mm reflects the fact that, especially at that location, little information is known about the plasma flow direction.

For the uncertainties discussed above, the root mean square uncertainties in the axial velocity measurements become ± 8.3%, ± 8.5%, ± 9.7%, ± 17.1%, and ± 31.1% for measurements made at r=0, 1, 2, 3, and 4 mm, respectively.

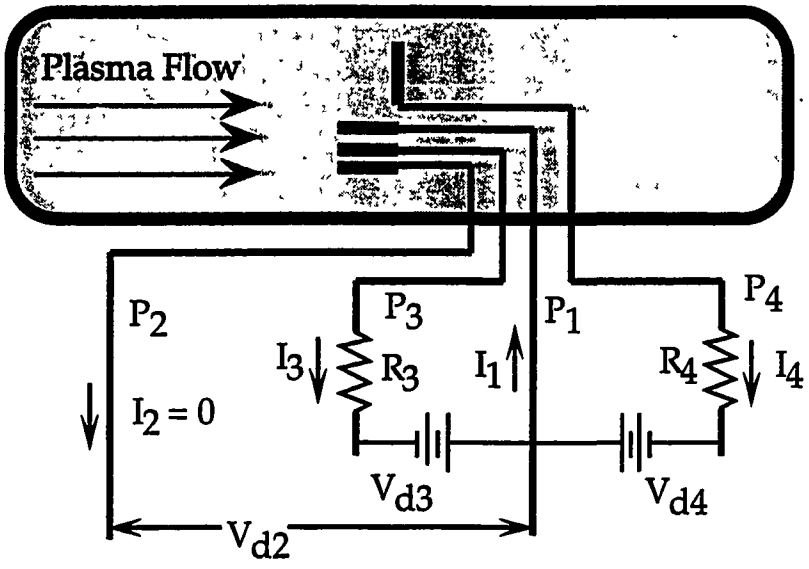

Fig. 4.1 Quadruple probe electrical schematic. The quantities V_{d2}, I_3, and I_4 are measured. The potential difference $V_{d3}=V_{d4}$ is established with 12 V batteries.

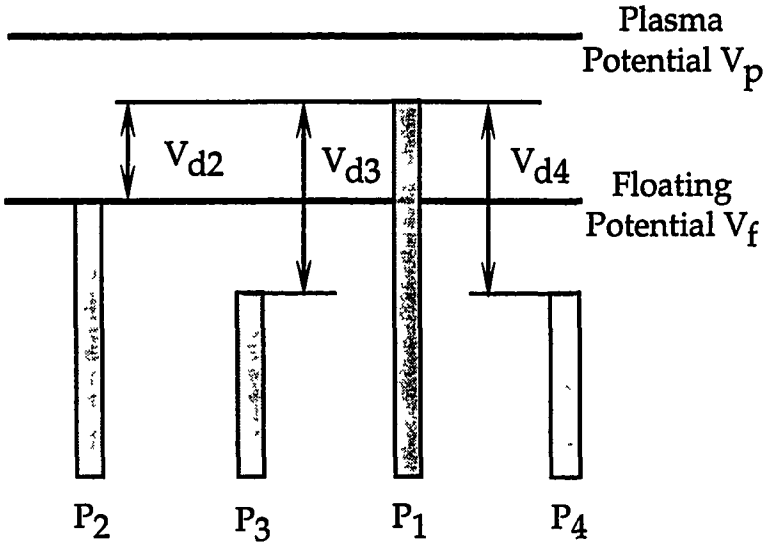

Fig. 4.2 Quadruple probe electrode potential plot for the quadruple probe used in this study with $V_{d3}=V_{d4}$. The probe potentials and the floating potential V_f are less that the plasma potential V_p.

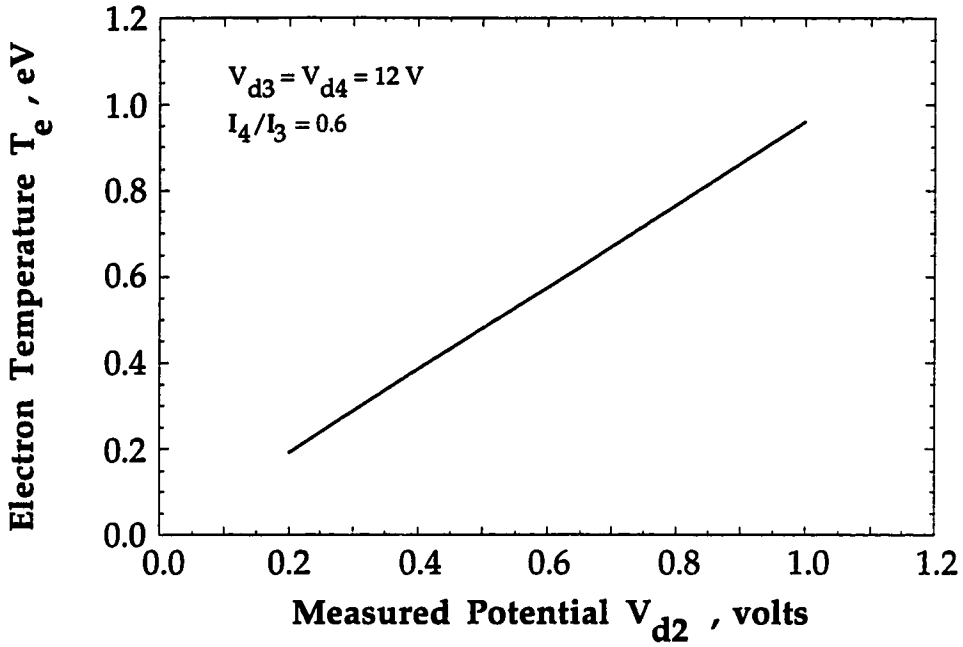

Fig. 4.3 Response of the quadruple probe for electron temperature T_e in terms of the measured quantity V_{d2}. The case of I_4/I_3=0.6 is shown to demonstrate the shape of the probe response.

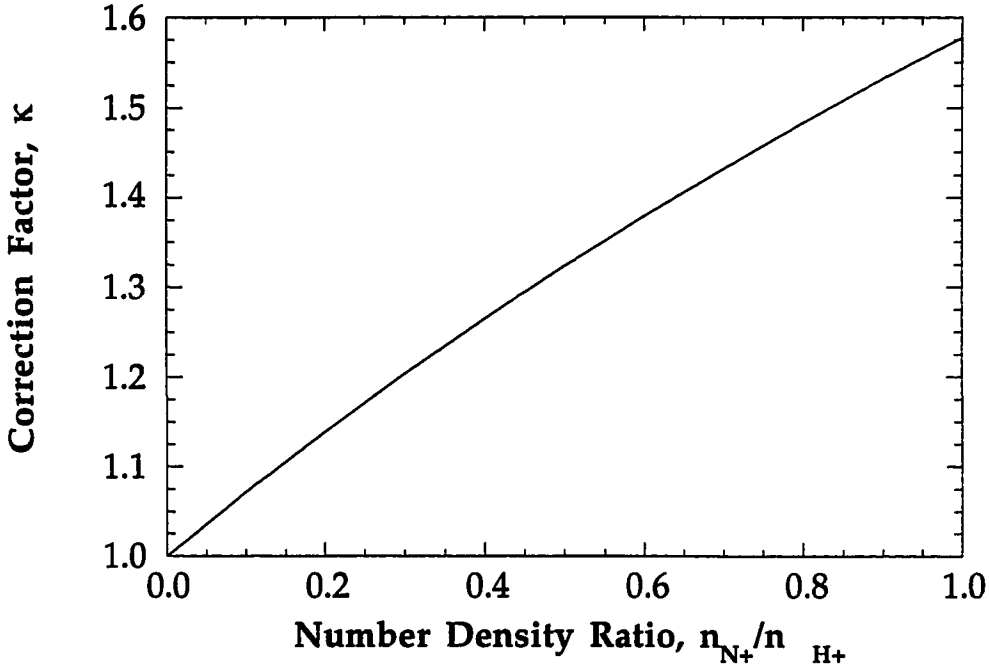

Fig. 4.4 Correction to the quadruple probe n_e measurement to account for the presence of N^+ ions in the seven species H_2-N_2 arcjet plasma.

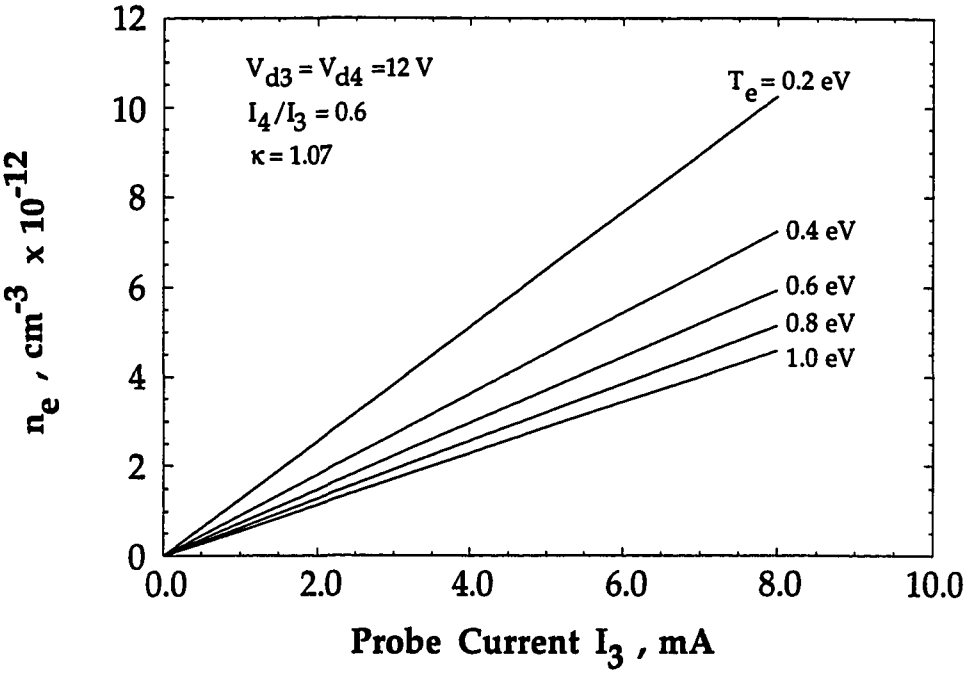

Fig. 4.5 Response of the quadruple probe for electron density n_e in terms of the measured quantity I_3 and the electron temperature determined from Eq. 4.14. The case I_4/I_3=0.6 is shown.

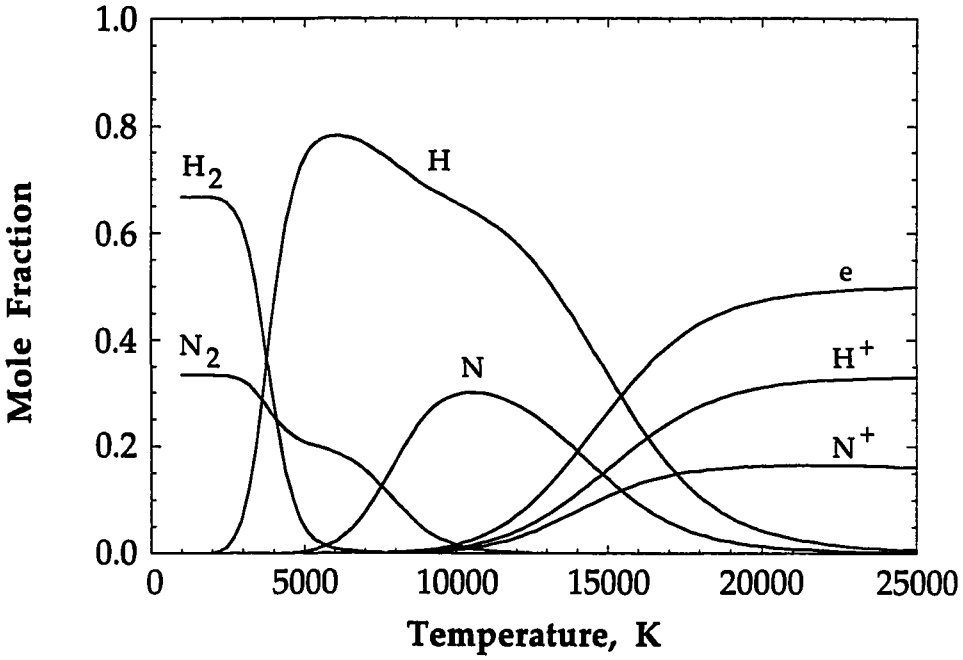

Fig. 4.6 Species mole fractions for $2H_2+N_2$ at p=1 atm under equilibrium conditions (Nachtreib, 1993).

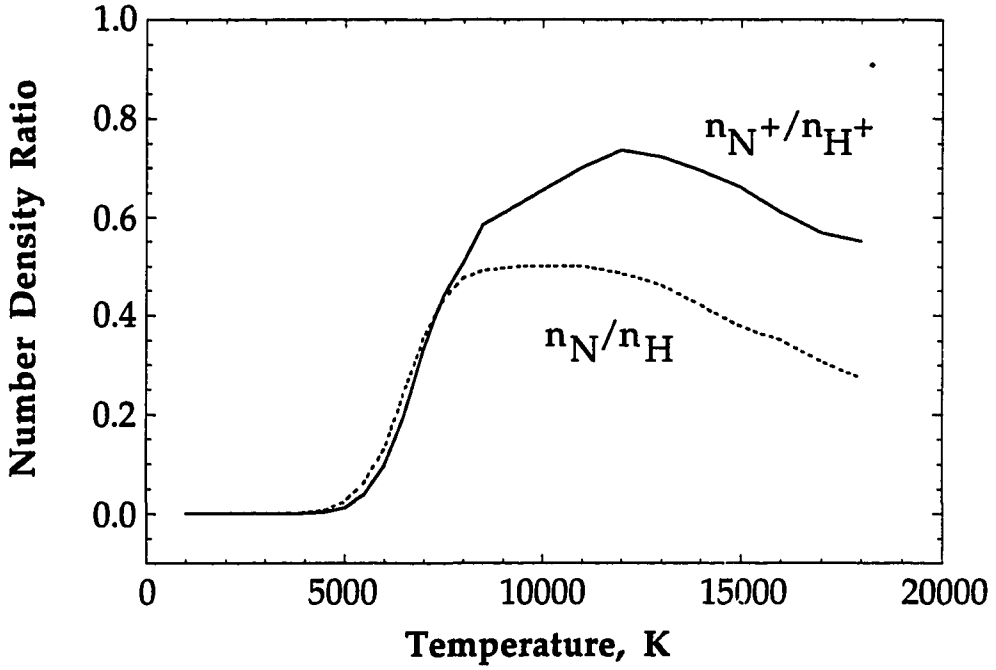

Fig. 4.7 Ionic and atomic number density ratios for hydrazine (N_2H_4) at p=1 atm under equilibrium conditions (Nachtreib, 1993).

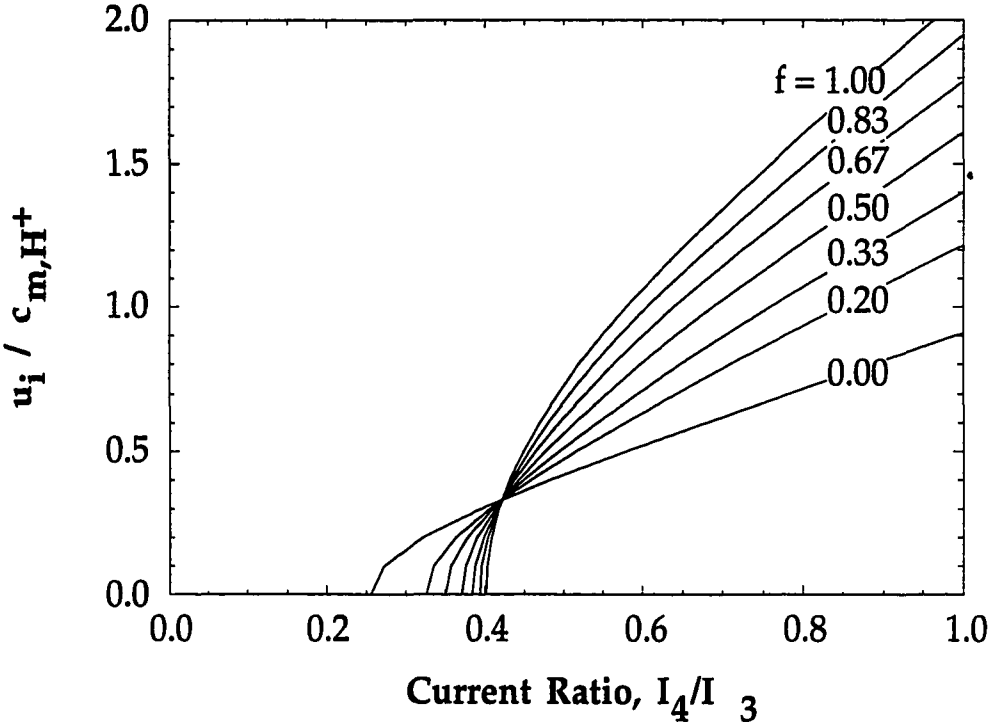

Fig. 4.8 Ion speed ratio $u_i/c_{m,H^+}$ versus I_4/I_3 for 0.0<f<1.0. For this study, f (=n_{H^+}/n_e) is approximately 0.9, corresponding to κ=1.07.

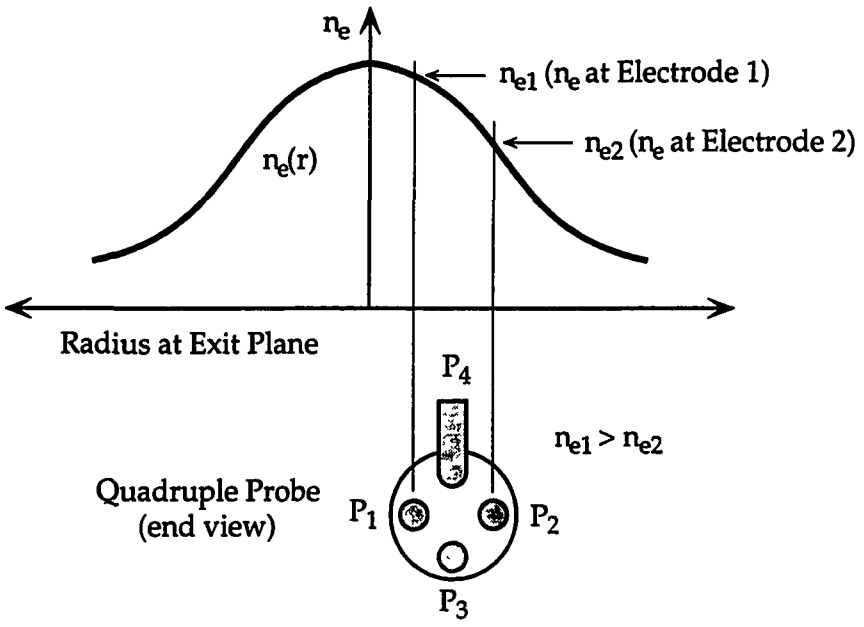

Fig. 4.9 Demonstration of the effect of the probe width on quadruple probe measurements. The difference in the local electron densities at electrodes 1 and 2 results in an asymmetry in the measured quantity V_{d2}.

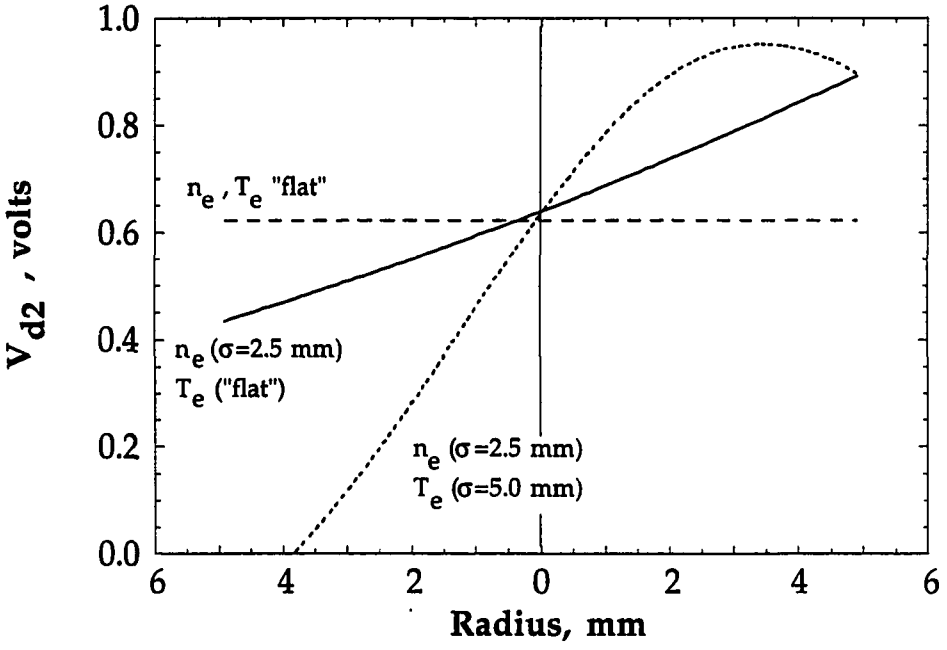

Fig. 4.10 Calculated quadruple probe response to axisymmetric Gaussian profiles of T_e and n_e with standard deviation σ (mm).

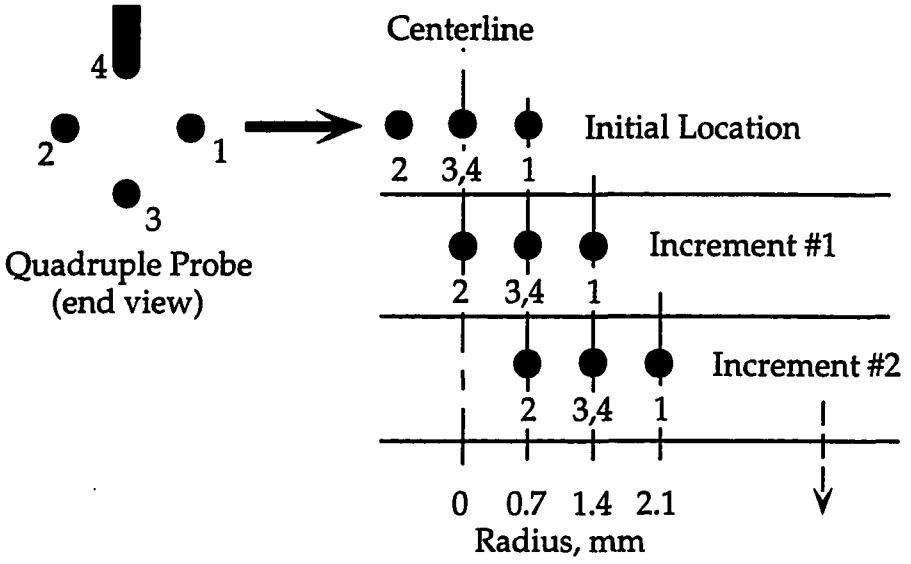

Fig. 4.11 Illustration of the numerical "marching procedure" used to extract radial profiles of T_e and n_e from the quadruple probe data.

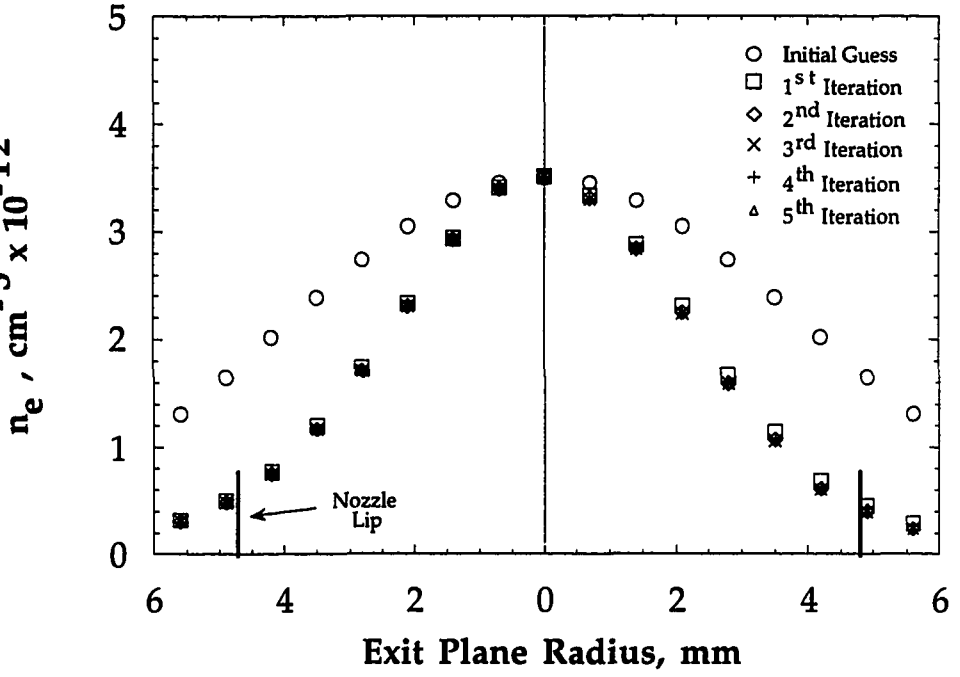

Fig. 4.12 Electron density versus radius showing convergence of the profile during the iterative process of extracting T_e and n_e radial profiles from the quadruple probe data.

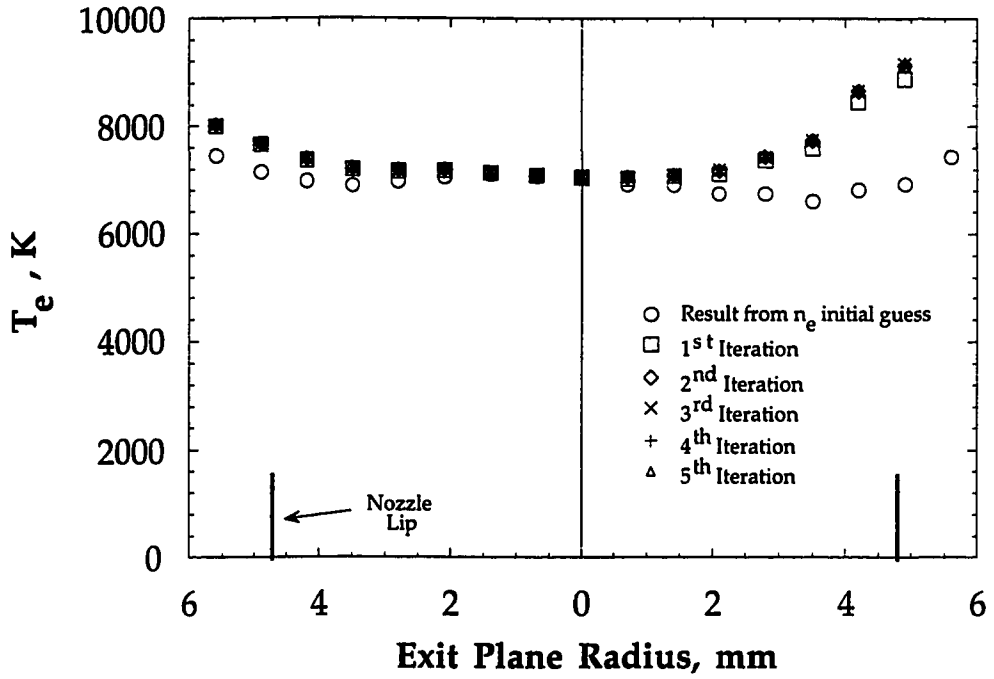

Fig. 4.13 Electron temperature versus radius showing convergence of the profile during the iterative process of extracting T_e and n_e radial profiles from the quadruple probe data.

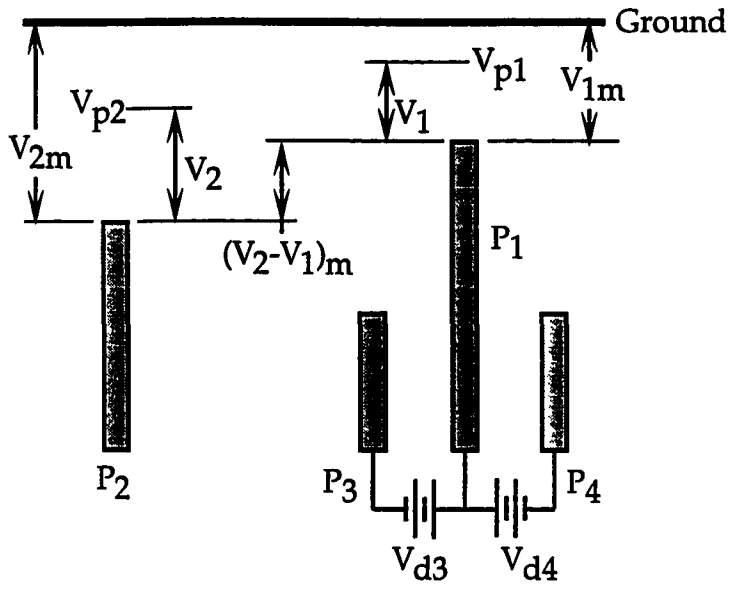

Fig. 4.14 Potential plot for the quadruple probe in a radial electric field, where $V_{p1} \neq V_{p2}$.

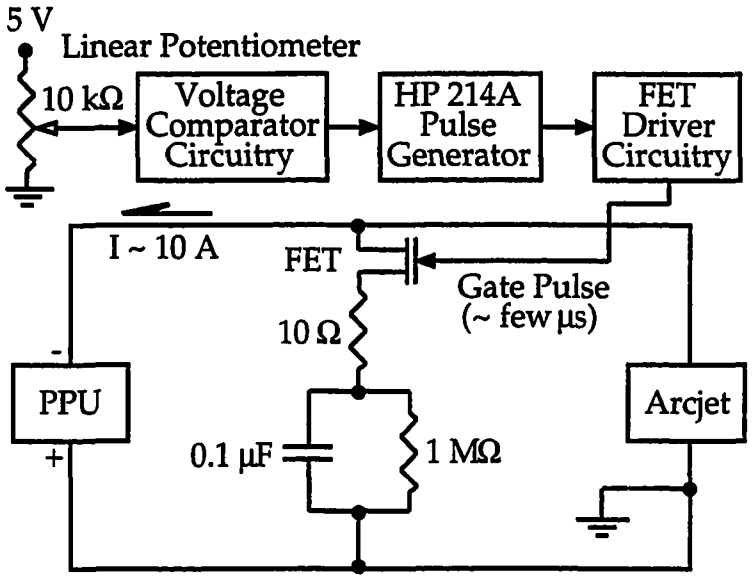

Fig. 4.15 Schematic of the electrical circuit used to generate the arcjet current deficit pulse for the time-of-flight velocimetry technique.

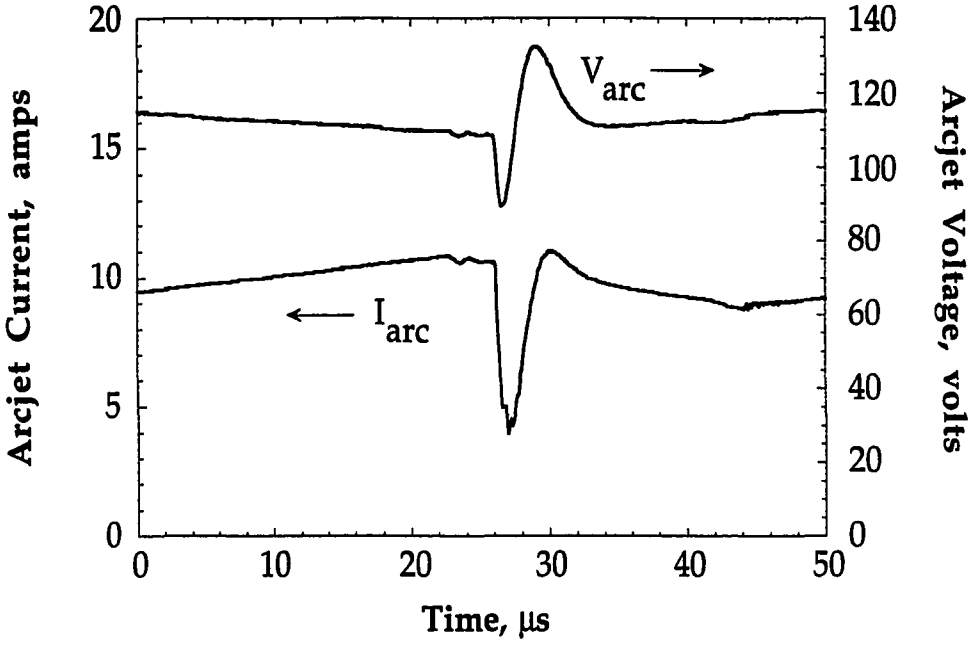

Fig. 4.16 Variation of the arcjet current I_{arc} and voltage V_{arc} during the current deficit pulse. Note that the pulse width (~4μs) is much smaller than the 60 μs period of the PPU ripple.

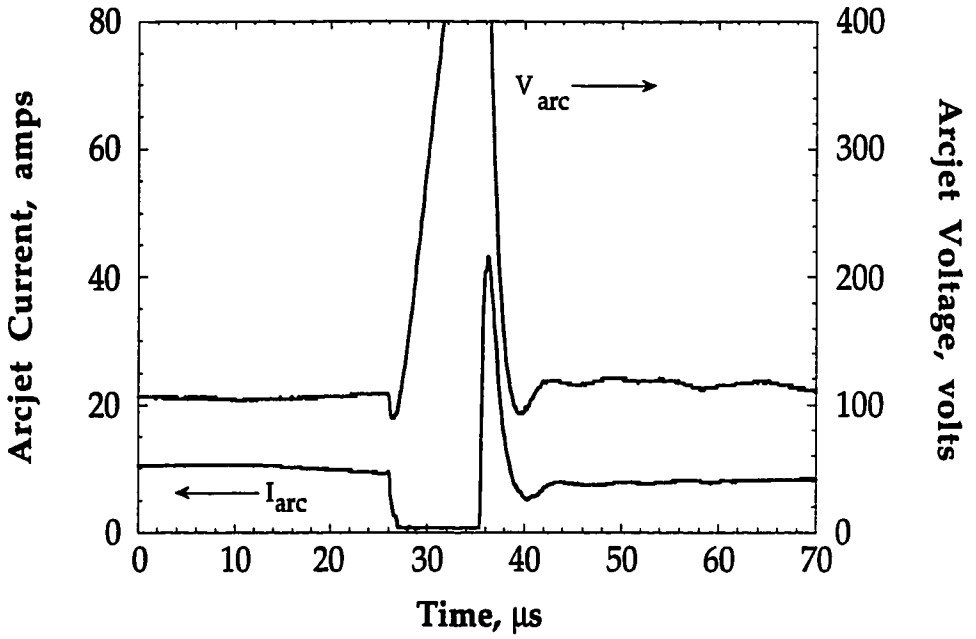

Fig. 4.17 Arcjet current and voltage during a current deficit pulse that was triggered at a minimum point in the PPU current ripple phase. The arcjet plasma is momentarily extinguished during this pulse.

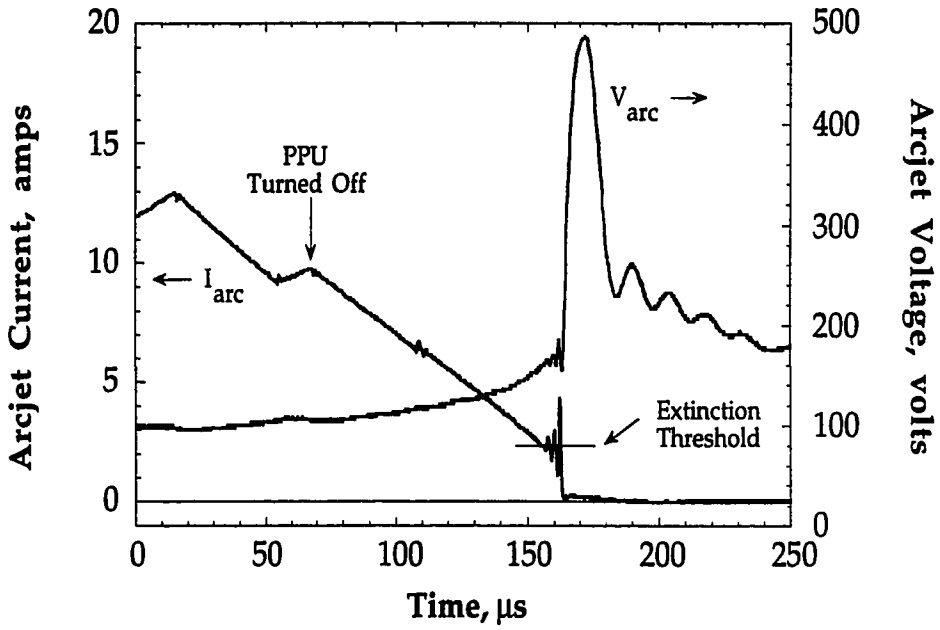

Fig. 4.18 Arcjet current and voltage during the arcjet turn off process, in which the plasma is intentionally extinguished. The thruster power supply was turned off at t~70 μs.

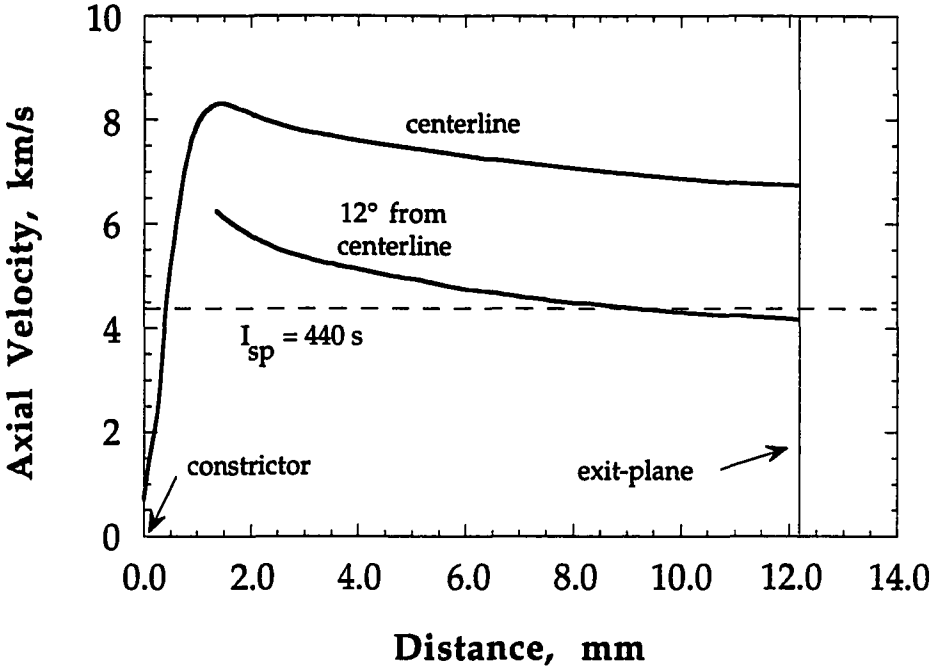

Fig. 4.19 Nozzle interior axial velocities predicted by Megli (1995) for chemical nonequilibrium versus distance from the cathode tip. These results are for I_{arc}=10 amps and 50 mg/s of $2H_2+N_2$.

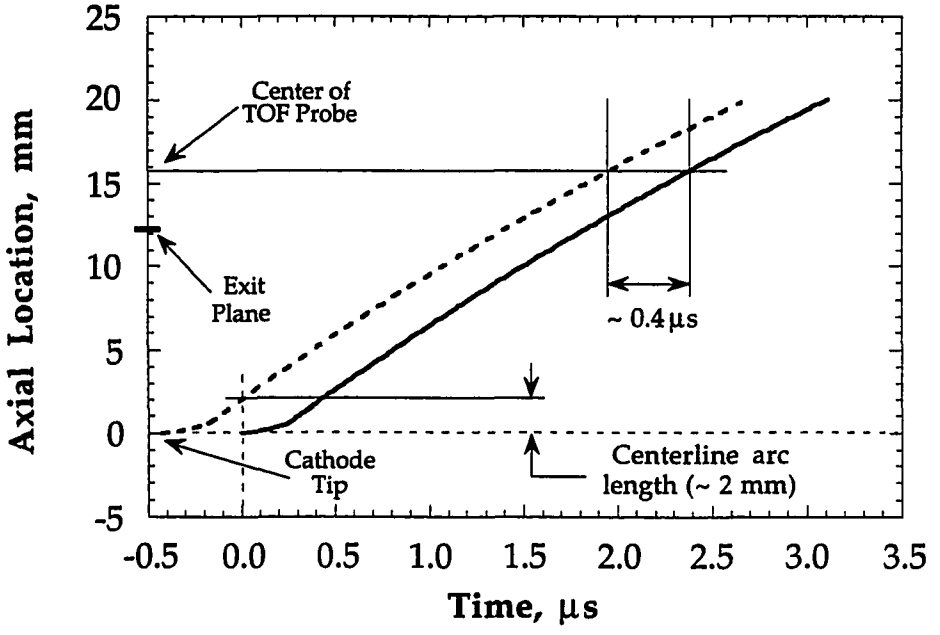

Fig. 4.20 Position versus time (x-t) diagram demonstrating that an infinitesimally narrow (in time) current pulse broadens only ~0.4 μs before it reaches the time-of-flight probe location.

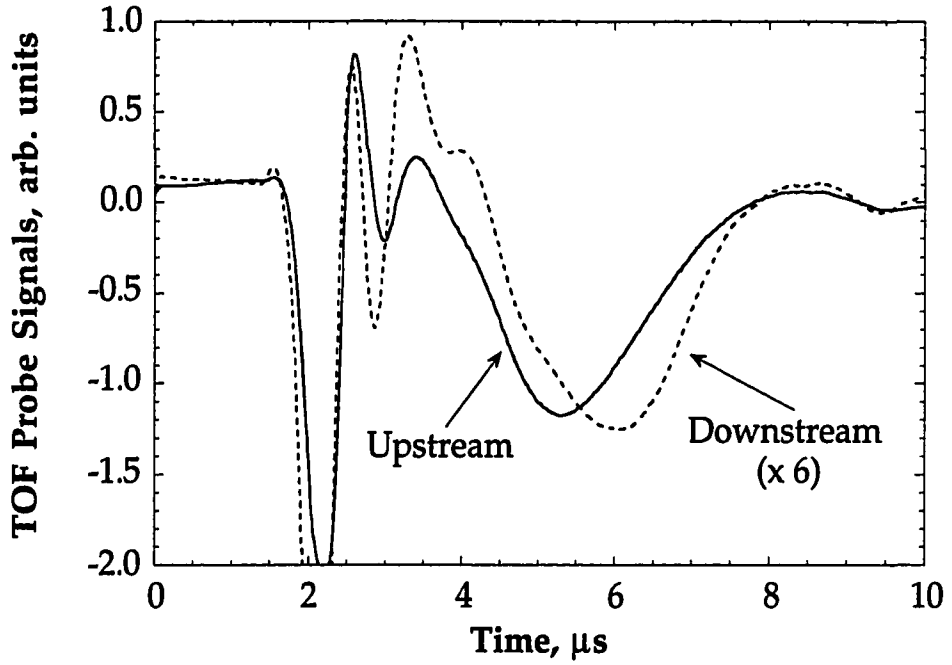

Fig. 4.21 Variation of the time-of-flight probe signals during the arcjet current deficit pulse. The time delay for the effect of the pulse to travel between the two electrodes is ~0.75 μs.

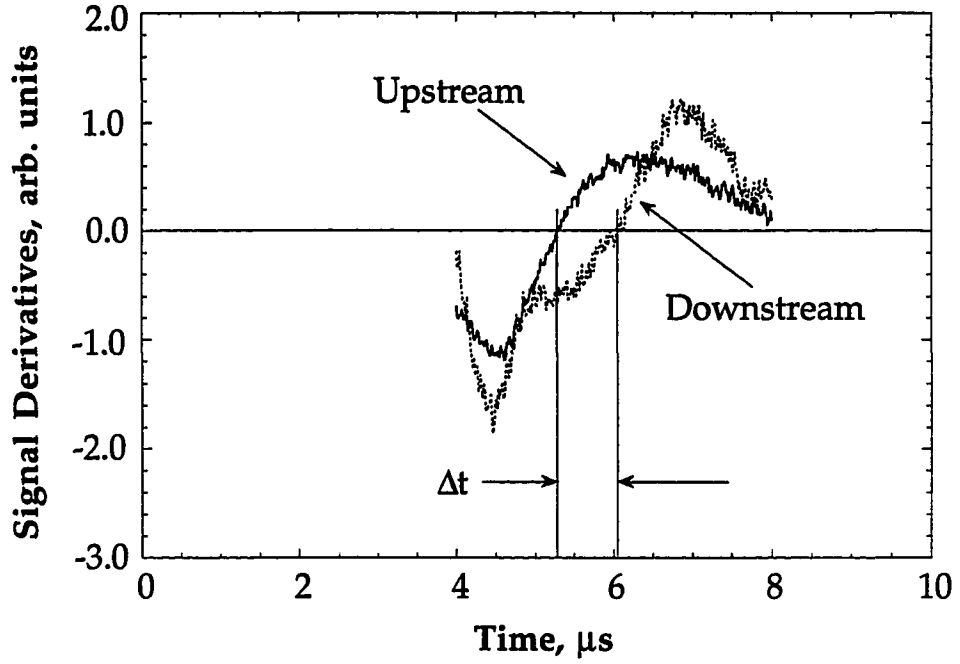

Fig. 4.22 Derivatives of typical smoothed time-of-flight signals depicting zero-crossings at signal minima locations.

5. Experimental Results

5.1 Experimental Operating Conditions

In this study, an investigation of the arcjet very near-field plume region (x=2.2-6.2 mm) was undertaken with a variety of electrostatic probing techniques over a range of thruster operating conditions. A primary goal of this study was to examine arcjet performance as a function of thruster specific power ($P/\dot{m}$). Specific power was varied by changing the arcjet propellant flow rate, by changing the arcjet power (via the current I_{arc}), or by changing both power and flow rate. The thruster conditions studied here are summarized below in Table 5.1. The arcjet operating voltage V_{arc} was observed to decrease uniformly over the three operating conditions 1-3. From condition 1 to condition 2, only the propellant mass flow rate was varied. The operating voltage decreased in this case because the lower flow rate effected a shorter arc length in the nozzle and thus a lower plasma impedance for the same current. Between cases 2 and 3, the voltage also decreases due to a decrease in $\dot{m}$. However, the voltage decreases further with the increase in I_{arc}, due to the negative impedance characteristic of the arcjet. Despite the variation in the thruster flow rate, current, and voltage, the overall power input P remained fairly uniform, as the power for the three conditions varied by less than ~ 6%. However, the specific power ranged from 19.8 to 26.0, corresponding to a ~ 30% change in $P/\dot{m}$ from case 1 to case 3. From case 1 to 2, $P/\dot{m}$ increased ~ 13%, while an additional increase of ~ 16% was noted between cases 2 and 3. As expected, increases in specific power corresponded to increases in the arcjet nozzle (anode) operating temperature T_a as shown in Table 5.1 and Fig. 5.1. From case 1 to case 2, T_a increases ~ 5%,

while the increase is ~ 8% for the change from case 2 to case 3. For the range of thruster specific power investigated, the steady state anode temperature T_a scales approximately linearly with $P/\dot{m}$, as shown in Fig. 5.1.

Operating Condition	$\dot{m}$ (mg/s)	I_{arc} (amps)	V_{arc} (volts)	Power (Watts)	$P/\dot{m}$ (MJ/kg)	T_a (K)
1	60.0	10.0	118.8	1188	19.8	1160
2	50.0	10.0	112.0	1120	22.4	1220
3	45.0	11.0	106.5	1171	26.0	1320

Table 5.1 Summary of the arcjet operating conditions investigated in this study. The quantities I_{arc} and $\dot{m}$ are specified and the remaining parameters are measured or calculated.

Experimental results are presented below in two parts. In the first part (section 5.2), axial velocity results are presented for electrostatic time-of-flight measurements. Radial profiles of the plasma radial velocity are presented for the three arcjet operating conditions discussed above in Table 5.1. Additionally, the effect of thruster warm-up on the centerline axial velocity is documented for the $P/\dot{m} = 22.4$ MJ/kg case.

In section 5.3, the results of plume surveys made with several different electrostatic probes are presented. The $P/\dot{m}$ = 22.4 MJ/kg case was used exclusively during the development of several of the techniques used in this study. As such, several results in addition to the those reflecting the effect of $P/\dot{m}$ on the quadruple probe response were acquired. Namely, the following results are presented for this operating condition: 1) the effect of the PPU ripple on centerline quadruple probe measurements, 2) axial centerline profiles of T_e and n_e for x=2.2-6.2 mm from the thruster exit, 3) single and

triple electrostatic probe verification of quadruple probe measurements, and 4) floating probe estimates of the radial electric field over the thruster exit plane. Additionally, quadruple probe results (T_e, n_e, $u_i/c_{m,H+}$) and estimates of the bulk plasma temperature T_g are presented for the three values of $P/\dot{m}$ discussed above.

5.2 Time-of-Flight Velocimetry Results

Plasma axial velocity results obtained using the electrostatic time-of-flight (TOF) probe discussed in section 4.2 are presented below. Results are presented for centerline velocities obtained during the thruster warm-up process and for radial profiles of the axial velocity measured for each of three different thruster specific powers.

5.2.1 Centerline Axial Velocity During Thruster Warm-up

In order to determine the amount of time required for the thruster velocities to reach steady state conditions, the centerline axial velocity was measured with the TOF probe during the thruster warm-up process. The tip of the upstream electrode was located 1 mm from the thruster exit during these experiments. This corresponds to x= 3.5 mm for the TOF probe center. For $P/\dot{m}$ = 22.4 MJ/kg, the centerline velocity was monitored for up to 14 minutes after three independent arcjet "cold starts." These three experiments were conducted on three different days so that the thruster body was at room temperature at ignition for all three of the experiments.

Results of time-of-flight probe centerline velocity measurements are shown in Fig. 5.2 for data acquired during three individual periods after thruster ignition. These data show that the centerline axial velocity initially averages ~ 6.0 km/s during the period that the thruster is warming up. After

approximately 5-7 minutes of run time, the axial velocity averages ~ 6.5 km/s. These data are consistent with our previous results for this operating condition which indicate that exit plane n_e measurements reach steady state after ~ 4-8 minutes (Burton, et al. 1994). Similarly, it has been shown that the thruster voltage reaches 98% of its steady state value after only ~ 5 minutes of thruster operation (Curran and Haag, 1992). As a result of this experiment, all of the steady state velocity data presented in this study were recorded after at least 8 minutes of arcjet operation.

During the warm-up period, the measured velocities fluctuate between 5.8 and 6.3 km/s. Similarly, the steady-state centerline axial velocities range from 6.3 to 6.7 km/s. These variations, although within the experimental error for this technique, may be due to physical fluctuations in the thruster velocity. Previous work utilizing Current Modulation Velocimetry for a 1 kW hydrogen arcjet performed by Pobst, et al. (1993, 1994) has shown similar velocity fluctuations. In that work, it was determined that the phase of the PPU ripple was not responsible for the apparent fluctuations in the steady state thruster velocities. Similarly, the arcjet current deficit pulse was always triggered at the same phase in the PPU current ripple (see Fig. 4.16) for the data presented in this study. Pobst, et al., whose experimental uncertainties were smaller than the observed fluctuations, were unable to determine a cause for the transient velocity behavior. Because the fluctuations observed in this study are within the experimental uncertainty (± 8.3% on centerline), it cannot be determined whether or not a phenomenon similar to that seen by Pobst, et al. is present in the 1-kW simulated hydrazine arcjet used in this study.

5.2.2 Radial Profiles of Axial Velocity

The time-of-flight probe was also used for off-centerline plasma velocity measurements to generate axial velocity profiles at the thruster exit. For these data, an attempt was made to align the probe with the flow divergence angle δ. It was found that using a fixed angle TOF probe aligned with the thruster axis (θ=0°) produced a flat or even inverted profile with a minima on the centerline. This occurs because an off axis TOF probe that is grossly misaligned with the flow divergence angle ($\theta << \delta$) will see a "faster" plasma at the downstream electrode than at the upstream electrode. Additionally, the electrode separation along the plasma streamline is less than the geometric separation (5.0 mm) by the factor $\cos|\delta-\theta|$. Both of these factors artificially increase the measured axial velocities, with the former phenomenon having a greater effect than the latter. Although the plasma streamlines are not known *a priori*, the error associated with TOF probe misalignment for off axis velocity measurements can be minimized by rotating the probe to align it with the expected flow divergence at a given location. The flow divergence has been shown to be quite large at ~ 10 mm from the thruster exit by Sankovic (1990). Due to the sudden expansion of the flow immediately downstream of the arcjet exit, the flow divergence angle is also likely quite large in the axial region (1<x<5 mm) spanned by the TOF probe. Due to this expansion, flow angles larger than those dictated by the nozzle geometry (half angle = 20°) are also expected at the exit. For time-of-flight measurements at r = ±0, ±1, ±2, ±3 and ±4 mm, the probe angles used were ±0°, ±10.8°, ±18.0°, ±25.2° and ±45.0°, respectively. It was assumed that velocities measured in this manner were along the probe axis and were converted to axial components. Clearly, these estimates of the plasma flow

divergence angles represent a significant portion of the experimental uncertainty in the measured axial velocities for off-centerline measurements. For centerline measurements, however, this source of uncertainty is not present due to the azimuthal symmetry of the arcjet.

Figure 5.3 shows the results of a typical radial profile of the plasma axial velocity measured at the thruster exit plane, using the technique discussed above. The upstream time-of-flight electrode is located 1.0 mm from the thruster exit plane, and the arcjet is operating at the $P/\dot{m}$ = 22.4 MJ/kg condition. The error bars represent the experimental uncertainties discussed in section 4.3.6, with the percentage error increasing with distance from the centerline. The profile appears fairly symmetric, with the axial velocity decreasing greatly at the edge of the thruster exit plane, which is denoted by the two black lines at ± 4.76 mm in Fig. 5.3.

5.2.3 Effect of $P/\dot{m}$ on Axial Velocity Radial Profiles

For the thruster operating conditions investigated in this study, radial profiles of the axial plasma velocity were measured using the methodology discussed in section 5.2.2. Radial profiles are shown in Fig. 5.4 for $P/\dot{m}$ =19.8, 22.4, and 26.0 MJ/kg. For all three profile measurements, the probe tip was located 1 mm from the exit plane and the probe angles were as specified in section 5.2.2. The peak of the measured radial profiles increases with thruster specific input power. Although experimental uncertainties are larger near the edge of the thruster exit, the profiles appear to become slightly more narrow and peaked at the center as $P/\dot{m}$ increases.

Experimental uncertainty in the axial velocity, despite being large for the off-centerline values, is moderate for measurements on the centerline

because there are no errors there due to estimating the flow divergence angle. For this reason, centerline values are used to compare with numerical model results in section 6.2. Additionally, the reported centerline values for all three of the conditions investigated represent the average of several independent TOF surveys at that location. Figure 5.5 shows the centerline axial plasma velocity versus the thruster specific power. The solid line in the figure represents a best-fit straight line through the data, indicating that the axial velocity at the centerline is linear with $P/\dot{m}$ for the conditions examined in this study.

5.3 Electrostatic Probe Results

This section describes the results of electrostatic probe measurements made with the quadruple probe shown in Fig. 2.4. Quadruple probe measurements yield T_e, n_e, $u_i/c_{m,H^+}$ and, when coupled with TOF probe data, estimates of the gas temperature T_g. Independent measurements of T_e and n_e made with single and triple electrostatic probes validate the quadruple probe measurements. The effect of the arcjet PPU ripple on the quadruple probe response has been determined with quadruple probe measurements on the thruster centerline, Additionally, the effect of axial gradients on plasma parameters over the quadruple probe length is quantified by measuring the centerline axial profiles of T_e and n_e. Finally, the radial electric field at the thruster exit plane has been estimated using two of the quadruple probe electrodes in a double floating probe configuration.

5.3.1 Effect of the PPU Ripple on Probe Measurements

For the quadruple probe, T_e, n_e, and $u_i/c_{m,H^+}$ are determined by measurements of the probe voltage V_{d2} and ion currents I_3 and I_4. Since

these parameters are expected to be influenced by the inherent current ripple (± 8%) associated with the arcjet PPU, a discussion of the effect of this ripple on the probe is warranted. Figure 5.6 shows the centerline ion current density j_3 (= I_3/A_3) measured by electrode 3 and the arc current I_{arc} versus time. These data were acquired for $P/\dot{m}$ = 22.4 MJ/kg while the probe tip was located 1 mm downstream of the exit plane. Since I_{arc} is in essence the current at the arcjet cathode tip, the effect of the PPU ripple on the probe current I_3 is expected to be delayed as the plasma is convected over the ~ 15 mm distance between the cathode tip and the probe. In fact, the current measured at electrode 3 is in phase with the arc current, except for a delay of ~ 3-4 μs associated with the time required for the plasma to flow from the arc-heating region near the cathode to the quadruple probe. Accounting for differences in measurement location and the average velocity based on I_{sp} values of hydrogen and hydrazine arcjets, this time delay is consistent with previous triple probe results for the 1-kW hydrogen arcjet (Pobst, et al. 1993).

The relationship between centerline measurements of the quadruple probe quantities V_{d2} and j_3 is shown in Fig. 5.7. While j_3 closely follows the phase of the PPU current ripple except for the 3-4 μs convective delay, V_{d2} is 180° out of phase with j_3. Since the ion saturation current $j_3 \sim n_e(T_e)^{1/2}$ and V_{d2} increases monotonically with T_e as shown in section 4.1, Figs. 5.6 and 5.7 indicate that n_e increases and T_e decreases with increases in I_{arc} during a typical PPU ripple cycle. Specifically, Eqs. (4.14) and (4.20) indicate that the ±8% arcjet current ripple causes an associated ± 18% ripple in n_e (in phase) and a ± 5% ripple in T_e (180° out of phase) about their mean values. For the quadruple probe centered at x=2.2 mm from the exit plane, the mean centerline values are T_e ~0.6 eV and n_e ~3.6 x 10^{12} cm^{-3}. The T_e results,

although out of phase with I_{arc}, are in phase with the arc voltage V_{arc} (which has a ± 3% ripple) due to the negative impedance characteristic of the arcjet, as demonstrated in Fig. 2.2. Thus, the T_e behavior is consistent with the variation of the electric field between the arcjet anode and cathode, which heats the electrons. Additionally, increases in n_e with increasing arcjet current are consistent with increases in the ionization fraction of the plasma as the number of energetic electrons available for dissociating and ionizing collisions increases with I_{arc}.

Because of the large variation in the measured quantities V_{d2}, I_3 and I_4 with the PPU current, the mean values of these parameters are used to determine the mean values of T_e, n_e and $u_i/c_{m,H^+}$ through Eqs. (4.14), (4.20) and (4.24). For all subsequent electrostatic probe data presented in this study, a moving average smoothing routine is applied to the raw data so that the effects of the PPU ripple are eliminated. Care is taken so that the smoothed profiles accurately represented the true mean of the PPU ripple effects.

5.3.2 Axial T_e and n_e Profiles

Previous n_e data measured with single Langmuir probes (Sankovic, 1990) and by Zube and Myers (1993) and Manzella, et al. (1990) via emission spectroscopy indicate that axial gradients over the length of the quadruple probe may be significant. To quantify the effects of axial gradients in T_e and n_e over the 2.5 mm quadruple probe length for the 1-kW hydrazine thruster used in this study, centerline data were acquired for several probe axial locations for the arcjet operating at $P/\dot{m}$ = 22.4 MJ/kg. Five probe tip locations from x=1 to 5 mm from the thruster exit, in 1 mm increments, were examined. Results for the measured ion saturation current density j_3 for the

five centerline axial locations are shown in Fig. 5.8. The horizontal error bars represent the 2.5 mm length of electrode 3 and indicate the extent to which quadruple probe data represent averages of the measured plasma parameters over the probe length in the axial direction. A 50% decrease in j_3 is indicated over the 4 mm region investigated, which represents the combined effect of changes in T_e and n_e, since the ion saturation current density $j_3 = I_3/A_3 \sim n_e(T_e)^{1/2}$.

Figure 5.8, along with the corresponding V_{d2} data and Eqs. (4.14) and (4.20), yields the axial centerline profiles of T_e and n_e shown in Figs. 5.9 and 5.10. The electron temperature (Fig. 5.9) varies from 6700 to 3600 K (~0.6 - 0.3 eV) for quadruple probe measurements made with the probe length centered between $2.2 < x < 6.2$ mm from the thruster exit.

Results for the electron density axial profile measured by the quadruple probe are shown in Fig. 5.10. A line denoting a spherical expansion of the electrons, with a virtual center at the arcjet constrictor, is also shown. Over the 4 mm range of probe locations n_e drops by ~ 30%, with the magnitude of dn_e/dx increasing slightly near the thruster exit. While the n_e gradient based on the present data is significant near the nozzle exit ($dn_e/dx \sim -0.5 \times 10^{12}$ cm^{-3}/mm at x= 2-3 mm), it is not large enough to prevent the use of the 2.5 mm long quadruple probe in that region.

Based on the axial variations of T_e and n_e reported above, it is apparent that the quadruple probe results represent plasma conditions averaged over the axial dimension (2.5 mm) of the probe. The uncertainty introduced to these measurements by the axial gradients is not large enough to offset the utility of the quadruple probe in this type of plasma environment.

With the measurements of centerline plasma conditions presented above, one is now in a position to calculate the plasma ionization fraction and relevant length scales and at the thruster exit (x=2.2 mm). From the numerical model results of Megli (1995) for condition 2 (see Table 6.3), the neutral particle density at the thruster exit plane is ~ 1×10^{16} cm^{-3}. The model results, coupled with the centerline measurement of $n_e \sim 4 \times 10^{12}$ cm^{-3}, reveal that the arcjet exit plane plasma is very weakly ionized, with an ionization fraction $\alpha \approx 10^{-4}$. Additionally, the Debye length for the conditions at x = 2.2 mm of $T_e \sim 0.6$ eV and $n_e \sim 4 \times 10^{12}$ cm^{-3} is $\lambda_D \sim 3 \times 10^{-3}$ mm, which is much smaller than the probe electrode diameter of 0.25 mm.

As discussed in section 3.5, the plasma at the x = 2.2 mm measurement location is in the free molecular flow regime as demonstrated by the following ratios of mean-free-path to electrode radius r_p (= 0.125 mm): $\lambda_{n\text{-}n}/r_p = 20$, $\lambda_{i\text{-}n}/r_p = 5$, $\lambda_{i\text{-}i}/r_p = 30$, $\lambda_{i\text{-}e}/r_p = 20$, $\lambda_{e\text{-}n}/r_p = 20$, and $\lambda_{e\text{-}e}/r_p = 30$. Electron collisions with other species are infrequent in this region, so that information regarding the plasma expansion downstream of the exit plane can be obtained by plotting T_e versus n_e for the axial locations reported in Figs. 5.9 and 5.10. For an adiabatic expansion of the electrons, the electron temperature is expected to vary as $T_e \sim n_e^{\gamma-1}$, with $\gamma = 5/3$. Based on the results discussed in section 5.3.7 indicating that a small amount of ohmic heating is present at the thruster exit plane, the electron temperature is expected to decrease *less rapidly* than $T_e \sim n_e^{\gamma-1}$. However, calculations show that T_e and n_e (Figs. 5.9 and 5.10) very roughly follow an adiabatic and spherical expansion, with T_e decreasing *more rapidly* than one would expect for a purely adiabatic expansion, despite the presence of ohmic heating at the thruster exit. This phenomenon clearly requires further experimental investigation.

5.3.3 Single and Triple Electrostatic Probe Measurements

As an independent check of the quadruple probe and to insure that the presence of the perpendicular electrode in the electrical circuit (see Figs. 2.4 and 4.1) does not influence the T_e and n_e data, independent measurements were made with a single and triple electrostatic probes at the first axial location (x= 2.2 mm) for $P/\dot{m}$ = 22.4 MJ/kg. The single probe, in addition to providing independent measurements of T_e and n_e, was used to investigate the physical symmetry of the plume.

The triple probe consisted of the three aligned electrodes (1-3) of the quadruple probe. As such, the triple and quadruple probes were identical except that the perpendicular electrode was disconnected from the probe circuit (Fig. 4.1) while the probe was in the triple probe configuration. The quadruple and triple probe T_e and n_e data were consistent within 5%, which is well within the experimental uncertainties associated with the experiment. This is not a surprising result, since in the limit I_4/I_3 --> 0, Eqs. (4.14) and (4.20) reduce to the triple probe equations for T_e and n_e. However, it does confirm the fact that the use of the perpendicular electrode, and the subsequent introduction of the measured quantity I_4/I_3 into the T_e and n_e equations, does not adversely influence the quadruple probe response.

Experiments were also performed with a single electrostatic probe at the thruster exit plane (x=2.2 mm) for a simulated hydrazine thruster operating at $P/\dot{m}$ = 22.4 MJ/kg. These single probe experiments serve two purposes: 1) they provide independent measurements of T_e and n_e for comparison with the multiple electrostatic probe data, and 2) they allow a direct measurement of the extent of plume symmetry in the exit plane region. A classical single Langmuir probe, which consisted of electrode 3 of the

quadruple probe, was used to measure the current collected during several radial sweeps across the thruster exit plane. During each single probe radial sweep, the electrode center was located 2.2 mm from the thruster exit and was biased at a constant value ranging from -8.0 V (ion collection) to 6.0 V (electron collection) relative to facility ground. This methodology is contrary to most uses of the single Langmuir probe because the probe bias voltage is not "swept" to generate a voltage-current (V-I) characteristic. The harsh environment of the plasma plume prevented the single probe from being stopped in one place long enough for a V-I characteristic to be measured in this study. The current collected by the probe was determined by measuring the voltage across a current shunt resistor.

The smoothed single probe surveys, demonstrating the symmetric nature of the arcjet near-field plume, are summarized in Fig. 5.11. Because the probe bias potential was dependent on the voltage drop across the current shunt resistor (Fig. 3.1), the bias tended to change slightly as the current collection varied with the probe location in the plume. The probe bias voltages noted in Fig. 5.11 reflect these slight changes and are the bias potentials for the centerline position of the single probe (r=0). For a given radius, these data can be used to construct a Langmuir probe V-I characteristic by plotting the probe current versus the bias voltage. For r=0 mm, this V-I characteristic is shown in Fig. 5.12. Using the Langmuir probe techniques discussed in section 3.1.4 this characteristic yields an electron temperature of $T_e \sim 0.6$ eV. The determination of n_e from the V-I characteristic follows from the value of T_e and Eq. (3.5). For the characteristic shown in Fig. 5.12, the electron density is $\sim 7 \times 10^{12}$ cm^{-3}. The single probe T_e measurement agrees very well with the quadruple probe measurement at x=2.2 mm. The

quadruple probe measurement of n_e is ~ 50% less than the corresponding single probe value of electron density. However, this discrepancy is not altogether surprising considering the generally accepted uncertainties in electrostatic probe n_e measurements of ~ 50-60% (Tilley, et al. 1990). The fact that the triple and quadruple probe n_e results are within 5% is also not surprising, since their corresponding approaches make identical assumptions (e.g., Bohm Sheath) in the derivation of the respective probe responses.

5.3.4 Radial T_e and n_e Profiles

The results of a typical quadruple probe radial sweep through the thruster plume are shown in Fig. 5.13. For this sweep, the probe centers were 2.2 mm downstream of the exit plane, which was operating at $P/\dot{m}$ = 22.4 MJ/kg. Like the single probe data presented above (Fig. 5.11), typical quadruple probe measurements at the thruster exit plane reveal a smooth symmetric profile for the measured electrode current I_3. However, the measured potential difference V_{d2} is not symmetric with radius as a result of the steep radial gradient in n_e off-axis and, to a lesser extent, the radial gradient in T_e as demonstrated in section 4.2.2. These gradients, which are perpendicular to the quadruple probe electrodes and the arcjet thrust axis, cause the local values of T_e and n_e to differ from electrode P_1 to electrode P_2, and thus cause the apparent asymmetry in V_{d2} as the probe electrodes 1 and 2 pass through the plume.

The I_3 and V_{d2} data of the type shown in Fig. 5.13, along with the modified quadruple probe radial gradient theory, are used to solve for the radial profiles $T_e(r)$ and $n_e(r)$ using the iterative scheme discussed in section 4.2.3. The results of this technique for $T_e(r)$ and $n_e(r)$ are shown in Fig. 5.14

for the case of $P/\dot{m}$=22.4 MJ/kg. The resulting T_e profile is very flat for r<3 mm and nearly uniform at the centerline value of T_e = 7000 K. The radial n_e profile is also shown in Fig. 5.14 for this thruster operating condition. Recall that the T_e and n_e radial profiles shown in Fig. 5.14 are extracted simultaneously from the I_3 and V_{d2} quadruple probe data (Fig. 5.13). Far from the centerline, the uncertainty in n_e increases due to misalignment between electrodes 3 and the flow divergence angle δ. Similarly, a recent study has shown that T_e measurements can be artificially increased by electrode misalignment with the flow vector (Tilley, et al. 1994). It was demonstrated that measurements in the plume of an MPD thruster by means of a triple probe yielded T_e values for a 30° misalignment that were ~ 6% higher than measurements made with a properly aligned probe. Radial results presented in this study are limited to regions of the plume on or near the centerline where the misalignment is small, so that variations caused by this effect are manageable.

5.3.5 Ion Speed Ratio Measurements and T_g Estimates

The measured currents I_3 and I_4 and the current ratio I_4/I_3 are plotted in Fig. 5.15 for a typical quadruple probe sweep at x=2.2 mm and $P/\dot{m}$ = 22.4 MJ/kg. The measured current ratio I_4/I_3 range of ~0.60, along with κ=1.07 (f~0.9, see section 4.1.3), yields $u_i/c_{m,H^+} \sim 1.0 \pm 15\%$ by Fig. 4.8. A value of $u_i/c_{m,H^+}$ near unity indicates that the most probable thermal speed for H^+ (c_{m,H^+}) is approximately equal to the directed ion velocity u_i for this thruster operating condition. Recall that the contribution to the current ratio I_4/I_3 from nitrogen ions N^+ has been expressed in terms of H^+, as discussed in Chapter 4. As demonstrated in Fig. 4.8, the value of $u_i/c_{m,H^+}$ is highly

dependent on the plasma composition parameter f, so that the uncertainty in the ion speed ratio is influenced by knowledge of the plasma composition at the exit plane. This point is addressed further in section 4.1.5.

Since measurements of the plasma axial velocity u_i have been made with the TOF probe (section 5.2), quadruple probe data for $u_i/c_{m,H+}$ can be used to estimate the heavy particle kinetic temperature $T_g=T_i$. By the definition of the most probable thermal speed, and assuming that all of the heavy particles have the same kinetic temperature (Liebeskind, 1995), the bulk plasma temperature is given by

$$T_g = T_i = \frac{m_{H^+} (c_{m,H^+})^2}{2} \tag{5.1}$$

The most probable thermal speed of H+ ($c_{m,H+}$) is determined from the quadruple probe measurement of $u_i/c_{m,H+}$ and the measured axial velocity u_i. For the measured centerline velocity u_i=6.5 km/s at $P/\dot{m}$ = 22.4 MJ/kg (Fig. 5.3), the heavy particle temperature from Eq. (5.1) is $T_g=T_i$ ~ 3000 K. The radial profile of T_g for $P/\dot{m}$ = 22.4 MJ/kg, based on measurements of $u_i(r)$ and $u_i/c_{m,H+}$, is shown in Fig. 5.16. The uncertainty in these values of the heavy particle temperature is discussed below.

The uncertainty in the ion most probable thermal speed $c_{m,H+}$ is determined from the uncertainties in measurements of u_i and $u_i/c_{m,H+}$. Since $c_{m,H+} = [1/(u_i/c_{m,H+})]_{meas.} \times (u_i)_{meas.}$, the centerline uncertainties in $u_i/c_{m,H+}$ (± 15%) and u_i (± 10%) correspond to an rms uncertainty in $c_{m,H+}$ of ~ ± 20%. By the definition of $c_{m,H+}$ [Eq. (5.1)] and the dependence of T_g on $(c_{m,H+})^2$, this corresponds to an uncertainty of approximately +45/-35% in the centerline estimates of T_g.

An additional uncertainty in T_g is due to the size of the perpendicular quadruple probe electrode, since this electrode in reality measures the current I_4 based on a distribution of u_i and T_i along its 2 mm length. Because the quadruple probe theory for determining T_e and n_e uses the measured value of I_4/I_3, no error due to the presence of the perpendicular electrode is involved in determining these parameters. This has been verified (see section 5.3.3) with independent triple probe measurements of T_e and n_e. However, in interpreting the crossed probe data, the geometry of the probe becomes a factor. The electrode current I_4 is likely slightly under-represented due to a decrease in ion density and u_i along the electrode length for its off-centerline position. Conversely, because $I_4/I_3 \sim u_i/c_{m,H+}$ is proportional to $1/(T_i)^{1/2}$ (by definition), a T_i profile peaked at the centerline has the opposite effect on the current ratio I_4/I_3, although to a lesser extent because of the square root dependency. The determination of the gas temperature T_g becomes sensitive to the ion current collected at electrode P_4. Assuming a 10% underestimate of I_4 due to spatial extent of the perpendicular electrode, the ratio $u_i/c_{m,H+}$ increases 20%, and T_i becomes ~2000 K . Based on this analysis, the actual value of T_g is 30% less than the value determined via the quadruple and TOF probes. For this reason, and because the T_g estimate is based on other measurements with associated uncertainties of + 45%/- 35%, the overall uncertainty in the determination of T_g is + 5%/- 50%. Clearly, T_g values reported in this work carry a greater-than-desirable level of uncertainty based on experimental results of the crossed probe and time-of-flight probe techniques.

5.3.6 Effect of P/ṁ on Quadruple Probe Measurements

In sections 5.3.1-5.3.5 above, experimental results were shown for case 2 in Table 2.1 (i.e., P/ṁ=22.4 MJ/kg). Quadruple probe measurements were also made at other arcjet operating conditions for the purpose of investigating the effect of changes in the thruster current and propellant flow rate on its performance. These results, corresponding to thruster specific powers of 19.8, 22.4, and 26.0 MJ/kg are discussed below. In this discussion, cases 1, 2, and 3 refer to P/ṁ of 19.8, 22.4, and 26.0, respectively.

Figure 5.17 shows the effect of varying the thruster operating conditions on the centerline n_e at x=2.2 mm. Although the uncertainty in the n_e measurements is ± 50%, this is due primarily to quadruple probe assumptions. As such, the trends measured with the probe, despite being within the experimental uncertainty, are valid. In increasing P/ṁ from 19.8 to 22.4 (i.e., *decreasing* ṁ from 60 to 50 mg/s), the electron density decreases as well. More specifically, a 17% decrease in ṁ caused a 12% decrease in n_e. Decreasing the thruster flow rate also decreases the pressure and density of the gas as it enters the constrictor. The decrease in n_e between cases 1 and 2 is presumably due to a corresponding change in the gas density, which decreases the number of neutral particles available for ionizing collisions with energetic electrons. Additionally, the arcjet power decreased from 1188 W to 1120 W in the transition from case 1 to 2, indicating that 5.7% less power was deposited to the gas in case 2 than in case 1.

In changing the arcjet operation from case 2 to 3, ṁ was decreased 10% *and* I_{arc} was increased 10% according to Table 2.1. This transition corresponds to a ~23% increase in n_e. One would expect that an increase in I_{arc} for a given ṁ would increase the number of free electrons in the plasma since the

number of collisions with arc electrons in the constrictor also would increase. Based on the results for cases 2 and 3, it appears that the electron density in the plume is a stronger function of I_{arc} than $\dot{m}$.

The results of quadruple probe n_e radial profile measurements are shown in Fig. 5.18 for the three thruster specific powers investigated in this study. The electron density profiles were generated using the iterative technique described in section 4.2.3. Results are not shown for r>3.5 mm, since uncertainties due to probe misalignment with the plasma streamlines are difficult to quantify in this region. The centerline values demonstrate the trends shown previously in Fig. 5.17. For all three profiles, the density falls off drastically at the edge of the arcjet exit plane, as expected.

The variation of the centerline values of T_e measured with the quadruple probe is demonstrated in Fig. 5.19. Changing the propellant flow rate (case 1-->2) appears to have little effect on the measured electron temperature at the thruster exit plane. However, decreasing $\dot{m}$ by 10% and increasing I_{arc} by 10% (case 2-->3) had the effect of increasing the electron temperature by ~25%. Radial profiles of T_e, resulting from the technique discussed in section 4.2.3, are flat at the centerline values given in Fig. 5.19 for r < 3-4 mm. A typical radial T_e profile for the case $P/\dot{m}$=22.4 MJ/kg was shown in Fig. 5.14. These results, despite their flat profiles, are likely slightly parabolic according to the results of Tilley, et al. (1994). They noted that T_e measurements made with a triple probe were artificially inflated due to misalignment between the probe electrodes and the flow direction. More specifically, they noted that a misalignment of 30° caused a 6% artificial increase in the T_e measurement. Since the misalignment between the flow and the quadruple probe increases with distance from the thruster centerline,

it is suspected that the edges of the T_e profiles typified by Fig. 5.14 have been artificially increased through this mechanism. This results in the apparent flat T_e radial profile indicated in Fig. 5.14. Despite this effect, the T_e profiles are much wider than the n_e profiles measured in this study.

Based on Figs. 5.17 and 5.18, the parameter $P/\dot{m}$ is not a useful variable with which to study changes in n_e. That is, no clear trend is apparent in the effect of $P/\dot{m}$ on the electron density. To a slightly lesser extent, this is true for the electron density (Fig. 5.19). These results indicate that the individual effects of varying I_{arc} and$\dot{m}$ are important, rather than the overall effect of the parameter $P/\dot{m}=(I_{arc})(V_{arc})/\dot{m}$. This point is expanded upon in sections 6.1.2 and 6.2.5 which discuss comparisons of these results with previous experimental and numerical results, respectively.

Results for the ion current collected by the two crossed electrodes (P_3 and P_4) of the quadruple probe were also recorded. For the region of the thruster plume investigated, the resulting profiles of the current ratio I_4/I_3 were very uniform over the region r<3 mm as shown above in Fig. 5.15. The measured values of I_4/I_3 were 0.6, 0.6, and 0.5 for the conditions $P/\dot{m}$=19.8, 22.4, and 26.0 MJ/kg, respectively. From Fig. 4.8 with f=0.9, these correspond to values of the ion speed ratio $u_i/c_{m,H^+}$ of 1.0, 1.0, and 0.7 for cases 1-3. A value of $u_i/c_{m,H^+}$ ~1 indicates that the most probable thermal speed of H^+ is the same as its directed velocity. The most probable thermal speed is greater than the directed plasma velocity for $u_i/c_{m,H^+}$ <1. Combining these results for $u_i/c_{m,H^+}$ with the time-of-flight velocity data shown in section 5.2 results in estimates of the gas temperature T_g as discussed in section 5.3.5. The results for centerline estimates of T_g are shown in Fig. 5.20 for the three values of $P/\dot{m}$ investigated in this study. Uncertainties are large because the

value of T_g depends on several other measurements. Also, recall that the values of T_g are likely *upper limits* via the mechanism discussed in section 5.3.5. Radial profiles of T_g for the three operating conditions are shown in Fig. 5.21. Since the value of $u_i/c_{m,H^+}$ is relatively flat in the region r<3 mm, the radial profile of T_g is determined primarily by the shape of the measured axial velocity profile $u_i(r)$. As such, increases in uncertainty in the velocity results for large radii (see section 4.3.6) correspond to even larger uncertainties in T_g for locations far from the centerline.

5.3.7 Floating Probe Electric Field Estimates

A double floating probe configuration (electrodes P_1 and P_2 of Fig. 2.4) was used to estimate the radial electric field E_r near the thruster exit plane. For two floating probes in a plasma with electrode sheath potentials V_{s1} and V_{s2}, and a measured floating potential difference between the two electrodes $\Delta V_f = V_{f2} - V_{f1}$, the difference in the plasma potential ΔV_p between the two electrodes is related to ΔV_f by:

$$\Delta V_p = \Delta V_f - (V_{s2} - V_{s1}) \tag{5.2}$$

The result of a typical ΔV_f measurement is plotted in Fig. 5.22 for the $P/\dot{m}$=22.4 MJ/kg case. The sign reversal of the signal for the two peaks ($|\Delta V_f| \approx 0.2$ V) at r = 5.5 mm is a consequence of electrode orientation remaining constant during a probe sweep while the plasma potential gradient changes sign, relative to the direction of the sweep, across the plume. From Eq. (5.2), ΔV_p can be found from ΔV_f and the probe sheath drops. For a single floating electrode (I=0), the sheath potential drop V_s is derived by summing the ion

and electron current into the probe and solving for the potential that satisfies the zero net current requirement. This yields an electrode sheath potential of

$$V_s = \frac{kT_e}{2e} \ln\left(\frac{m_i}{m_e}\frac{T_e}{T_i}\right) \tag{5.3}$$

Since the logarithm term does not vary by more than 2% over the electrode separation, the difference in electrode sheath potentials is

$$V_{s2} - V_{s1} = \Delta V_s \cong \frac{\Delta(kT_e)}{2e} \ln\left(\frac{m_i}{m_e}\frac{T_e}{T_i}\right) \tag{5.4}$$

Near the thruster centerline, the change in T_e over the 1.4 mm electrode separation [$\Delta(kT_e)$] is slight due to the measured flat T_e radial profile (Fig. 5.14). For $\Delta(kT_e)$ as large as 0.01 eV (~500 K), ΔV_s is < 0.04 V, allowing the sheath drop to be neglected in Eq. (5.2). Therefore $\Delta V_f \approx V_{p2}-V_{p1}$, generated by a radial electric field E_r at the thruster exit plane. The resulting plot of E_r versus radial position is shown in Fig. 5.23. The field is approximately zero at the center as expected, and is radially inward inside the plume, with a peak of ~ 100 V/m near r=2 mm. The field apparently peaks at ~ 200 V/m at r ≈ 5 mm, but this is likely a consequence of large gradients in T_e and n_e at the plume edge, voiding the assumption of small ΔV_s.

The floating probe measurements of E_r are evidence for the existence of current density and ohmic heating in the near-field plume. From the measured n_e, the estimated ionization fraction on the centerline is $\alpha \approx 10^{-4}$, giving a plasma electrical conductivity of $\sigma \approx 100$ mho/m. In the exit plane (at

r = 2 mm) E_r ~ 100 V/m, which is equivalent to $j_r=\sigma E_r$~1 A/cm^2. If this current is flowing across an area of approximately 0.2 cm^2, the total current crossing the exit plane amounts to ~0.2 A, or 2% of the total current supplied to the arcjet. Furthermore, this current represents a small amount of ohmic heating (j^2/σ~1 W/cm^3) in the exit plane region.

The indication of current in the near-field plume is consistent with the boundary condition that j must be perpendicular to the anode wall at a 20° angle to the centerline, forcing a current component perpendicular to the exit plane in the plume. These measurements carry implications for downstream boundary conditions for arcjet numerical models.

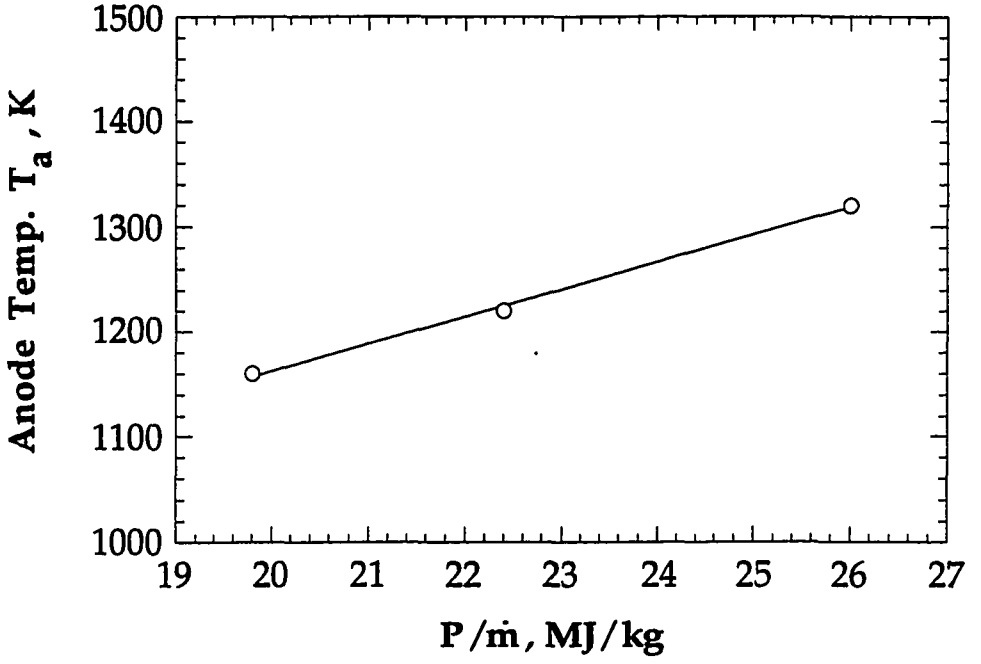

Fig. 5.1 Arcjet anode steady state operating temperature versus thruster specific power (P/ṁ).

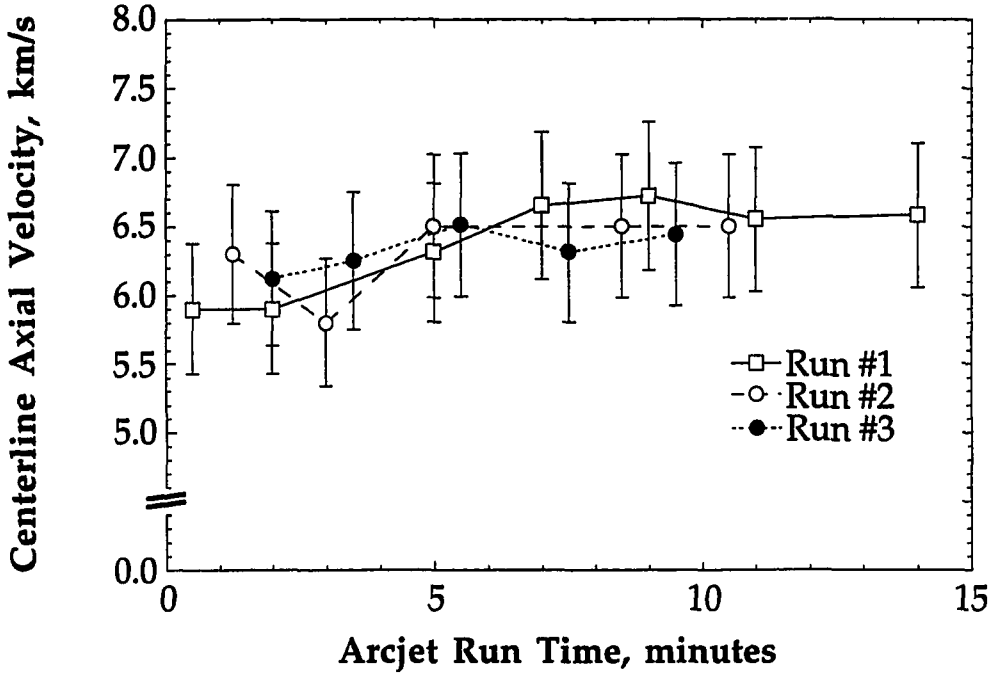

Fig. 5.2 Measured centerline axial velocity versus time elapsed after arcjet ignition from a "cold start." Three different thruster warm-up processes are depicted.

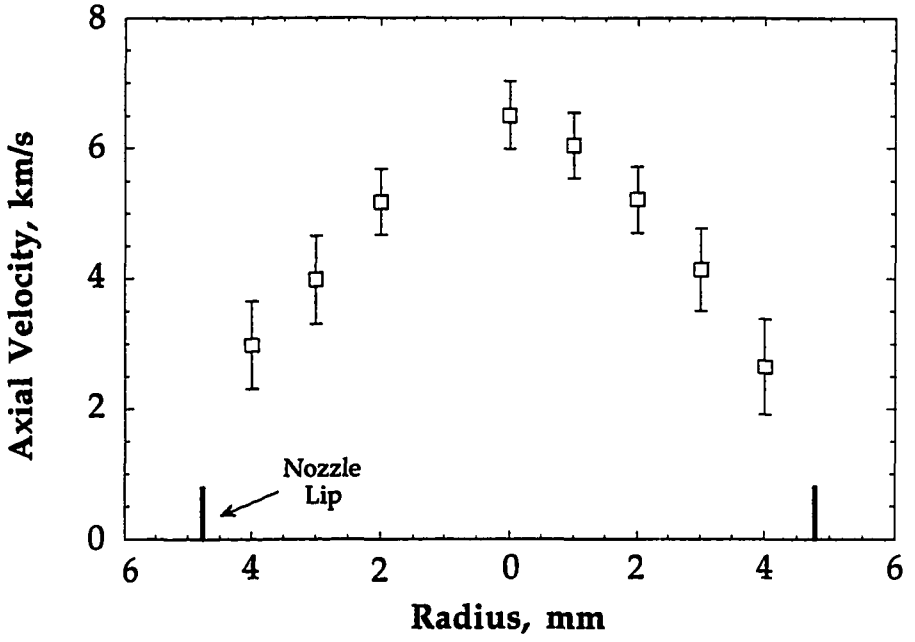

Fig. 5.3 Axial velocity profile measured with the time-of-flight probe for the case of $P/\dot{m}$=22.4 MJ/kg. The TOF probe tip was located 1 mm from the thruster exit plane.

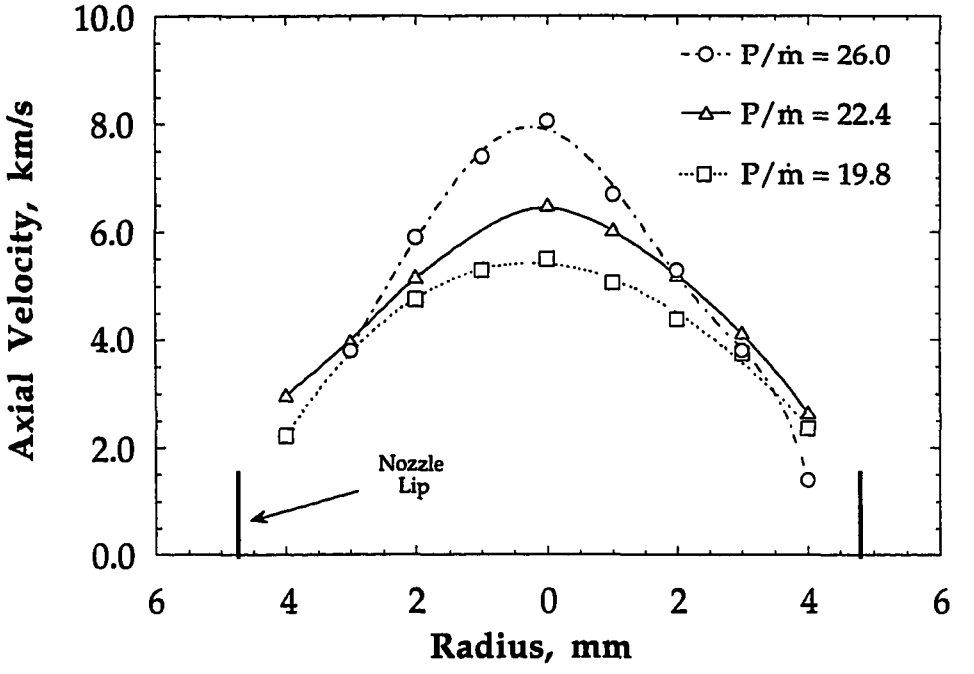

Fig. 5.4 Radial profiles of the plasma axial velocity measured for three different thruster specific powers ($P/\dot{m}$). Error bars are not shown for clarity, but are similar to those shown in Fig. 5.3.

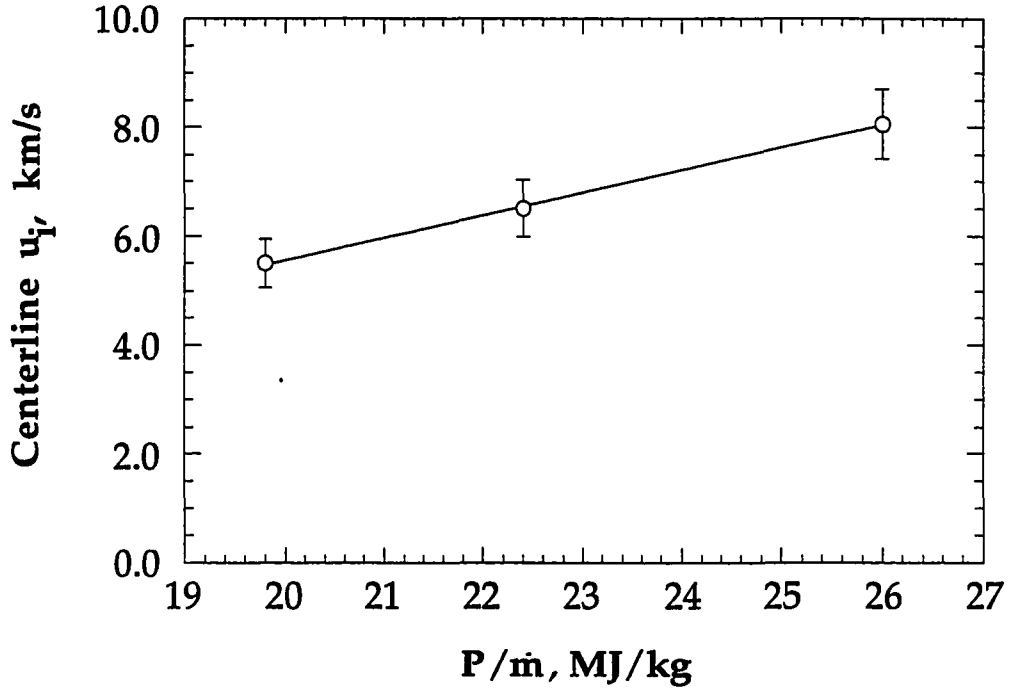

Fig. 5.5 Centerline axial velocity versus thruster specific power P/ṁ. The solid line is a straight line fit through the data.

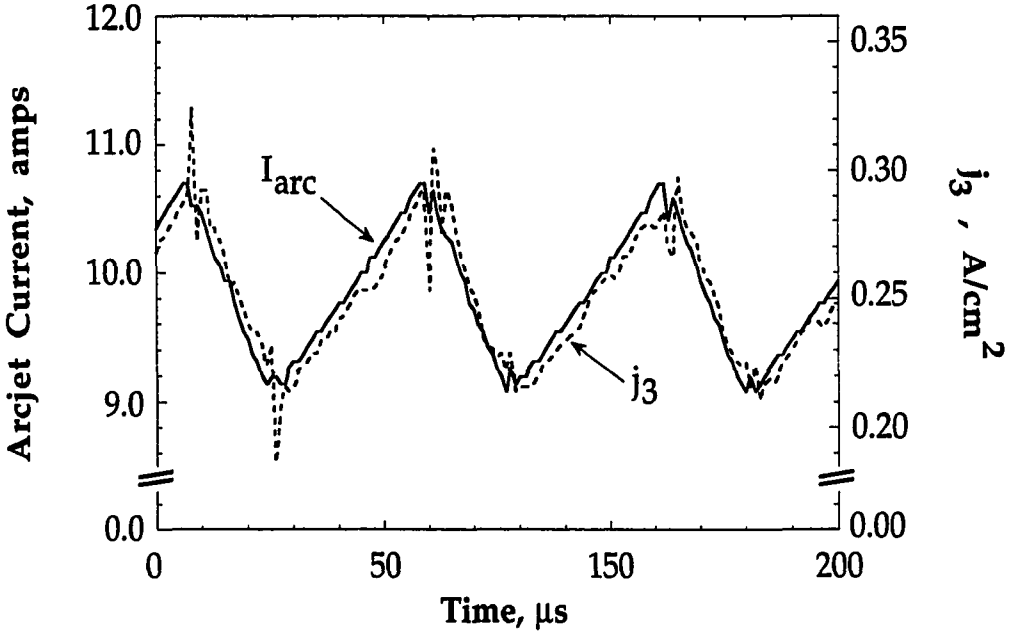

Fig. 5.6 Arcjet current and quadruple probe current density j_3 (= I_3/A_3) versus time showing the effects of the PPU ripple. The convective time delay between the cathode tip and the probe is 3-4 μs.

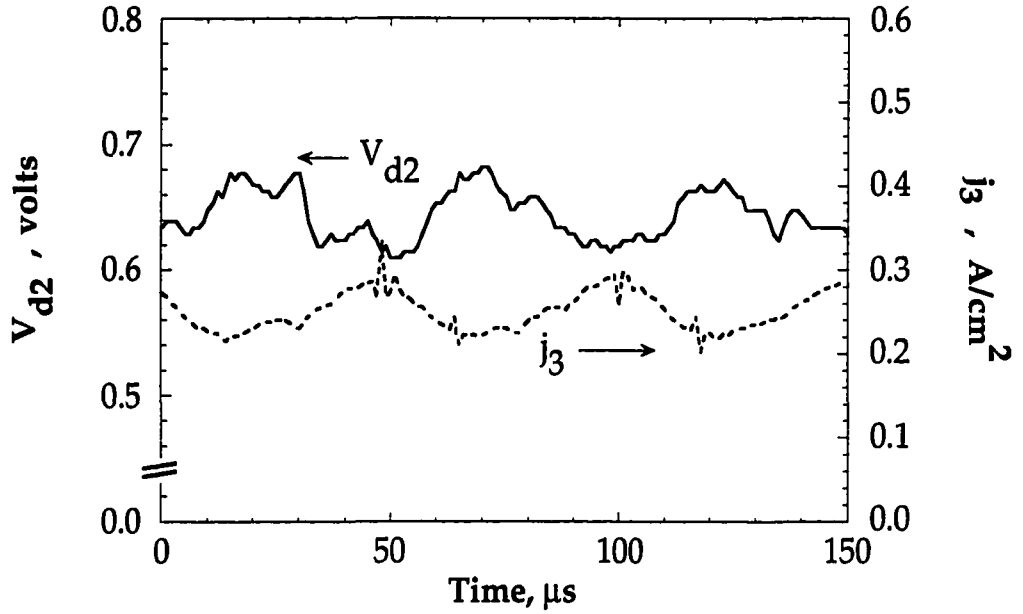

Fig. 5.7 Centerline quadruple probe measurements of V_{d2} and j_3 ($=I_3/A_3$) versus time. Figures 5.6 and 5.7 show that n_e increases and T_e decreases with increases in I_{arc}.

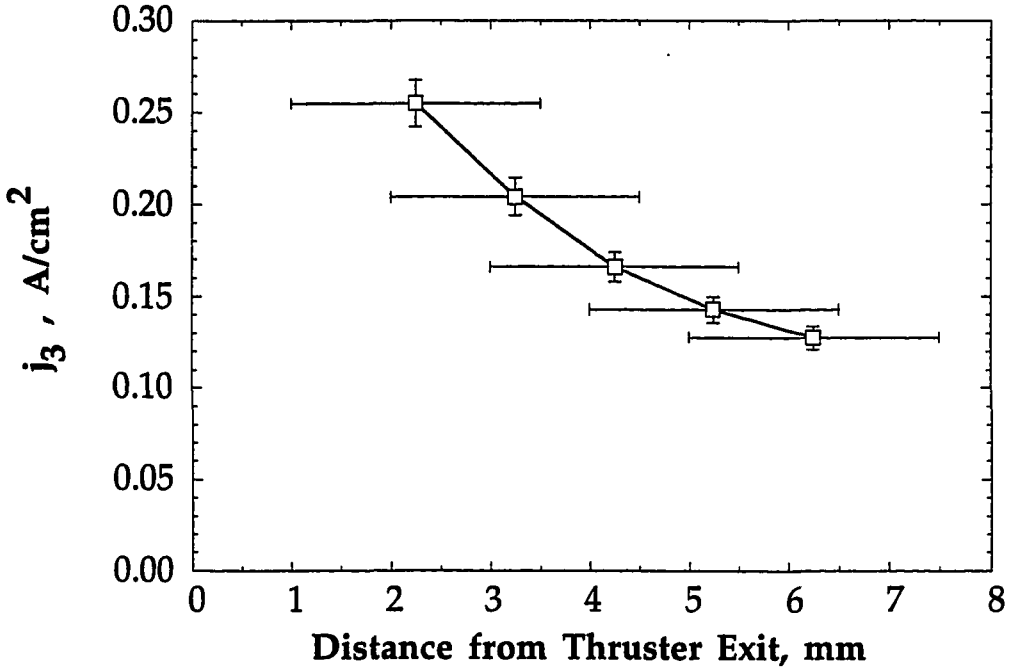

Fig. 5.8 Axial variation of the ion saturation current density j_3 ($=I_3/A_3$) measured by the quadruple probe. Horizontal error bars are 2.5 mm long, indicating the length of electrode 3.

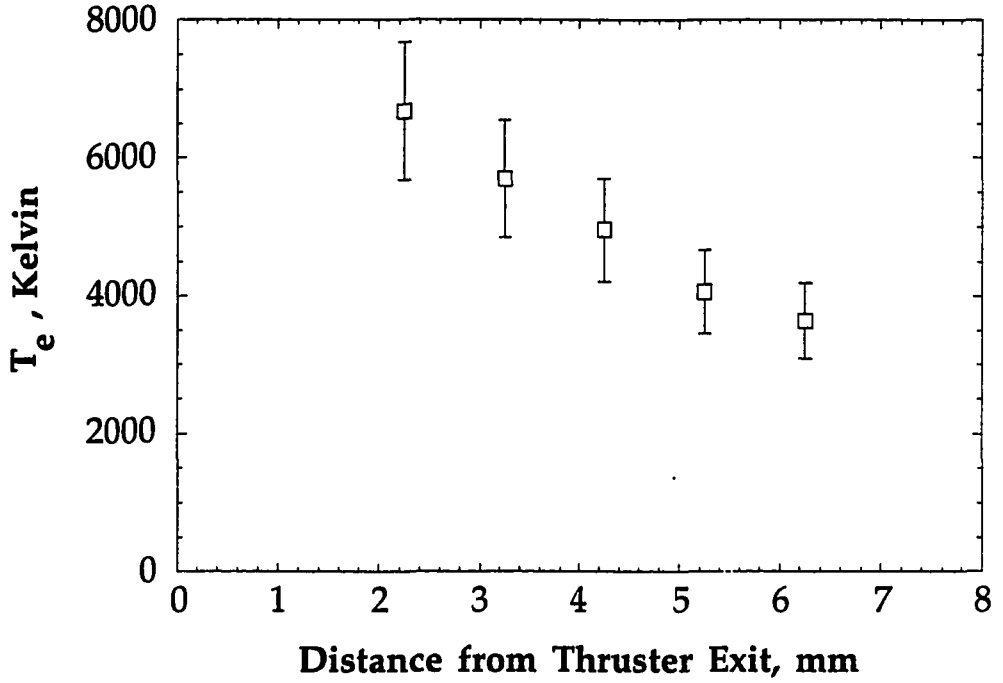

Fig. 5.9 Axial variation of centerline quadruple probe measurements of the electron temperature T_e.

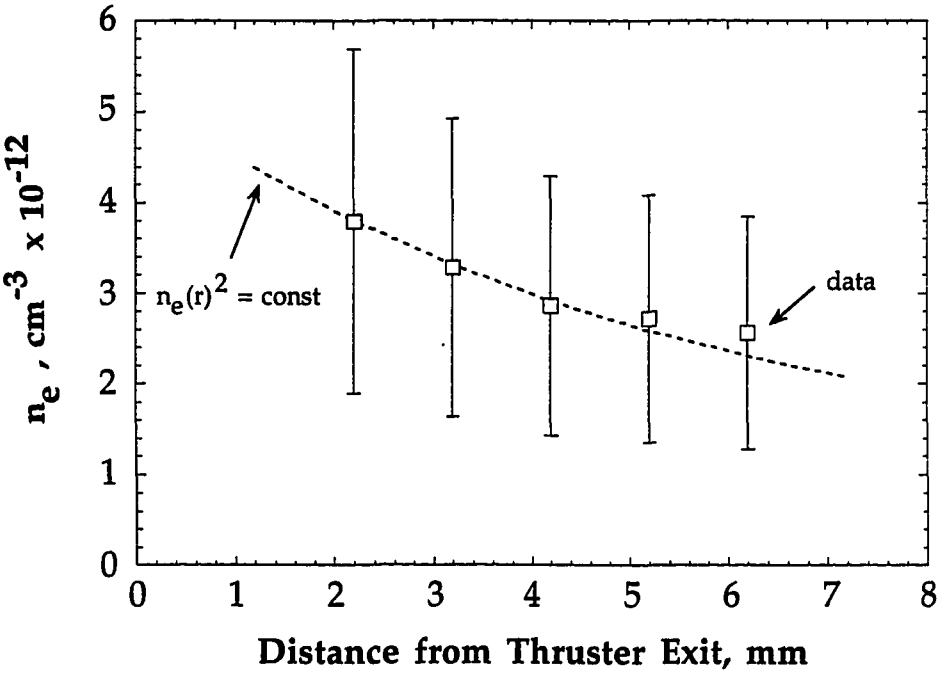

Fig. 5.10 Axial variation of centerline quadruple probe measurements of n_e. The n_e gradient is ~ -0.5 x 10^{12} cm^{-3}/mm at x=2.2 mm. The dashed line represents a spherical expansion originating at the arcjet constrictor.

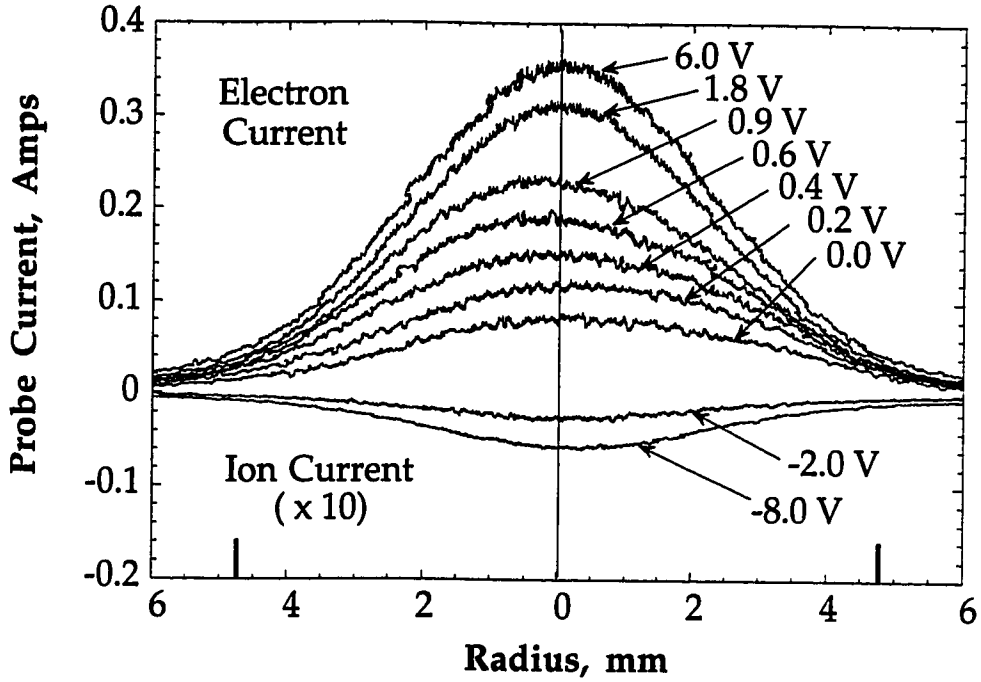

Fig. 5.11 Single probe measurements demonstrating arcjet plume symmetry. Curve labels represent electrode bias voltages . Cross plots at constant radii yield single probe V-I characteristics.

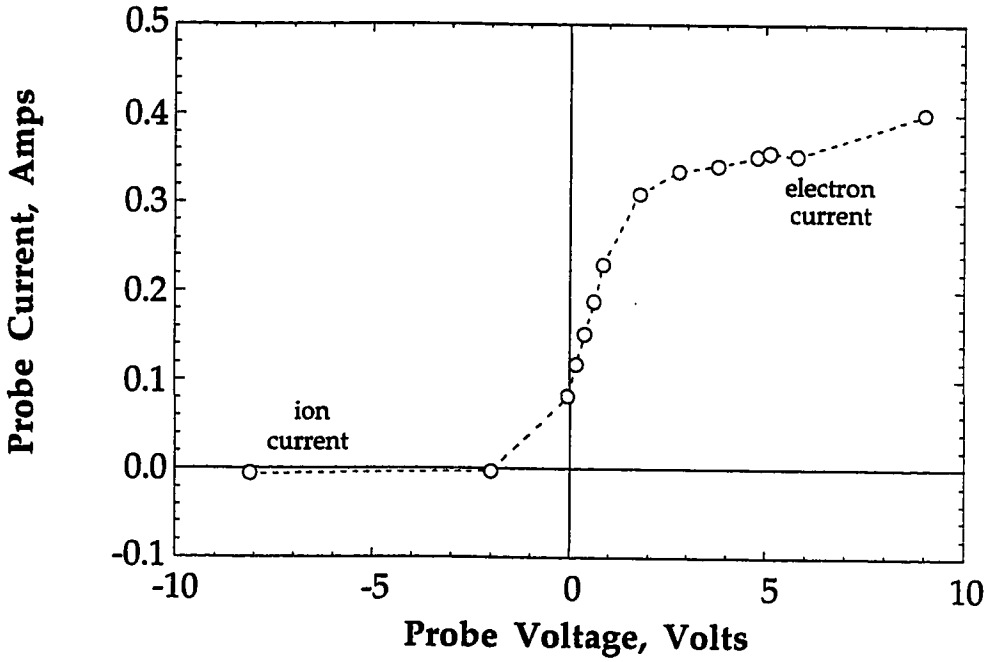

Fig. 5.12 Single probe V-I characteristic extracted from Fig. 5.11 at r=0.0 mm. Using the method described in Chapter 3, these data represent T_e ~0.6 eV and $n_e \sim 7 \times 10^{12}$ cm^{-3}.

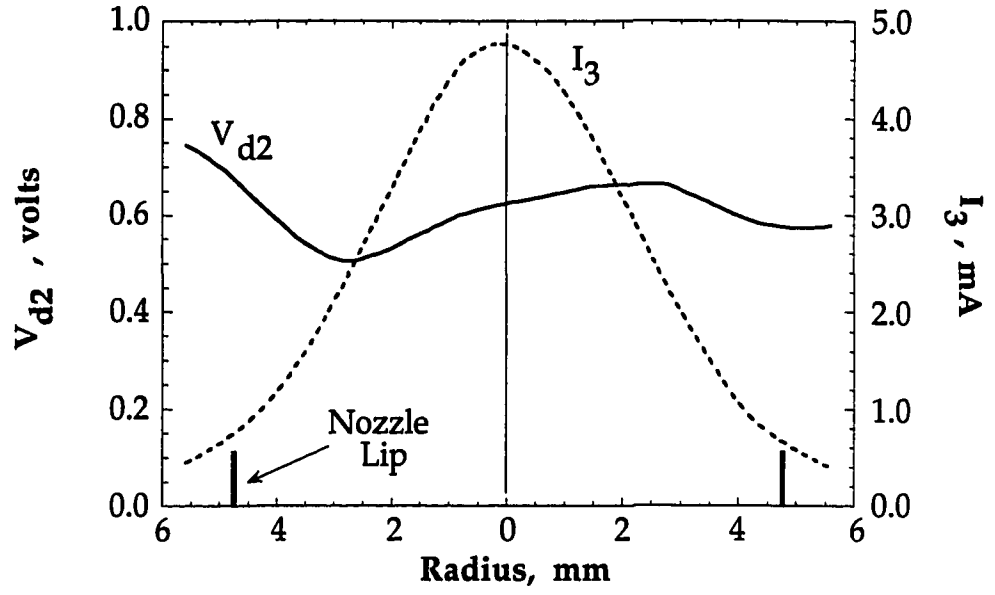

Fig. 5.13 Smoothed profiles of $I_3(r)$ and $V_{d2}(r)$ measured by the quadruple probe during a typical radial probe sweep.

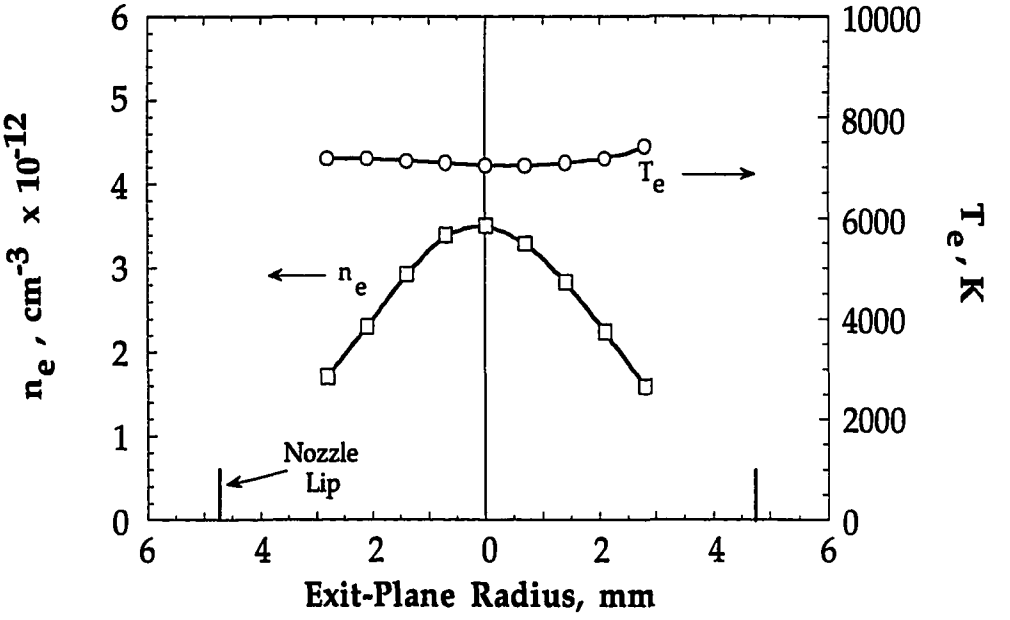

Fig. 5.14 Radial profiles of T_e and n_e extracted from the quadruple probe data using the radial gradient model. Uncertainties in T_e and n_e are ± 15% and ± 50%, respectively, for centerline measurements.

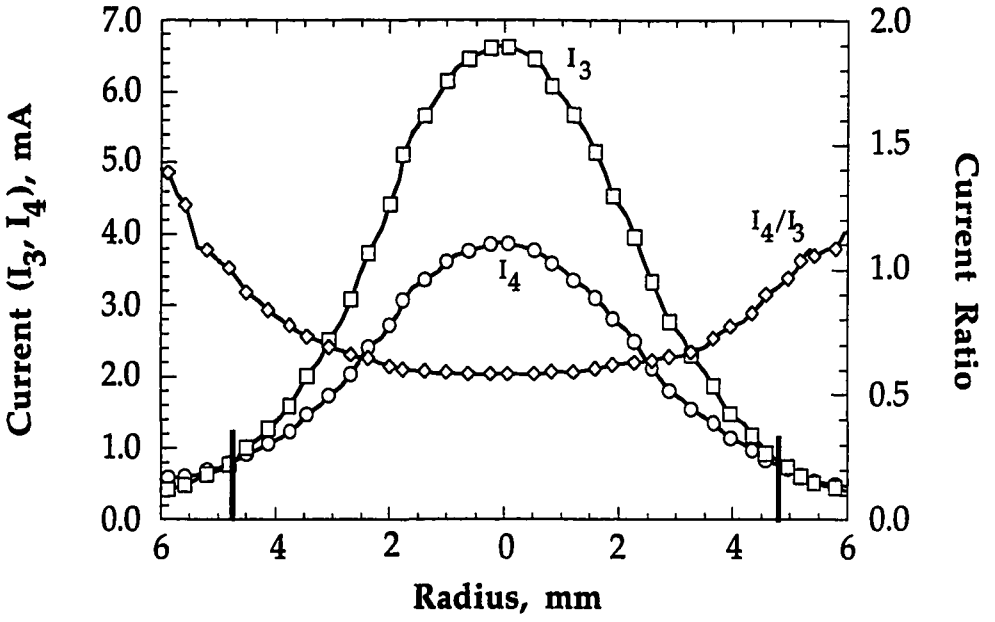

Fig. 5.15 Quadruple probe currents I_3 and I_4 giving $u_i/c_{m,H^+} \sim 1$ on the thruster centerline for the $P/\dot{m}$=22.4 MJ/kg case.

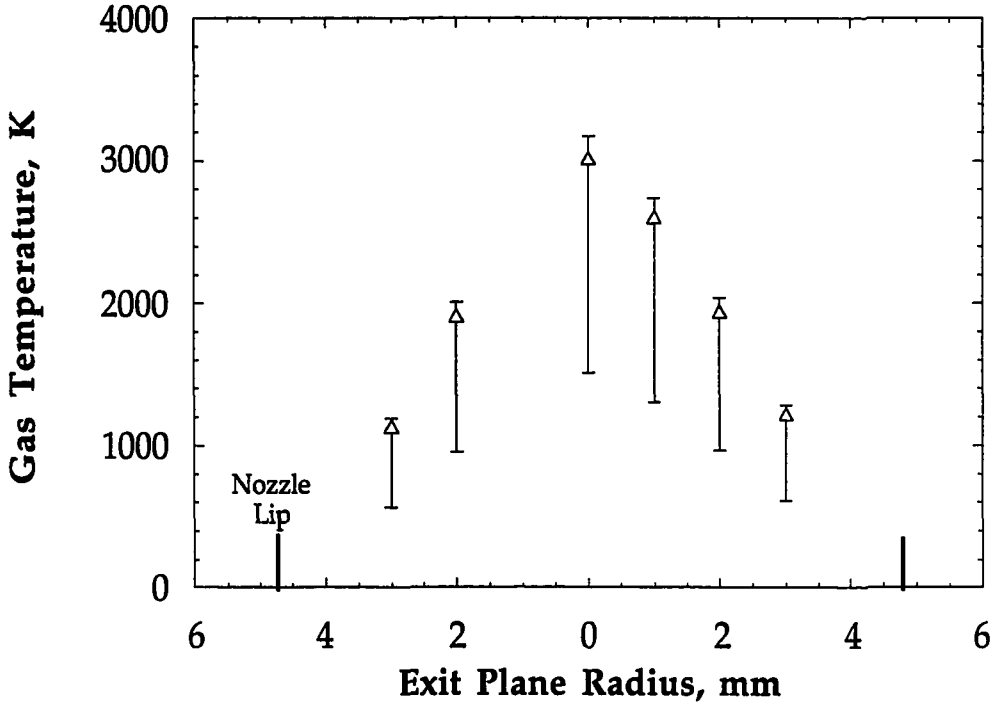

Fig. 5.16 Gas temperature radial profile estimates based on measurements of u_i and $u_i/c_{m,H^+}$ for the case of $P/\dot{m}$=22.4 MJ/kg.

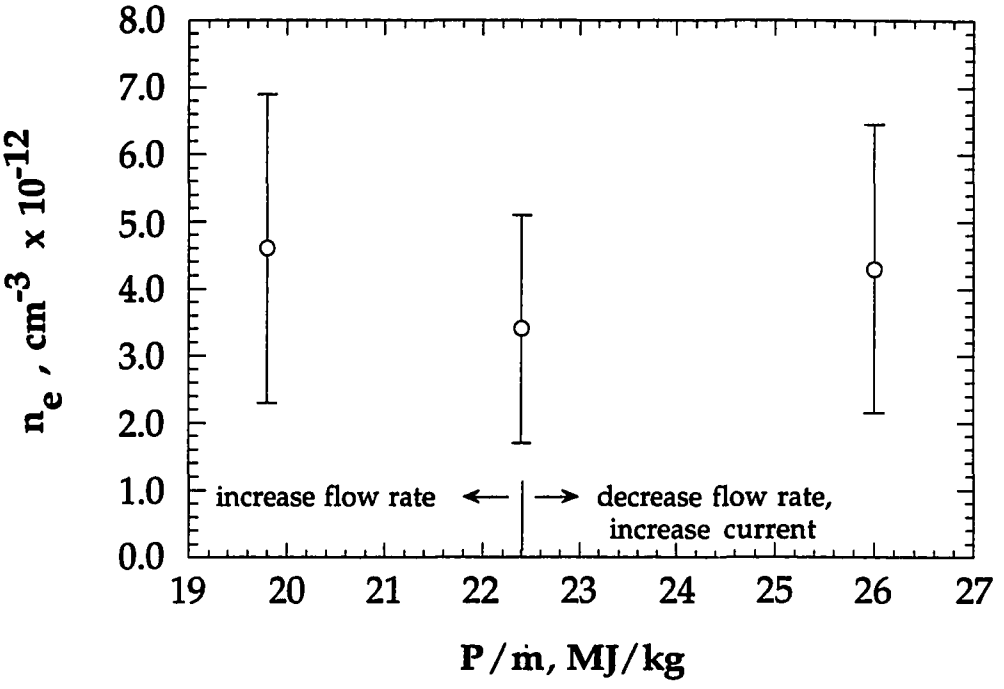

Fig. 5.17 Centerline quadruple probe measurements of n_e versus thruster specific power.

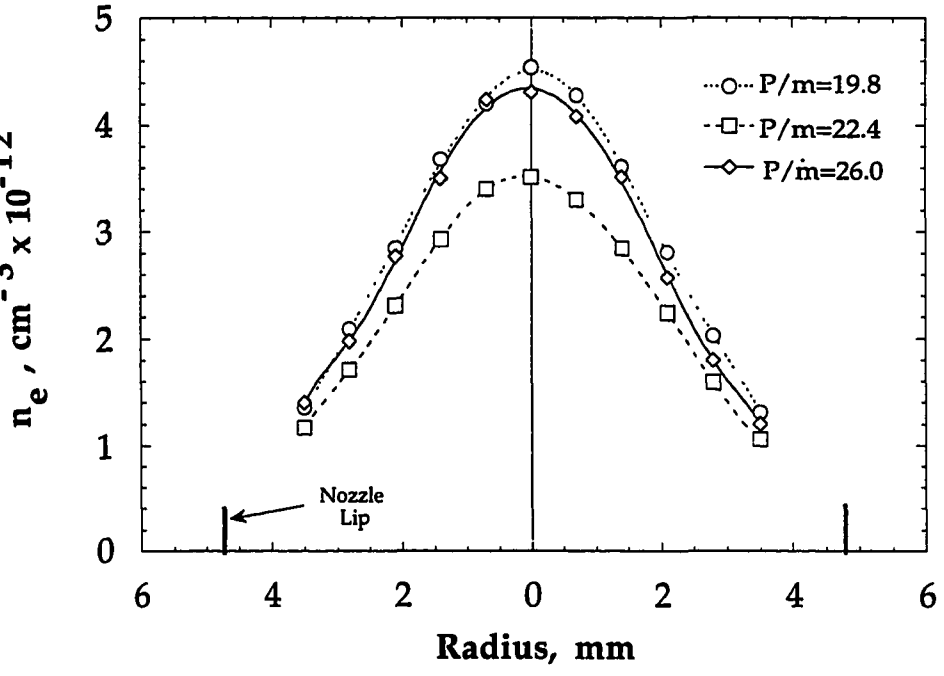

Fig. 5.18 Radial n_e profiles measured by the quadruple probe for the three thruster operating conditions examined in this study. The uncertainty in n_e is ± 50%, and is not shown for clarity.

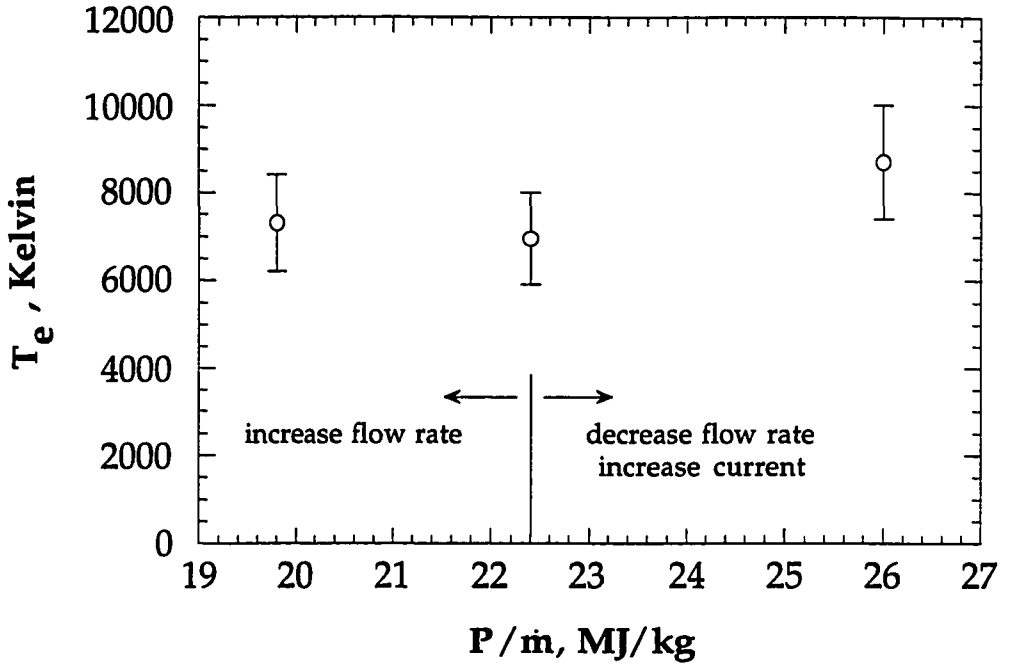

Fig. 5.19 Centerline quadruple probe measurements of electron temperature versus thruster specific power.

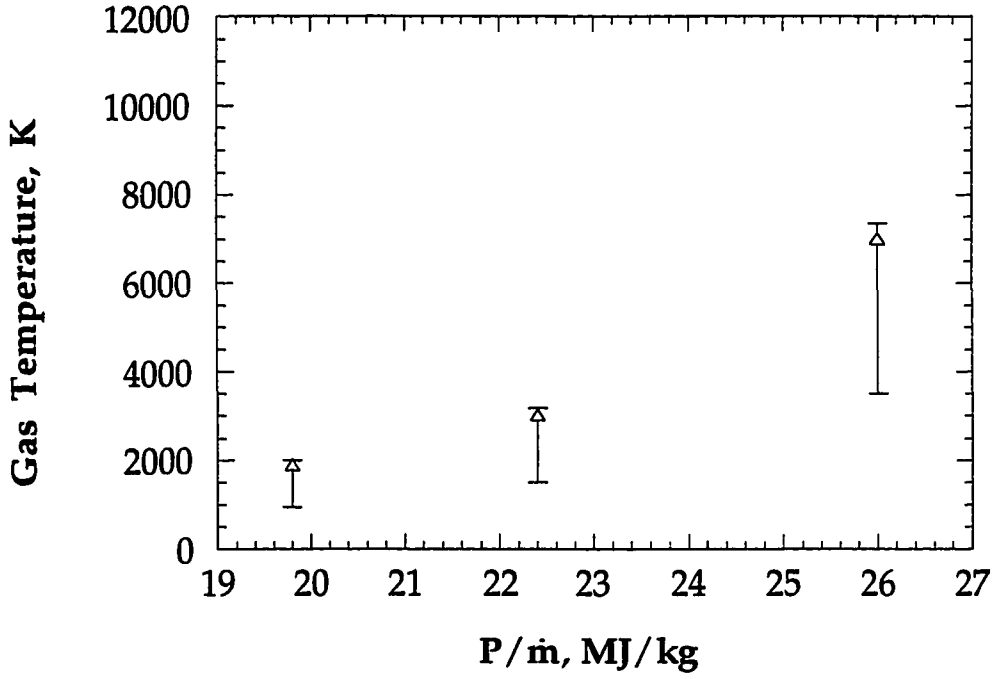

Fig. 5.20 Estimated gas temperature T_g versus thruster specific power. Uncertainties are large (+5%/-50%) due to propagation of uncertainties in the measured quantities u_i and $u_i/c_{m,H^+}$.

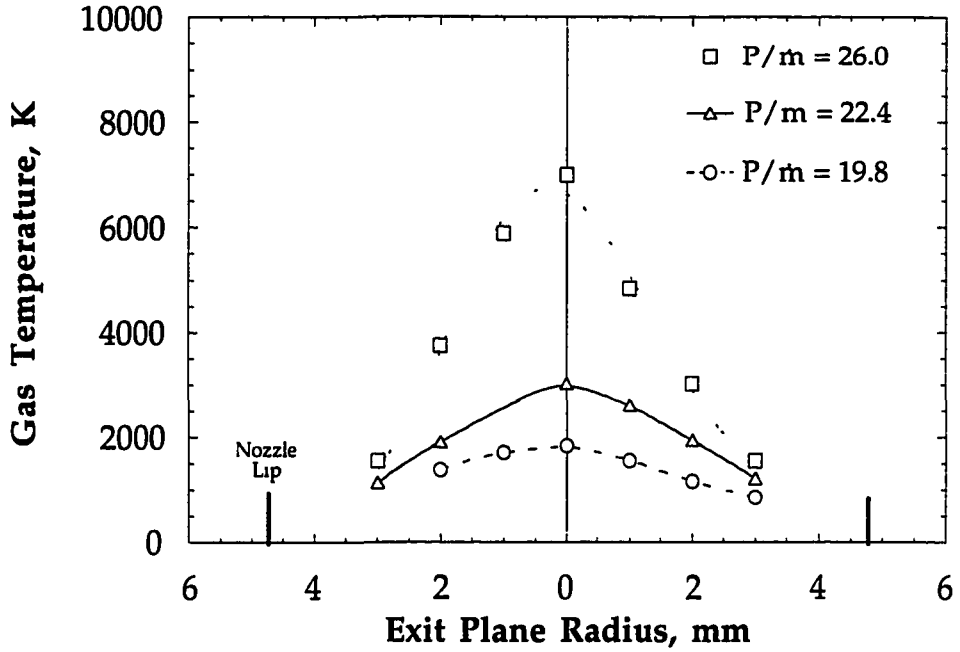

Fig. 5.21 Estimated gas temperature profiles based on measurements of u_i and $u_i/c_{m,H^+}$ for three thruster specific powers. The uncertainty in the T_g estimates is + 5%/- 50%. Curves are drawn through the profiles for clarity only.

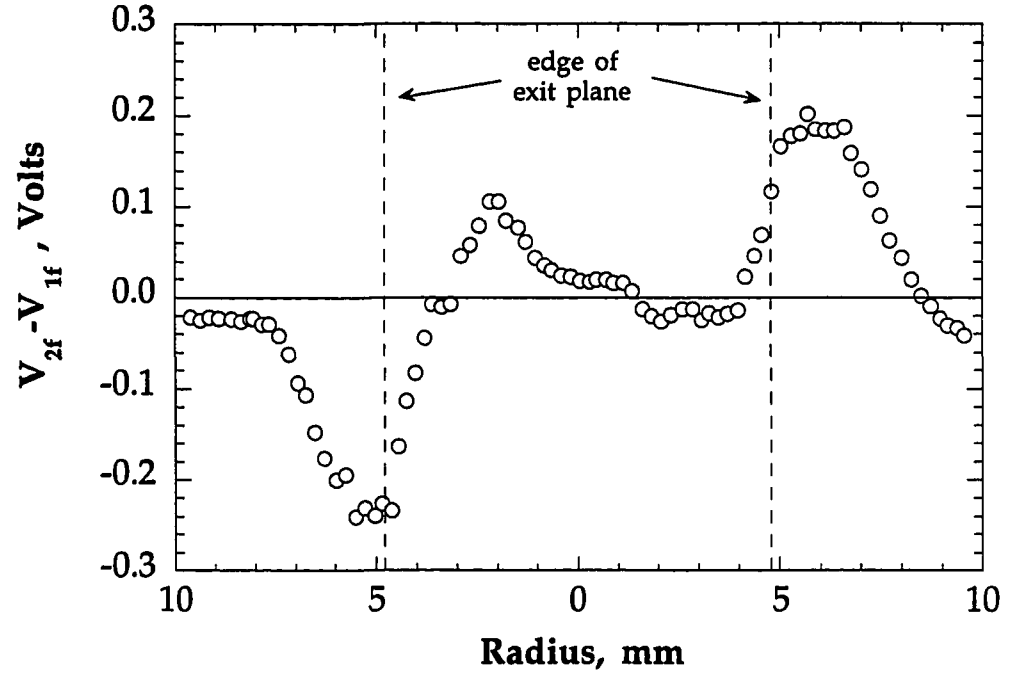

Fig. 5.22 V_{2f}-V_{1f} measurement made with the radial double probe configuration.

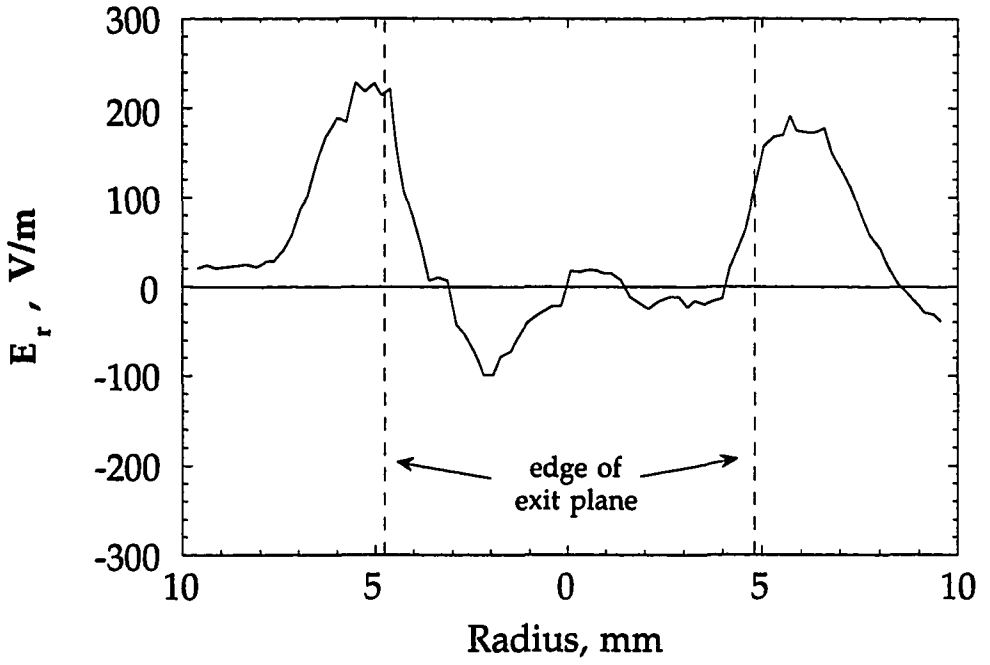

Fig. 5.23 Radial E-field E_r versus position across the thruster face.

6. Comparison of Data with Previous Results

6.1 Comparison with Experimental Results

In order to evaluate the experimental techniques used in this study, comparisons are made with the results of previous experiments performed under similar conditions. One of the primary goals of this research, however, is to add to the relative lack of published data for the exit plane region of the hydrazine arcjet. As such, few experimental studies exist that have presented results in the region of the hydrazine arcjet plasma investigated here. As discussed in Chapter 1, a vast majority of the experimental work performed on low power arcjets has been for thrusters operating on hydrogen propellant. The remaining fraction of experimental work in this area has historically been split between ammonia and hydrazine thrusters.

The global performance of the arcjet used in this work is compared with that of an identical 1-kW hydrazine thruster investigated by Curran and Haag (1992). Comparisons of steady state thruster current, voltage, power, and specific power $P/\dot{m}$ are presented. Measurements of thruster specific impulse I_{sp} are also available from the work of Curran and Haag for the conditions investigated in the present work.

Results of T_e, n_e, and T_g measured in this study are compared with previous data that were acquired for the nozzle *interior* region, immediately upstream of the region investigated here ($2.2<x<6.2$ mm). These data were measured by Zube and Myers (1993), who used emission spectroscopy to make measurements of the nozzle interior region through a series of small holes bored into the thruster anode wall. The emission spectroscopy electron density results of Manzella, et al. (1990) are also presented, for x=0 and 1 mm.

The axial profiles of T_e and n_e measured in this research are further evaluated by comparing them with the Langmuir probe results of Sankovic (1990) and Carney and Sankovic (1989) for 30<x<150 mm and x=320 mm downstream of the thruster exit, respectively. Although these results do not constitute a direct comparison with data in the region 2.2<x<6.2 mm, they help demonstrate the extent of the axial T_e and n_e gradients between the thruster interior and far-field plume regions.

As of this writing, there exist no previous velocity data for low-power *hydrazine* arcjets, making a direct comparison with the axial velocity results of this study impossible. However, the experimental velocity data are discussed below in the context of I_{sp} as an indication of the average exit velocities of hydrazine and hydrogen arcjets.

6.1.1 Global Thruster Performance Measurements

A summary of the arcjet global performance parameters measured in this research and in the work by Curran and Haag (1992) for an identical thruster geometry and propellant composition are presented below in Table 6.1. In the study by Curran and Haag (1992), the thruster performance (Table 6.1) was evaluated at various points during a several hundred hour endurance test of a new thruster. Each cycle of testing consisted of 2 hours on followed by 2 hours off. Thruster global performance results were presented at the conclusion of 144, 335, and 502 cycles. The results presented in Table 6.1 represent thruster performance measurements made after 144 2-hour cycles. Curran and Haag noted that the thruster voltage V_{arc}, for a given flow rate and current, increased steadily during the endurance test. They report that the operating voltage increased ~6 volts during the first ~300 hours of

thruster operation, while the increase over the remaining ~700 hours was only ~3 volts. The values of V_{arc} measured during this study were 3.1 volts lower than those reported by Curran and Haag, indicating that the arcjet used in this study has likely operated for less than the equivalent of 144 cycles or 300 hours of operation. It is this ~3 volt difference in the arcjet voltage that is responsible for the discrepancy in the reported values of thruster power P and specific power $P/\dot{m}$ presented in Table 6.1.

Setpoint		Present Study			Curran and Haag (1992)			
$\dot{m}$ (mg/s)	I_{arc} (amps)	V_{arc} (volts)	Power (W)	$P/\dot{m}$ (MJ/kg)	V_{arc} (volts)	Power (W)	$P/\dot{m}$ (MJ/kg)	I_{sp} (s)
60	10	118.8	1188	19.8	----	----	----	397†
50	10	112.0	1120	22.4	115.1	1151	23.2	419
45	11	106.5	1171	26.0	109.6	1206	26.5	444

†extrapolated from Curran and Haag data for I_{arc}=10 A, $\dot{m}$=40 and 50 mg/s

Table 6.1 Summary of the arcjet operating conditions measured in this research and those measured by Curran and Haag (1992). Measurements of I_{sp} were not undertaken in the present work. Curran and Haag did not investigate the $\dot{m}$ = 60 mg/s case.

Previous axial velocity measurements at the exit of a low power hydrazine arcjet have not been presented. However, the measured axial velocity results presented in this work can be roughly compared with exit plane velocities from 1-kW arcjets operating on other propellants. Arcjets of the 1-kW class, operating on hydrogen at a specific impulse $I_{sp} = u_e/g_o$ of ~950 seconds, have peak centerline axial velocities at the thruster exit of ~14 km/s (Pobst, et al., 1995a). Comparing the specific impulses of 1-kW hydrogen (~950

s) and hydrazine arcjets (~420 s), it is apparent that the average exhaust velocity u_e for hydrazine thrusters should be roughly 44% that of hydrogen. The measured centerline axial velocities for the hydrazine thruster examined in the present study were 5.5, 6.5, and 8.0 km/s for $P/\dot{m}$ values of 19.8, 22.4, and 26.0 MJ/kg, respectively. Despite the lack of hydrazine arcjet data for a direct comparison, the measured velocity data are within the range of expected values based on the specific impulse arguments discussed above.

6.1.2 Centerline T_e, n_e, and T_g Measurements

The results of centerline measurements of T_e and n_e, along with an estimate of T_g, are compared with the experimental results of Zube and Myers (1993), Manzella, et al (1990), Sankovic (1990), and Carney and Sankovic (1989). All of the experiments discussed here utilized a 1-kW thruster operating on a mixture of $2H_2+N_2$ to simulate hydrazine propellant. Each of the thrusters was geometrically similar to the arcjet used in the present work. The results of Zube and Myers are for the case of I_{arc}=9 amps and $\dot{m}$ = 47.6 mg/s. Although they do not report the steady state value of the thruster operating voltage V_{arc}, it can be estimated from the performance map reported by Curran and Haag (1992) for an identical thruster. Based on the inferred value of V_{arc}, the results of Zube and Myers for I_{arc}=9 amps and $\dot{m}$=47.6 mg/s correspond to a specific power of $P/\dot{m}$=22.1 MJ/kg. Although this operating condition (I_{arc}, $\dot{m}$) does not mirror any of the three used in the present study, its specific power agrees quite well with the $P/\dot{m}$=22.4 MJ/kg (I_{arc}=10 amps, $\dot{m}$=50.0 mg/s) case used in this work. As such, the results of the $P/\dot{m}$=22.4 MJ/kg case (condition 2 in Table 2.1) investigated in the present

work are utilized in the subsequent comparisons of centerline values of T_e, n_e, and T_g discussed below.

The results of Manzella, et al. (1990) correspond to I_{arc}=10 amps and $\dot{m}$=50.0 mg/s, which are identical to the compared results from this study. The results of Sankovic (1990) are for the case of I_{arc}=10 amps, $\dot{m}$=49.0 mg/s. The Carney and Sankovic (1989) results discussed here are for $8<I_{arc}<11$ amps and $\dot{m}$=44.8 mg/s.

The centerline electron temperatures measured in this work for $P/\dot{m}$=22.4 MJ/kg are shown in Fig. 6.1 along with nozzle interior measurements of the atomic hydrogen excitation temperature performed by Zube and Myers (1993). Zube and Myers make several arguments that the measured atomic excitation temperature is very near the free electron temperature T_e. First, they cite close agreement between the atomic excitation temperatures of atomic hydrogen, neutral atomic nitrogen (NI), and singly ionized atomic nitrogen (NII). They state that "given the different cross sections, radiative rates and densities, it seems unlikely that this agreement would occur unless the upper excited state populations were controlled by the same mechanisms of electronic collisional excitation and radiative decay." Second, Zube and Myers state that the electronic energy levels used for the measurements were close to the ionization potentials of the atoms. Finally, they state that the values of n_e they measured via Stark broadening were very near the threshold determined by Griem (1964) for partial local thermal equilibrium, implying that the excitation temperature $T_{ex} \sim T_e$.

The present measurements of T_e in the region $2.2<x<6.3$ mm appear to be slightly higher than expected based on the electron temperature estimates of Zube and Myers in the arcjet interior. Considering the degree to which the

electron temperature can be estimated by the atomic excitation temperature T_{ex}, and the experimental uncertainties in T_{ex} (10-15%) and T_e (15%), the agreement is quite good. Although not represented in Fig. 6.1, the electronic excitation temperature has also been very roughly estimated by Manzella, et al. (1990) to be ~5000-5500 K in the vicinity of the thruster exit plane, based on spectroscopic measurements and an assumption of Boltzmann equilibrium.

A summary of relevant centerline electron temperature measurements is presented in Fig. 6.2 for -10<x<350 mm. In addition to those depicted in Fig. 6.2, the single Langmuir probe results of Sankovic (1990) and Carney and Sankovic (1989) are presented. The horizontal and vertical "error bars" on the data by Sankovic represent T_e data acquired with several different probe geometries over the region 30<x<150 mm. In this region, no clear trend in T_e as a function of axial location could be inferred from the data. The vertical "error bar" on the Carney and Sankovic data represents T_e measurements for several arcjet currents between 8 and 11 amps at x=320 mm. Again, the error bar is utilized because no clear trend was observed for T_e in terms of thruster current for these data. The data shown in Fig. 6.2 demonstrate that a very large gradient (~ -7500 K/cm) in T_e is apparently present in the thruster nozzle region and during the first ~ 5 mm downstream of the thruster. For 30<x<320 mm, the gradient is much more gradual, at ~ -55 K/cm. Based on the shape of the T_e axial profile measured in the present study, it appears that the transition between these two regions begins to occur at x ~ 6 mm as the slope of the measured T_e profile begins to decrease.

Results of the centerline electron density measurements for this study and for the work of Zube and Myers (1993) are shown in Fig. 6.3. While the n_e gradient based on the data from the present study is large near the exit

($dn_e/dx \sim -0.5 \times 10^{12}$ cm^{-3}/mm at x= 2-3 mm), it is small compared with the axial gradient indicated in the nozzle interior near the exit plane. These results imply that n_e varies by approximately 2 orders of magnitude over the 5 mm range defined by -3<x<2 mm, apparently resulting from the very sudden expansion as the flow leaves the confines of the arcjet nozzle and enters the vacuum environment. It thus appears likely that very large axial variations in the n_e gradient (large d^2n_e/dx^2) are present in the thruster very near-field plume. Over the 5 mm range of probe locations investigated in this study, n_e drops by ~ 30%, with the magnitude of dn_e/dx increasing slightly near the thruster exit.

A similar trend has been noted by Laser Induced Fluorescence measurements of the hydrogen atom density n_H in a 1-kW hydrogen arcjet of similar geometry (Pobst, et al., 1995b). In that study, a decrease in centerline H atom density of ~40% was observed for 2<x<6 mm. Despite the differences in propellants, the similarities in the n_H and n_e gradients over 2<x<6 mm hint that the n_e gradient measured in the present study is due the plasma expansion process rather than electron-ion recombination processes.

The n_e results presented in Fig. 6.3 are shown along with the emission spectroscopy results of Manzella, et al. (1990) and the Langmuir probe results of Sankovic (1990) and Carney and Sankovic (1989) in Fig. 6.4. The electron densities measured in the present study appear consistent with the data of previous researchers with the exception of the data of Manzella, et al. (1990) for x=0 and x=11 mm. However, these data represent upper limits placed on n_e based on Stark broadening of line-of-sight (non-Abel inverted) emission spectroscopy signals, and thus are consistent with the quadruple probe data measured in this study.

The very substantial n_e gradients presumed to exist in the nozzle and plume region bounded by -10<x<10 mm (Fig. 6.3) require extra care in locating and reporting probe positions for both optical and intrusive measurement techniques.

Results of N_2 vibrational and rotational temperature measurements performed by Zube and Myers (1993) in the thruster nozzle ($P/\dot{m}$=22.1 MJ/kg) are shown along with the estimate of T_g for the $P/\dot{m}$=22.4 MJ/kg case investigated in the present study in Fig. 6.5. The value of T_g determined in this study is approximately 1500 K higher than the vibrational temperatures expected near the exit plane based on the results of Zube and Myers. However, the uncertainty in T_g is quite large (+5%/-50%) due primarily to the uncertainty in the value of the plasma composition factor f ($=n_{H+}/n_{N+}$). Additionally, T_g is determined in part by the current measured by the perpendicular electrode of the quadruple probe (see Fig. 2.4). The fact that this electrode collects current over its 2 mm length artificially inflates the measured value of T_g through the mechanism discussed in section 5.3.5.

A limited amount of experimental data exists with which to compare the effects of varying thruster $P/\dot{m}$ on measurements of T_e and n_e. A parametric study of the effect of varying thruster specific power on T_e and n_e by changing I_{arc} and $\dot{m}$ was performed by Sankovic (1990). In that study, centerline electron temperatures and densities were measured with a Langmuir probe at a location ~100 mm downstream of the thruster exit plane. Results were presented for arcjet currents of 6, 8, and 10 amps and simulated hydrazine flowrates of 30, 35, 40, and 45 mg/s. A summary of the results of Sankovic is shown in Figs. 6.6 and 6.7, which show measured n_e and T_e, respectively, as a function of thruster current and flowrate (i.e., . $P/\dot{m}$). In

general, Sankovic noted that the electron density measured at x~100 mm increased with increasing arcjet current for a given propellant flow rate. Similarly, n_e also increased with increasing flow rate for a constant arcjet current (Fig. 6.6). In this study, similar trends were noted for measurements of n_e at x=2.2 mm in terms of varying $P/\dot{m}$ through I_{arc} and $\dot{m}$. The centerline values of T_e and n_e measured in the present study are summarized below in Table 6.2.

Operating Condition	$\dot{m}$ (mg/s)	I_{arc} (amps)	$P/\dot{m}$ (MJ/kg)	n_e (cm^{-3})	T_e (K)
1	60.0	10.0	19.8	4.6×10^{12}	7300
2	50.0	10.0	22.4	3.5×10^{12}	7000
3	45.0	11.0	26.0	4.3×10^{12}	8700

Table 6.2 Summary of centerline n_e and T_e quadruple probe measurements at x=2.2 mm for the operating conditions investigated in this study.

In increasing the propellant flow rate 20% from 50 to 60 mg/s for I_{arc} =10 amps (case 2 --> case 1 in Table 6.2), the measured electron density increased ~30%. These results are roughly consistent with the those of Sankovic who noted that a ~30% increase in $\dot{m}$ from 35 to 45 mg/s caused a corresponding ~40% increase in n_e for I_{arc}=10 amps. It is difficult to draw similar conclusions regarding the effect of varying $P/\dot{m}$ between cases 2 and 3 in Table 6.2 since both I_{arc} and $\dot{m}$ were varied in that instance. In moving from case 2 (10 amps, 50 mg/s) to case 3 (11 amps, 45 mg/s), one would expect an increase in n_e due to increasing the arcjet current, but also a decrease in n_e due to decreasing $\dot{m}$, based on the results of Sankovic (Fig. 6.6). Therefore, no

clear agreement or disagreement between the results of this study and those of Sankovic can be distinguished in this instance.

The results of Sankovic (1990) for electron temperature measurements for varying I_{arc} and $\dot{m}$ were much less conclusive than the n_e results published in that work. For fixed arcjet currents of 6 and 8 amps, no clear trend was established for the effect on T_e for varying $\dot{m}$. However, for the case of I_{arc}=10 amps, the electron temperature was observed to increase nearly uniformly with decreases in $\dot{m}$. In the present study, increasing the flow rate by 20% (case 2 --> 1) caused no measurable difference in the electron temperature, considering the ± 15% uncertainty in the quadruple probe T_e measurements. For a fixed $\dot{m}$, Sankovic did observe a clear trend indicating that increasing the thruster current from 6-10 amps in two amp increments decreased the measured electron temperature. As with the n_e results discussed above, no direct comparison can be made with the results of Sankovic for cases 2 and 3 (see Table 6.2) because both $\dot{m}$ and I_{arc} were varied between these cases in the present study.

6.1.3 Arc Current Estimate at the Thruster Exit Plane

In section 5.3.7, the results of a double floating probe measurement were presented, which allowed estimates of the radial electric field and the amount of the thruster current I_{arc} that was present at the x=2.2 mm measurement location. These results revealed that ~2%, or 0.2 amps, of the arcjet current (10 amps) crossed the exit plane before reattaching to the anode surface (see discussion in section 5.3.7). These results are substantiated by the work of Curran, et al. (1990), who performed measurements of the current attachment distribution along the nozzle wall of a 1-kW arcjet with overall

dimensions identical to the thruster used in this study. They "segmented" the thruster anode in the axial direction so that it consisted of 5 conducting sections that were electrically insulated from each other. By measuring the current drawn by each of the 5 sections, they were able to infer the current attachment distribution in the arcjet. For $\dot{m}$= 49.7 mg/s of $2H_2+N_2$ and I_{arc}= 10 amps, Curran, et al. noted that ~ 50% (5 amps) of the thruster current attached to the segment nearest the nozzle exit, which consisted of the last ~5 mm of the nozzle (just under half of the nozzle length), including the thruster exit plane. While most of the thruster current attached to the most downstream segment, it is difficult to surmise where, along the segment length, the current of 5 amps was attaching.

The work by Curran, et al., while an excellent and original addition to the literature, has received some constructive criticism regarding the effect of the segments and electrical insulators on the steady state operation of the arcjet. For example, the operating voltage of the segmented thruster is ~20 volts higher than an unsegmented version of the same thruster, implying that the plasma conductivity and, hence, the electron distribution have been substantially altered by the presence of the segments. Additionally, the segmented nozzle body was observed to operate ~ 300 K hotter than an unmodified thruster, indicating that the heat conduction mechanism in the nozzle block was significantly modified by the presence of the segments. Despite the effects of the segment sections on the thruster performance, the results of Curran, et al., (1990) seem to substantiate the estimates of the present study that a significant portion of the arcjet current is present at the nozzle exit plane. Presently, work is being conducted by Tiliakos, et al. (1995) to measure the current attachment distribution in a 1-kW arcjet by using

several small (<<1 mm dia.) conducting pins distributed along the nozzle wall. The authors believe that this approach will allow measurements of the current attachment distribution without significantly modifying the fundamental operating physics of the thruster.

6.2 Comparison with Numerical Model Predictions

Experimental studies are generally a necessary step in the development and understanding of complicated physical systems like arcjets. Of equal importance, however, are numerical or computational approaches for modeling the complex processes involved in arcjet operation. A well developed and tested numerical model can be used as an invaluable design tool. However, during the model development phase, experimental and numerical efforts are best utilized concurrently. Through this interaction, experimental results can be used both to help determine model boundary conditions and to validate the model performance. A comprehensive computational arcjet modeling effort has recently been undertaken by Megli, Krier, and Burton (1995). Since this effort stands alone in its ability to model the complex flow of N-H plasmas in 1-kW hydrazine arcjets, results of this experiment will be compared with the predictions of this model. The key aspects of this model are discussed in detail by Megli (1995) and are summarized very briefly below.

6.2.1 Brief Description of the Numerical Model

The arcjet model developed by Megli, et al. (1995) is an axisymmetric, seven species (H_2, N_2, H, N, H^+, N^+, e) hydrogen/nitrogen plasma code that utilizes a PISO algorithm to solve the computational domain up to the exit plane. Separate energy equations are formulated and solved for the electrons

and the heavy species. The anode temperature distribution is included, and the plasma electrical conductivity is coupled with the plasma properties, which allows a self-consistent solution for the current distribution. The model is capable of both thermal and chemical nonequilibrium simulations, which along with its ability to vary the mixture ratio of hydrogen and nitrogen, distinguishes it from previous numerical modeling efforts. A complete discussion of the model and assumptions can be found in the dissertation by Megli (1995).

Comparisons are made between the experimental results measured in this study and model predictions for a 1 kW-class arcjet operating on a gaseous mixture of $2H_2+N_2$ to simulate fully-decomposed hydrazine propellant. The arcjet geometry modeled is identical to that if the 1-kW thruster utilized in this study. For the model results discussed below, chemical and thermal nonequilibrium simulations are employed.

6.2.2 Comparison of Global Performance Results

The thruster operating conditions used by the model to compare with the experimental results of this study are summarized in Table 6.3. In comparing the experimental results with model predictions, the propellant flow rate $\dot{m}$ and thruster current I_{arc} were matched. Because the model solved for the resulting arcjet voltage V_{arc} based on $\dot{m}$ and I_{arc}, the specific powers of the experimental and numerical results were not necessarily equal. As shown in Table 6.3 below, the model tended to underpredict the arc voltage and, hence, the thruster specific power. Despite this discrepancy between the thruster powers, the parameters $\dot{m}$ and I_{arc} were used to compare

the model with experiment, since these were the variables set in the laboratory environment.

		Experiment			Model, (Megli, 1995)		
Case	I_{arc} (amps)	$\dot{m}$ (mg/s)	V_{arc} (volts)	$P/\dot{m}$ (MJ/kg)	$\dot{m}$ (mg/s)	V_{arc} (volts)	$P/\dot{m}$ (MJ/kg)
1	10	60.0	118.8	19.8	63.1	101.9	16.1
2	10	50.0	112.0	22.4	51.4	93.6	18.2
3	11	45.0	106.5	26.0	43.0	86.8	22.2

Table 6.3 Comparison of the arcjet operating voltage V_{arc} and specific power $P/\dot{m}$ for the experiments of this study and the numerical predictions of Megli (1995).

6.2.3 Comparison of Centerline Data and Predictions

The centerline electron temperature predicted by the model for case 2 in Table 6.3 is shown in Fig. 6.1, along with the results of this study and those of Zube and Myers (1993). Based on the experimental results, it appears that the model is underpredicting T_e near the exit plane by a factor of ~ 2. This trend is consistent with experimental results and the predictions of this model for 1-kW *hydrogen* arcjets as well. For ~13 mg/s of hydrogen propellant, the model predicts T_e~2700 K at the exit plane (Megli, 1995), while the electrostatic triple probe results of Pobst, et al. (1993) show electron temperatures of 5000-6000 K at a location 25 mm *downstream* of the hydrogen thruster exit. Thus, the electron temperature at the exit plane of the 1-kW hydrogen arcjet is expected to be larger than the value of 2700 K predicted by the model.

A possible cause of this discrepancy in the predicted and measured values of T_e is illuminated by examining the electron energy equation. The computational model, which imposes the condition of zero current at the thruster exit plane, does not account for the possibility of adding energy to the electrons near the exit plane via ohmic heating. The experimental results of section 5.3.7, however, reveal that a finite amount of current j and ohmic heating (j^2/σ ~1 W/cm^3) are present downstream of the arcjet exit plane. A rough, first order analysis of the electron energy equation, neglecting all source and sink terms except for ohmic heating, reveals that the change in T_e due to this term may be greater than ~ 2000 K/mm for the conditions measured in this work at x = 2.2 mm. These results indicate that the numerical model exit plane boundary condition may need revision. However, a more in depth analysis of this topic is clearly warranted.

Note that model predictions of thrust, u_i, I_{sp} and T_g (Megli, 1995) are relatively unaffected by the discrepancy in the electron temperature, since the relative electron concentration is low ($n_e/n_{neutral} < 0.001$). Internal nozzle diagnostics are currently being performed by Tiliakos, et al. (1995) and are expected to help resolve this discrepancy between experimental results and numerical model predictions. Despite the discrepancy between T_e predictions and estimates, the centerline heavy particle temperature T_g model predictions agree favorably with the experimental estimate of the present study for case 2 of Table 6.3, as shown in Fig. 6.5.

The centerline n_e predicted by the model and experiments for case 2 in Table 6.3 is depicted in Fig. 6.3. Given the largely varying axial n_e gradients discussed above, the model results seem consistent with experimental plume data of this study and the interior measurements of Zube and Myers (1993).

Because of these large gradients, a direct comparison between the measured radial n_e profile at the exit plane (probe tip = 1 mm from exit) and the computational model profile is not possible.

6.2.4 Comparison of Radial Profiles

Fig. 6.8 shows a comparison between the results of the time-of-flight (TOF) probe measurements and model exit plane predictions of the axial velocity profile for case 2 in Table 6.3. The center of the TOF probe corresponds to an axial location of x=3.5 mm. The centerline axial gradient in the axial velocities predicted by the model at the exit plane is ~ -30 m/s per mm, which corresponds to only ~0.1 km/s over the 3.5 mm separation between the model prediction and measurement locations. Agreement of the radial profiles of axial velocities is excellent and within experimental error in most locations. The numerically predicted profile is slightly more narrow and peaked than the measured profile. This is an expected result because the model flow is constrained in the nozzle (no-slip at wall), which differs from the free expansion that occurs in the plume in the vicinity of the TOF probe.

The heavy particle temperature profile determined from the quadruple probe and TOF probe data is shown along with the model prediction in Fig. 6.9. Both the model and experimental results correspond to case 2 in Table 6.3. Since the measured electron temperature radial profile is flat as shown by the radial gradient model in section 5.3.4, comparisons are not made with the model exit plane predictions. Additionally, a direct comparison of the experimental and predicted radial n_e profiles can not be undertaken due the very large axial gradients in n_e presumed to exist near the thruster exit plane. However, the measured trends of all of the measured parameters, as they

vary with $P/\dot{m}$, will be compared with model predictions in section 6.2.5 below.

6.2.5 Comparison of the Effect of Varying $P/\dot{m}$

A summary of the effect of varying $P/\dot{m}$ on quadruple probe measurements and model predictions of n_e and T_e is shown in Table 6.4. The experiments were conducted with the probe centered at an axial location of x=2.2 mm and the model predictions represent exit plane results. All of the values presented in the table are centerline measurements and predictions. Although the electron densities differ by ~2 orders of magnitude due to the large axial gradients near the exit plane (Fig. 6.4), the trends of the effect of varying $\dot{m}$ and I_{arc} can be compared for the experimental results and model predictions. From Table 6.4, it can be seen that the trends in n_e are very similar for the model and experiments for varying $\dot{m}$ and I_{arc}. These results are consistent with the results of Sankovic (1990), above. Similarly, the directional trends in the electron temperature measurements and model predictions are the same, despite the vastly different magnitudes in T_e, as discussed above.

	Experiment			Megli (1995)	
Case	$P/\dot{m}$ (MJ/kg)	n_e (cm^{-3})	T_e (K)	n_e (cm^{-3})	T_e (K)
1	19.8	4.6×10^{12}	7300	3.5×10^{14}	3250
2	22.4	3.5×10^{12}	7000	3.1×10^{14}	3030
3	26.0	4.3×10^{12}	8700	3.2×10^{14}	3160

Table 6.4 Comparison of centerline (x=2.2 mm) n_e and T_e measurements of this study with the numerical exit plane predictions of Megli (1995).

The model axial velocity predictions, despite the fact that the model predicts increased I_{sp} with increased $P/\dot{m}$ similar to the results observed by Curran and Haag (1992), vary less than ~2% for the range of specific power investigated in this study. For the three thruster operating conditions 1-3 in Table 6.3, the centerline axial velocities predicted at the exit plane are 6870, 6740, and 6770 m/s, respectively. This is in direct contrast to the axial velocities measured with the TOF probe of 5500, 6500, and 8000 m/s for conditions 1-3, respectively. These results are summarized in Fig. 6.10, which shows predicted centerline axial velocities versus the measured time-of-flight probe results for the three values of $P/\dot{m}$ investigated here. Recall that the model underpredicts the arc voltage and therefore the value of $P/\dot{m}$. As such, the model and experimental results correspond to similar thruster currents I_{arc} and flowrates $\dot{m}$ as summarized in Table 6.3. The exhaust velocity u_e ($=g_o I_{sp}$) predicted by the model for these operating conditions is also shown in Fig. 6.10. Since I_{sp} is a measure of the thruster exit velocity weighted by the mass of the exhaust expelled at that velocity, this could be an indication that the density profiles in the arcjet plume and those predicted by the model may be vastly different.

Figure 6.11 shows centerline values of the predicted gas temperature T_g at the exit plane versus the T_g estimates of this research. As was the case with the axial velocity results, the model and experiment agree only for case 2 in Table 6.3 ($P/\dot{m}$=22.4 MJ/kg). However, the large uncertaintities in the experimentally determined values of T_g preclude any strong conclusions regarding the model performance. This apparent large increase in the experimental values of T_g with increases in $P/\dot{m}$ may imply a corresponding decrease in the centerline bulk gas density. This trend seems consistent with

the above argument that the *gas* density profiles of the model and experiment may be quite different despite the accurate model prediction of I_{sp}.

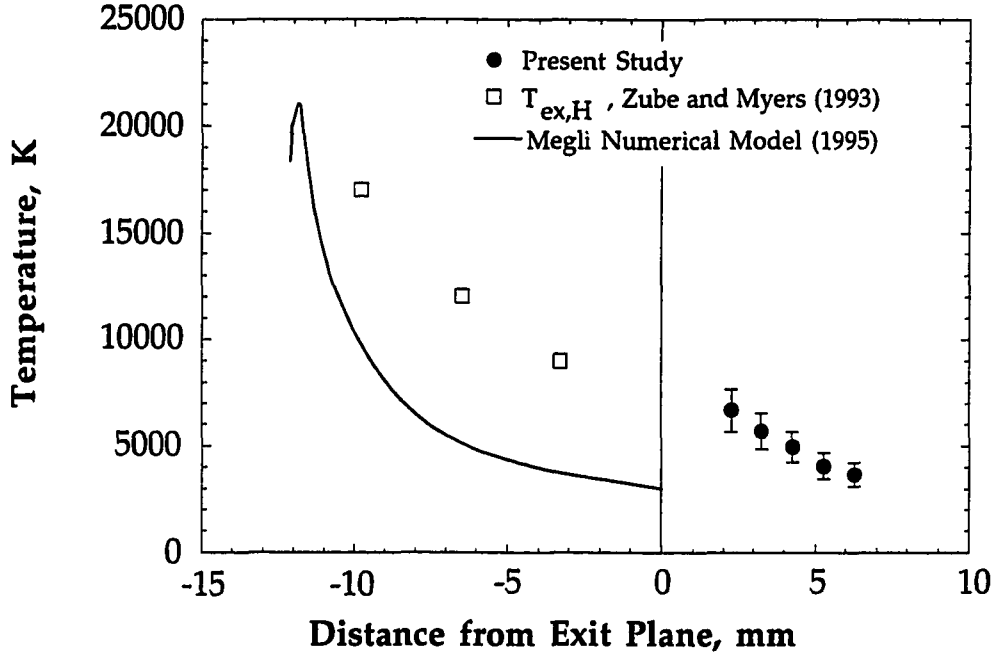

Fig. 6.1 Comparison of the T_e measurements of this study, the T_e numerical predictions of Megli (1995) and hydrogen excitation temperature $T_{ex,H}$ measurements of Zube and Myers (1993).

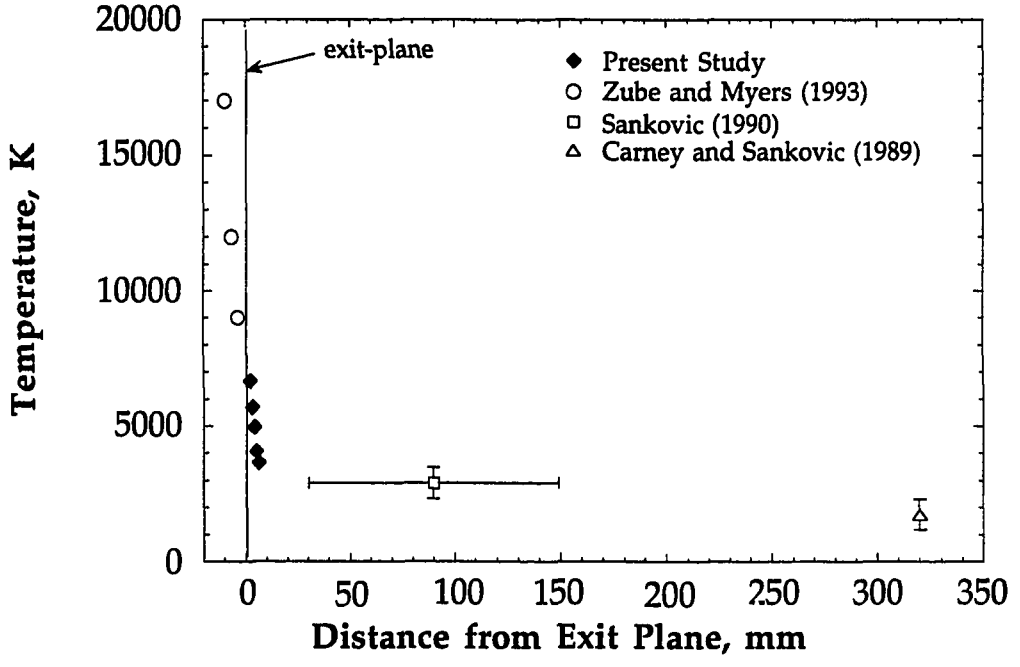

Fig. 6.2 Summary of T_e and $T_{ex,H}$ experimental results. Error bars indicate a range of the measured quantity and/or a range of measurement locations.

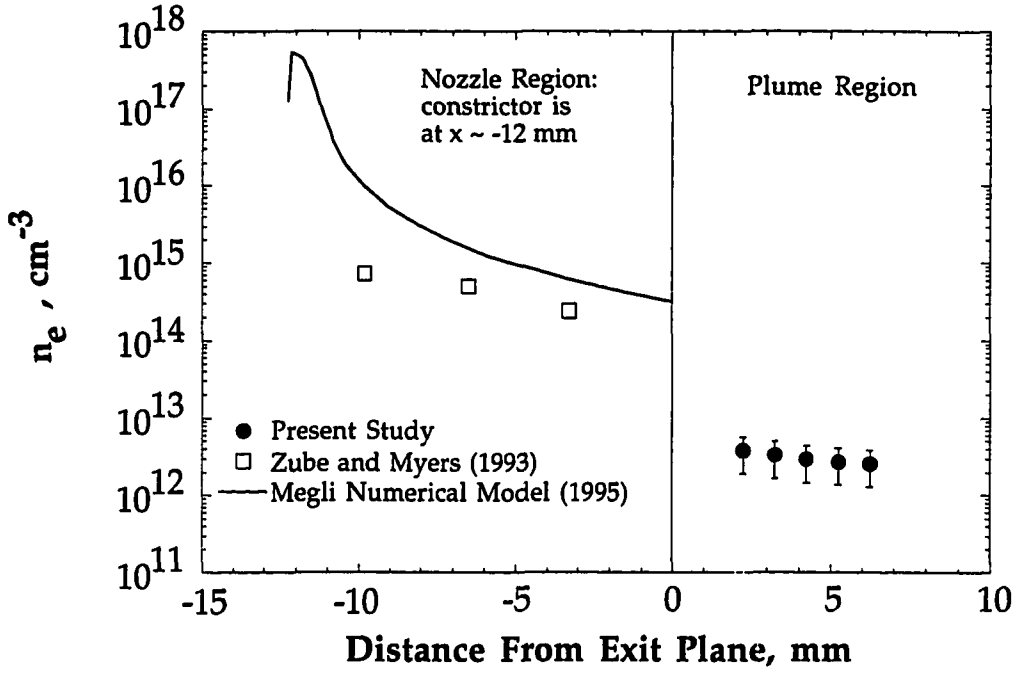

Fig. 6.3 Comparison of the n_e measurements of this study, the experimental results of Zube and Myers (1993), and the numerical predictions of Megli (1995).

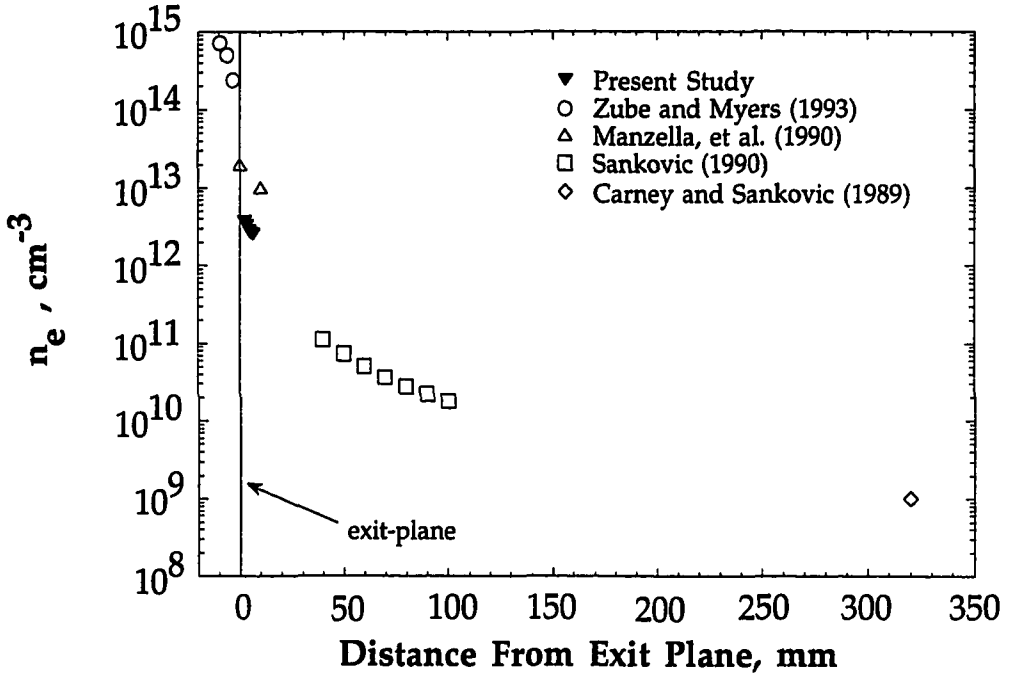

Fig. 6.4 Comparison of centerline n_e results of this work with previous experimental efforts demonstrating that the electron density varies by nearly 6 orders of magnitude over ~350 mm.

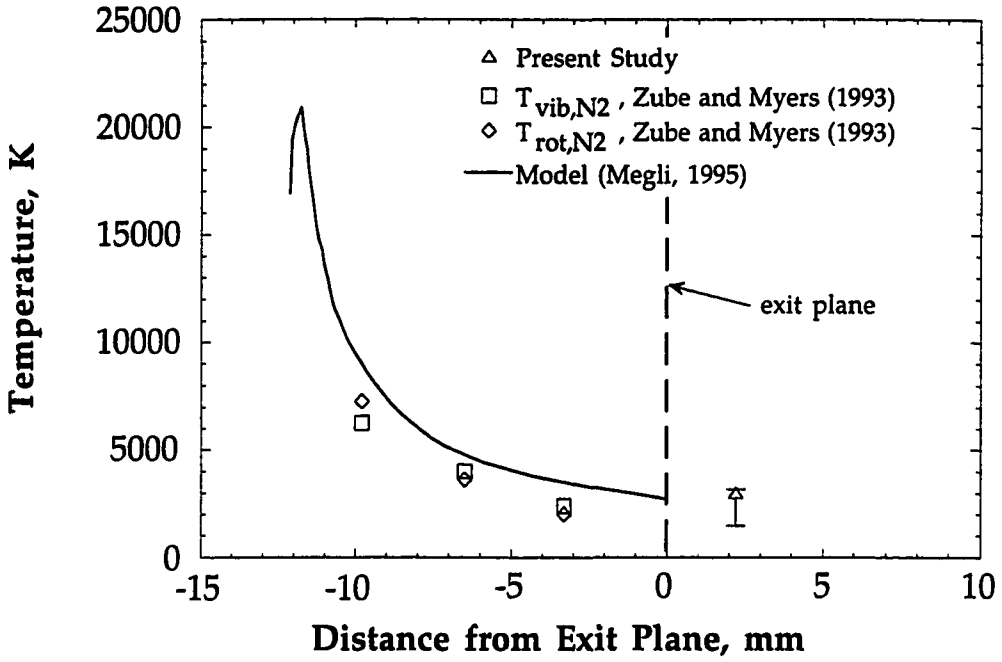

Fig. 6.5 Comparison of the gas temperature estimate of the present study with N_2 vibrational and rotational temperatures measured by Zube and Myers (1993) and the predictions of Megli (1995).

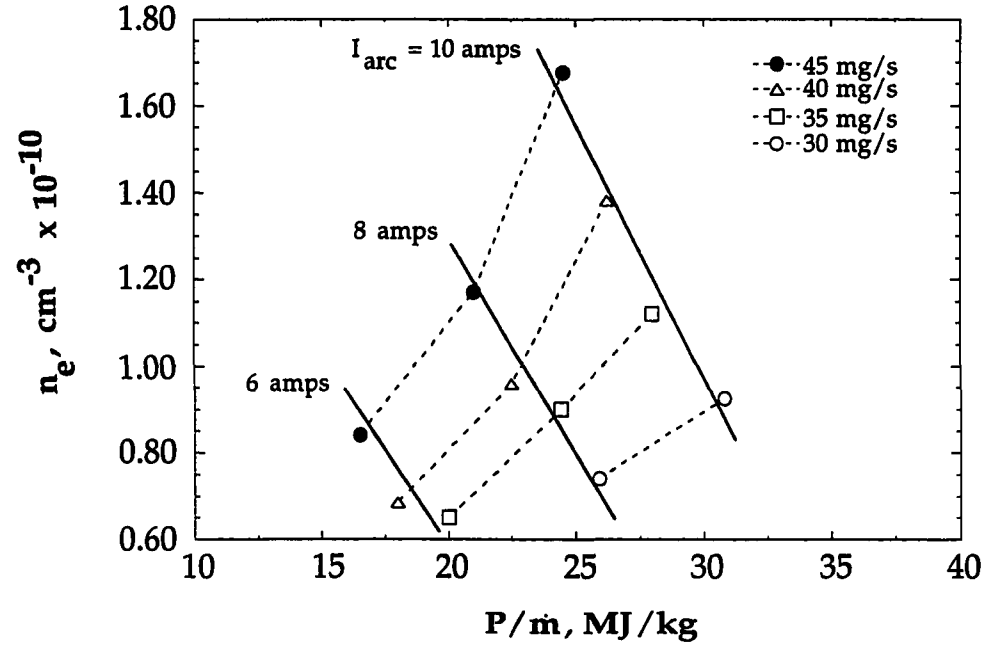

Fig. 6.6 Experimental results of Sankovic (1990) showing the variation of n_e (at x~10 cm) with thruster current and propellant flow rate. The trends indicated by these results are compared with the results of this work in section 6.1.2.

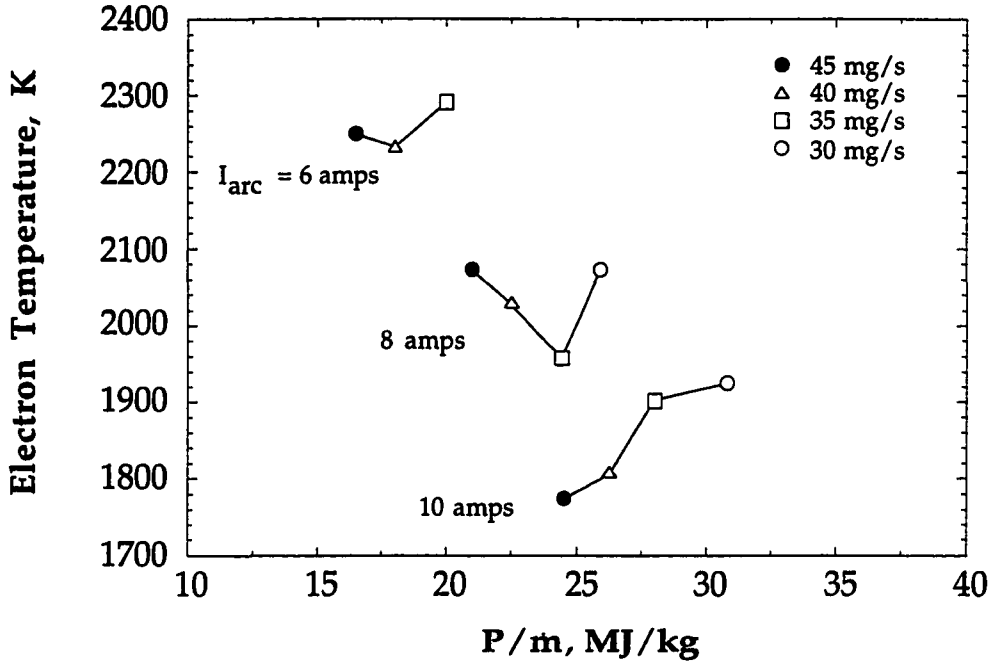

Fig. 6.7 Experimental results of Sankovic (1990) showing the variation of T_e (at x~ 10 cm) with thruster current and propellant flow rate. The trends indicated by these results are compared with the results of this work in section 6.1.2.

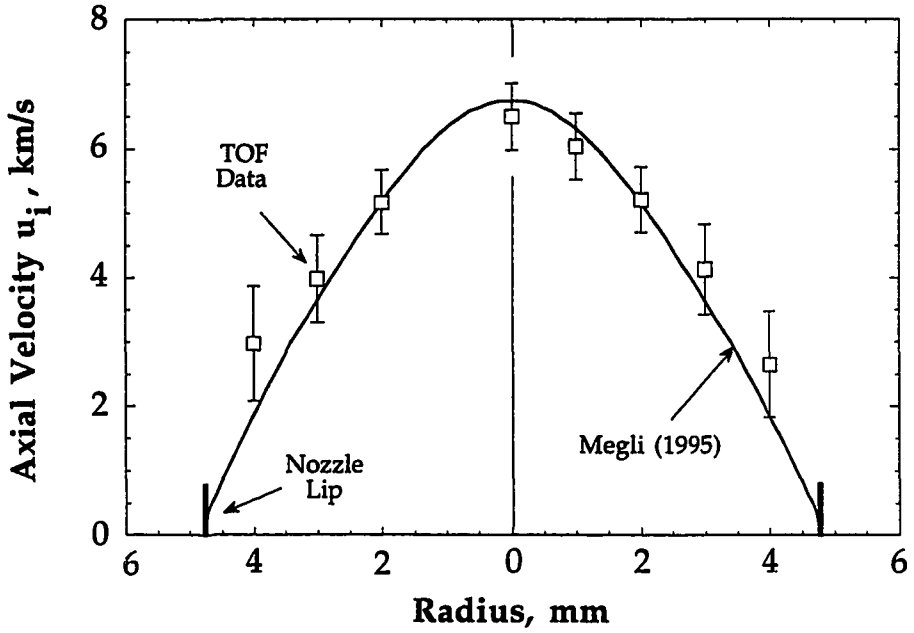

Fig. 6.8 Comparison of time-of-flight measurements of axial velocity with the numerical model predictions of Megli (1995) for the case of 10 amps and 50 mg/s $2H_2+N_2$ propellant.

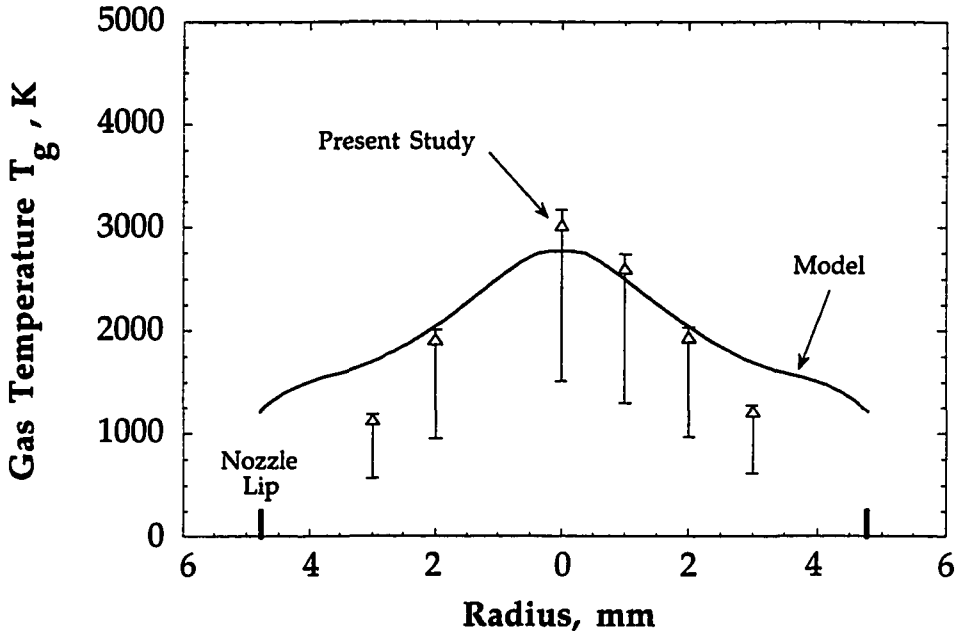

Fig. 6.9 Comparison of the gas temperature T_g estimates of this study with the numerical model predictions of Megli (1995) for the case of 10 amps and 50 mg/s $2H_2+N_2$ propellant.

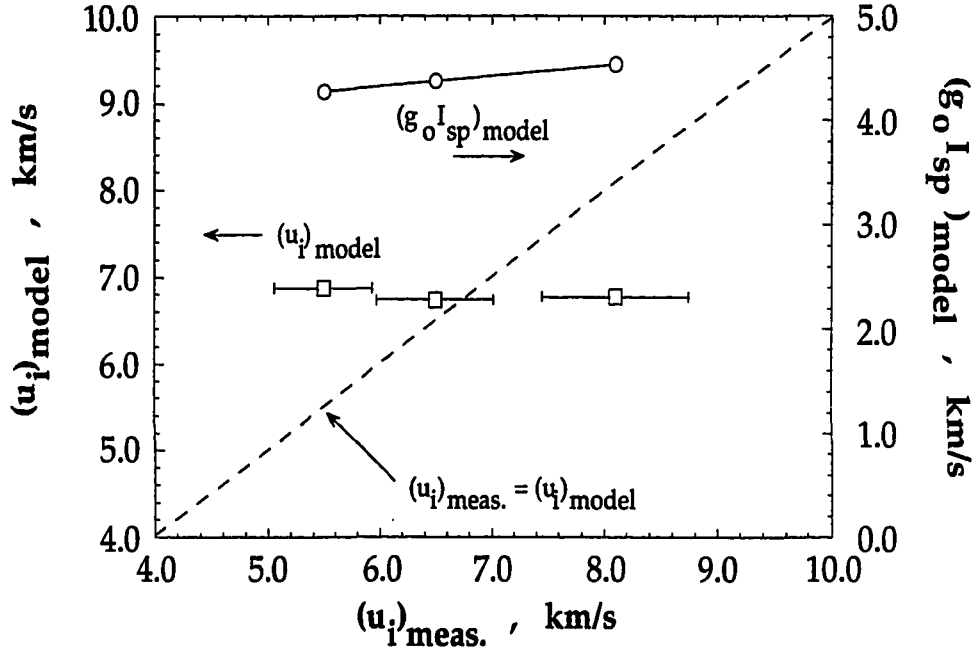

Fig. 6.10 Comparison of model predictions and TOF measurements of the plasma axial velocity u_i for the cases shown in Table 6.3. is also shown. The dashed line denotes agreement between $(u_i)_{model}$ and $(u_i)_{meas.}$.

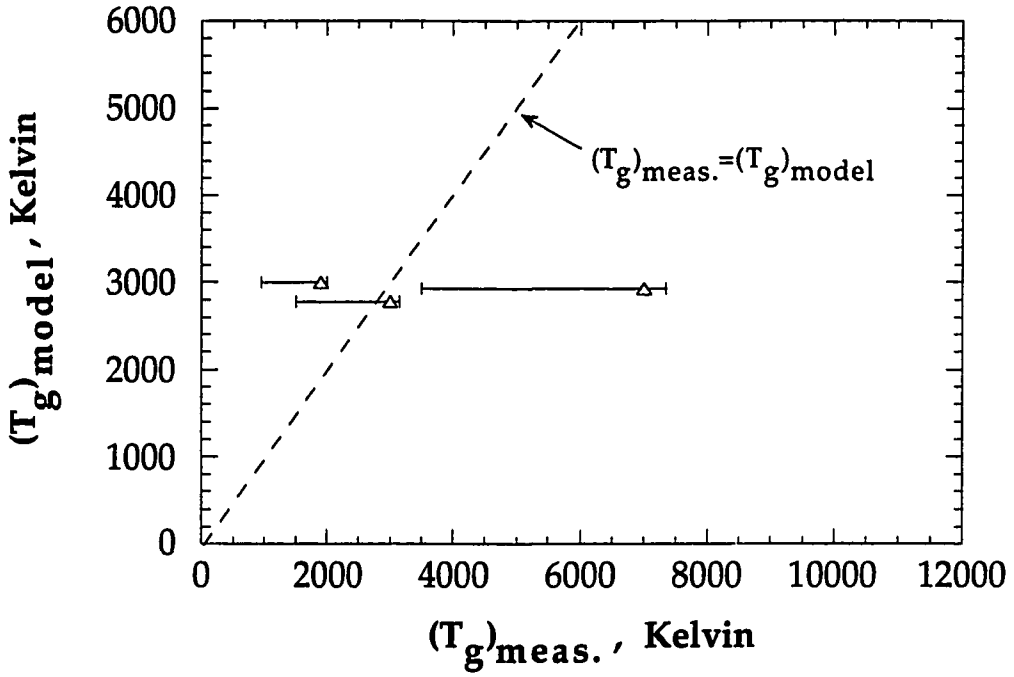

Fig. 6.11 Comparison of model predictions and experimental estimates of the gas temperature T_g for the cases shown in Table 6.3. The dased line denotes agreement between $(T_g)_{model}$ and $(T_g)_{meas.}$.

7. Summary and Conclusions

7.1 Summary

An experimental study of the near-field plume of a 1-kW constricted arcjet has been performed by making measurements with several types of electrostatic probes. The thruster used in this study was a NASA Lewis Research Center design and operated on a gaseous mixture of $2H_2+N_2$ to simulate fully decomposed hydrazine propellant. Various combinations of propellant flow rates and thruster arc currents were utilized so that the thruster operated with specific powers of 19.8, 22.4, and 26.0 MJ/kg.

The objectives of this study were: 1) Make experimental measurements for the purpose of validating the performance of a numerical arcjet model developed concurrently by Megli (1995), 2) Add to the very limited base of previous scientific research conducted on low-power *hydrazine* arcjets, and 3) Demonstrate the feasibility and utility of low-cost, robust plasma diagnostic techniques in the small geometries associated with low-power arcjets. These objectives were fulfilled through the development and implementation of the probing techniques highlighted below.

The quadruple electrostatic probe technique, which was originally developed by Burton, et al. (1993), was used to make simultaneous measurements of the electron temperature T_e, electron density n_e, and the ion speed ratio $u_i/c_{m,H^+}$. This technique was modified significantly for use in the present study. The modified approach allows the quadruple probe to be implemented in a multi-component (e.g., hydrogen-nitrogen) plasma in which there exists more than one species of positive ion. All previous uses of the quadruple (and triple) probes have been for single component plasmas.

Additionally, it was demonstrated that, unless accounted for, gradients in the plasma parameters could drastically convolute the measured data. In this study, the quadruple probe theory was modified to include the effects of radial gradients of T_e and n_e over the width of the probe. The theory was also revamped so that uncertainties in T_e and n_e due to the presence of the perpendicular electrode were eliminated. The quadruple probe was used to measure radial profiles of n_e, T_e, and $u_i/c_{m,H^+}$ at x=2.2 mm downstream of the thruster exit plane for a range of thruster operating conditions. Additionally, the axial profiles of centerline electron temperature and electron density were measured for 2.2<x<6.2 mm for the case of $P/\dot{m}$=22.4 MJ/kg. Independent single (Langmuir) and triple probe measurements verified the functionality of the quadruple probe techniques used in this study.

Two of the quadruple probe electrodes were also used in a double floating probe configuration to measure the radial electric field in the near-field plume plasma. Measurements of the electric field were used to estimate the fraction of the arcjet current at the thruster exit plane for the thruster operating at $P/\dot{m}$=22.4 MJ/kg.

A time-of-flight (TOF) electrostatic probe velocimetry technique, based on previous work by Pobst, et al. (1993, 1994), was developed and implemented in this study. The TOF probe was used to make spatially resolved measurements of the plasma axial velocities over a range of thruster operation. This approach resulted in radial profiles of the plasma axial velocity. Through the definition of the ion speed ratio, the TOF and quadruple probe results were combined to yield estimates of the gas temperature T_g.

Where previous experimental results existed, comparisons of the results of this study were made with those of previously published studies. Additionally, the results of a computational arcjet model (Megli, 1995) were compared with experimental results for the three thruster operating conditions here.

7.2 Conclusions

Through the course of this research, several plasma diagnostic techniques were developed or significantly adapted for use in the small geometries associated with low-power hydrazine arcjets. The performance of these techniques was favorable, demonstrating their utility in N-H plasmas of the type examined here.

The radial gradient quadruple probe model (section 4.2.3) is capable of capturing the effect of gradients in T_e and n_e over the width of the probe. While results of this analysis are convoluted by large uncertainties at locations far from the thruster centerline, the effect of passing the 1.4 mm wide probe through narrow radial T_e and n_e profiles has been demonstrated. A data reduction scheme has been demonstrated that can be utilized in any plasma in which radial gradients adversely affect the quadruple (or triple) probe response.

The measured *axial* gradients in T_e and n_e in the region $2.2<x<6.2$ mm indicate that the quadruple probe measurements represent a weighted average of these parameters along the 2.5 mm probe length. However, the axial gradients are slight enough in the region investigated so that they do not skew the quadruple probe results. The effect of gradients in the plasma potential V_p over the probe dimension has also been demonstrated. In the

region near the thruster centerline, it is concluded that these effects do not adversely influence the quadruple probe response.

The time-of-flight electrostatic probe technique for measuring plasma velocity has been demonstrated as a feasible method by which to make these measurements. However, the uncertainty of this technique is compromised for large radial locations in which the flow divergence of the plasma is difficult to estimate.

The accuracies of the experimental techniques utilized in this study have been demonstrated to be within acceptable limits. An exception is the large uncertainty in the estimate of the heavy particle temperature T_g, which is due to propagation of the uncertainties in other measured values. Areas in which these uncertainties can be improved are summarized in section 7.3 below.

Through the application of the diagnostic techniques described in this research, the scope of scientific data for the near-field plume region of the 1-kW hydrazine arcjet has been broadened. Based on the results of this work, the following experimental conclusions are made:

1) The electron temperature and electron density in the near-field plume are substantially influenced by the ripple inherent in the arcjet current supplied by the power processing unit (PPU) used in this study. Care must be taken, when using "switching" type power supplies, that the extent of the current ripple and its effects on T_e and n_e are understood and specified when reporting these values.

2) Quadruple probe measurements of the axial gradients in T_e and n_e over the range $2.2<x<6.2$ mm. show moderate gradients along the 2.5 mm

length of the quadruple probe in this region. The electron temperature varies from ~7000 K to ~3500 K over the 5 mm range of the measurements for the case $P/\dot{m}$=22.4 MJ/kg. The electron density varies only ~34% over this range, from 3.8 x 10^{12} cm^{-3} at x=2.2 mm to 2.5 x 10^{12} cm^{-3} at x=6.2 mm. However, a large gradient in n_e is indicated between x=2.2 mm (this study) and the nozzle interior (Zube and Myers, 1993), indicating an apparent sudden expansion in the flow as it crosses the thruster exit plane. The extent of this indicated axial gradient in n_e requires extra caution when measuring and reporting the locations of n_e measurements in this region.

3) Quadruple probe measurements of the radial profiles of T_e and n_e indicated that the electron temperature profile is nearly uniform at the centerline value and is much wider than the electron density radial profile.

4) Quadruple probe measurements of the ion speed ratio radial profile $u_i/c_{m,H^+}$ are very uniform over a majority of the thruster exit plane. These results, coupled with the measured axial velocity profiles, indicate a gas temperature profile that is peaked at the thruster centerline and roughly parabolic.

5) The T_e measurements and T_g estimates indicate a substantial thermal nonequilibrium with $T_e > T_g$ at the thruster exit for the three values of $P/\dot{m}$ investigated. For $P/\dot{m}$=19.8, 22.4, and 26.0 MJ/kg, the ratios of T_g/T_e were 0.3, 0.4, and 0.8. However, the uncertainties in the reported values of T_g, which are likely upper limits as discussed in section 5.3.5, are quite large at +5%/-50%.

6) The effects of varying thruster specific power on T_e, n_e, and u_i were also examined by varying the thruster current and the propellant mass flow rate $\dot{m}$. Decreasing $\dot{m}$ by ~17% had the effect of decreasing the measured exit plane n_e by ~24%. The measurement of T_e also decreased (by only 4%) with $\dot{m}$, but this change is well within the uncertainty of the measured probe quantity V_{d2}. In decreasing $\dot{m}$ from 50 to 45 mg/s and increasing I_{arc} from 10 to 11 amps (case 2-->3), the electron density increased ~23% while the electron temperature increased ~24%. Based on these results, it is apparent that the electron density at the exit plane varies with the propellant flow rate. However, conclusions regarding the dependence on n_e to changes in I_{arc} are difficult to draw. Little change in the electron temperature is noted with variation in $\dot{m}$. Given this fact, the substantial change in T_e between cases 2 and 3 indicates a dependence of the exit plane electron temperature primarily on the thruster current I_{arc}.

7) Estimates of the arc current near the thruster exit plane indicate that a small portion of the thruster current (~2%) may be crossing the exit plane and reattaching to the edge of the nozzle. These results indicate that the generally applied numerical model exit plane boundary condition of zero current may need reevaluation. As discussed in section 6.2, the additional ohmic heating due to the presence of this current may account for the discrepancy between experimentally measured and numerically predicted electron temperatures.

8) Measurements of plasma velocity near the thruster exit plane reveals smooth, approximately parabolic radial profiles of axial velocity. The measured centerline velocities increase substantially (5.5-8.0 km/s) with increases in $P/\dot{m}$ (19.8-26.0 MJ/kg). These results contrast the previous

experimental results of Curran and Haag (1992) that indicate only moderate increases in I_{sp} occur with these increases in $P/\dot{m}$. These results are consistent, however, with the trend that the centerline *gas* density decreases with increasing $P/\dot{m}$. These results agree with the trend of increasing gas temperature T_g with $P/\dot{m}$ noted in the present study.

7.3 Recommendations for Future Work

Despite the simplicity and feasibility of the probing techniques used in this study, their utility can occasionally be somewhat limited. In addition, the results of this work have raised several questions regarding arcjet performance that may warrant further investigation. Based on experiences and knowledge gained through the course of this research, the following recommendations for future consideration are offered:

1) The quadruple probe technique used in this study functions well in the region of the plume in which it was utilized ($2.2<x<6.2$ mm). However, probe measurements are not possible closer to the thruster exit plane due to geometric limits on the probe size and location. As such the large n_e gradients, between the x=2.2 mm and the thruster exit plane, compromise the ability of the quadruple probe to make measurements for the purpose of validating numerical model predictions of exit plane densities. A detailed investigation of the axial n_e gradient in this region of the plume is recommended, perhaps via a spectroscopic technique that affords a much better spatial resolution. This work would quantify the extent, and perhaps explain the source, of the large axial n_e gradient in this region.

2) The axial velocity results of this study, along with the I_{sp} data of previous researchers, indicates that the gas density radial distribution may change substantially with $P/\dot{m}$ as discussed above. The diagnostics used in this study were not capable of measuring heavy particle densities. An experimental investigation of this parameter is recommended.

3) The uncertainties in the TOF probe axial velocity results were less than ± 10% for measurements made within r<2 mm. For measurements farther from the thruster centerline, uncertainties were much larger due to the possibility of misalignment between the TOF probe axis and the flow vector. These uncertainties can be substantially decreased via measurements of the flow divergence angle across the thruster exit. An experimental investigation of the flow divergence in the near-field plume, perhaps using rotating single electrostatic probes, is recommended. The time-of-flight technique can be further improved by decreasing the axial length of the probe. This will improve the axial spatial resolution of the technique. Additionally, since the frontal area of the probe is increased as it rotates, decreasing the axial length would also improve the radial resolution of the probe. Of course, changes in the probe electrode axial separation must be weighed against the magnitude of the measured convective time delay and the temporal resolution of the data acquisition system used to record the probe signals.

4) In the present study, an educated estimate of the plasma ion composition factor f ($=n_{H+}/n_e$) was made. This assumption introduced no added uncertainty to measurements of T_e and only minor uncertainty to the experimental determination of n_e. Additionally, measurements of the plasma axial velocity were unaffected by the selection of the factor f.

However, measurements of $u_i/c_{m,H^+}$ and, hence, the estimated values of T_g were strongly influenced by the value assumed for n_{H^+}/n_e through the implementation of the crossed probe technique. A better understanding of this factor is recommended if the crossed probe technique is to be applied to plasmas in which multiple species of positive ions are present.

5) The evaluation of the extent of thermal nonequilibrium (T_g/T_e) in this study was compromised by the large experimental uncertainty in the gas temperature T_g. Additional measurements of the gas temperature, through an independent means which possesses a more manageable uncertainty, is recommended. Laser Induced Fluorescence (LIF) measurements are frequently used for this purpose with hydrogen arcjets, but have not been applied to low-power hydrazine arcjets.

References

Bohm, D, Burhop, E. H. S. and Massey, H. S. W., The Characteristics of Electrical Discharges in Magnetic Fields, edited by Guthrie, A. and Wakerling, R. K., McGraw-Hill, New York, 1949.

Bufton, S. A., Burton, R. L. and Krier H., "Measured Plasma Properties at the Exit Plane of a 1-kW Arcjet," AIAA Paper 95-3066, July 1995.

Burtner, D., Keefer, D. and Ruyten, W., "Experimental and Numerical Studies of a Low-Power Arcjet Operated on Simulated Ammonia," AIAA Paper 94-2869, June 1994.

Burton, R. L., DelMedico, S. G. and Andrews, J. C., "Application of a Quadruple Probe Technique to MPD Thruster Plume Measurements," *Journal of Propulsion and Power*, Vol. 9, No. 5, pp. 771-777, 1993.

Burton, R. L., Bufton, S. A., Tiliakos, N. T. and Krier, H., "Application of Multiple Electrostatic Probes to a Low Power Arcjet," AIAA Paper 94-3299, June 1994.

Burton, R. L., personal communication, 1994.

Burton, R. L., Bufton, S. A. and Krier, H., "Exit-Plane Electrostatic Probe Measurements of a Low-Power Arcjet," Submitted to *Journal of Propulsion and Power*, October, 1995.

Butler, G. W., Cassady, R. J. and King, D. Q., "Directions for Arcjet Technology Development," AIAA Paper 94-2652, June 1994.

Carney, L. M. and Sankovic, J. M., "The Effects of Arcjet Operating Condition and Constrictor Geometry on the Plasma Plume," AIAA Paper 89-2723, July 1989.

Carney, L. M. and Keith, T. G., "Langmuir Probe Measurements of an Arcjet Exhaust," *Journal of Propulsion and Power*, Vol. 5, No. 3, pp. 287-294, 1989.

Chen, S.-L. and Sekiguchi, T., "Instantaneous Direct-Display System of Plasma Parameters by Means of Triple Probe," *Journal of Applied Physics*, Vol. 36, No. 8, pp. 2363-2375, 1965.

Chung, P. M., Talbot, L. and Touryan, K. J., Electric Probes in Stationary and Flowing Plasmas: Theory and Application, Springer-Verlag, 1975.

Curran, F. M., Manzella, D. H. and Pencil, E. J., "Performance Characterization of a Segmented Anode Arcjet Thruster," AIAA Paper, 90-2582, (also NASA TM-103227), July 1990.

Curran, F. M. and Haag, T. W., "Extended Life and Performance Test of a Low-Power Arcjet," *Journal of Spacecraft and Rockets*, Vol. 29, No. 4, pp. 444-452, 1992.

DelMedico, S. G., Plasma Flow Measurements by a Quadruple Probe in a Quasi-Steady MPD Plasma, M.S. Thesis, University of Illinois, 1992.

Gallimore, A. D., Kelly, A. J. and Jahn, R. G., "Anode Power Deposition in Quasisteady Magnetoplasmadynamic Thrusters," *Journal of Propulsion and Power*, Vol. 8, No. 6, pp. 1224-1231, 1992.

Gallimore, A. D., Kim, S.-W., Foster, J. E., King, L. B., and Gulczinski, F. S., "Near and Far-field Plume Studies of a 1-kW Arcjet," AIAA Paper 94-3137, June 1994.

Golz, T. M., Auweter-Kurtz, M., Habiger, H. and Kurtz, H. L., "High Specific Impulse Performance of a 100 kW Radiation Cooled Thermal Arcjet Thruster," AIAA Paper 94-3249, June 1994.

Griem, H. R., Plasma Spectroscopy, Mcgraw-Hill, New York, 1964.

Habiger, H. A., Auweter-Kurtz, M. and Kurtz, H., "Electrostatic Probes for the Investigation of Arc-Driven Electric Propulsion Devices," *Proceedings of the 23rd International Electric Propulsion Conference*, Seattle, WA, pp. 1137-1147, 1993.

Habiger, H. A., Auweter-Kurtz, M. and Kurtz, H., "Investigation of Arc Jet Plumes with Fabry-Perot Interferometry," AIAA Paper 94-3300, June 1994.

Hoell, J. M. , Burlock, J. and Jarrett, O. , "Velocity and Thrust Measurements in a Quasi-Steady Magnetoplasmadynamic Thruster," *AIAA Journal*, Vol. 9, No. 10, pp. 1969-1974, 1971.

Hargus, W., Micci, M. and Spores, R., "Interior Spectroscopic Investigation of the Propellant Energy Modes in an Arcjet Nozzle," AIAA Paper 94-3302, June 1994.

Hutchinson, I. H., Principles of Plasma Diagnostics, Cambridge University Press, 1987.

Jack, J. R., "Theoretical Performance of Propellants Suitable for Electrothermal Jet Engines," NASA TN D-682, March 1961.

Jahn, R. G., Physics of Electric Propulsion, McGraw-Hill Series in Missile and Space Technology, McGraw-Hill, New York, 1968.

Johnson, B. H. and Murphree, D. L., "Plasma Velocity Determination by Electrostatic Probes," *AIAA Journal*, Vol. 7, No. 10, pp. 2028-2030, 1969.

Kanal, M., "Theory of Current Collection of Moving Cylindrical Probes," *Journal of Applied Physics*, Vol. 35, No. 6, pp. 1697-1703, 1964.

Keefer, D., Moeller, T. and Rhodes, R., "Multiplexed Laser-Induced Fluorescence and Nonequilibrium Processes in Arcjets," AIAA Paper 94-2656, June 1994.

Kushner, M. J., personal communication, 1994.

Langmuir, I. and Mott-Smith, H. M., "The Theory of Collectors in Gaseous Discharges," *Physical Review*, Vol. 28, pp. 727-763, 1926.

Liebeskind, J. G., Hanson, R. K. and Cappelli, M. A., "Flow Diagnostics of an Arcjet Using Laser-Induced Fluorescence," AIAA Paper 92-3243, July 1992.

Liebeskind, J. G., Hanson, R. K. and Cappelli, M. A., "Experimental Investigation of Velocity Slip Near an Arcjet Exit Plane," *AIAA Journal*, Vol. 33, No. 2, pp. 373-375, 1995.

Manzella, D. H., Curran, F. M., Myers, R. M. and Zube, D. M., "Preliminary Plume Characteristics of an Arcjet Thruster," AIAA Paper 90-2645, July 1990.

Megli, T. W., Krier, H., Burton, R. L., and Mertogul, A. E., "Two Temperature Modeling of N_2/H_2 Arcjets," AIAA Paper 94-2413, June 1994.

Megli, T. W., Krier, H. and Burton, R. L., "A Plasmadynamics Model for Nonequilibrium Processes in N_2/H_2 Arcjets," AIAA Paper 95-1961, June 1995.

Megli, T. M., A Nonequilibrium Plasmadynamics Model for Nitrogen/ Hydrogen Arcjets, Ph.D. Thesis, University of Illinois, 1995.

Miller, S. A., Multifluid Nonequilibrium Simulation of Arcjet Thrusters, Ph.D. Thesis, Massachusetts Institute of Technology, 1994.

Nachtrieb, R. T., "Application of the Saha Equation to High Temperature (>6000 K) Rocket Exhaust," Phillips Laboratory, PL-TR-92-3042, Edwards AFB, Jan. 1993.

Ohler, S. Gilchrist, B. and Gallimore, A., "Non-Intrusive Plasma Diagnostics for Electric Propulsion Research," AIAA Paper 94-3297, June 1994.

Paccani, G., "Electrostatic Probe Diagnostics of Solid Propellant MPD Thruster Jets," AIAA Paper 94-3340, June 1994.

Pivirotto, T. J., "Velocity and Atom Temperature Distribution Measurement in Arcjet Engine Plumes," *Proceedings for the Arcjet Plume Diagnostics Technical Workshop*, Pasadena, CA, pp. 179-190, 1986.

Pobst, J. A., Schilling, J. H., Erwin, D. A. and Spores, R. A., "Time Resolved Measurements of 1-kW Arcjet Plumes using Current Modulation Velocimetry and Triple Langmuir Probes," *Proceedings of the 23rd International Electric Propulsion Conference*, Seattle, WA, pp. 1177-1184, 1993.

Pobst, J. A., Schilling, J. H., Lutfy, F. M., Erwin, D. A. and Spores, R. A., "Arcjet Diagnostics using Current Modulation Velocimetry and Pulsed Electron Beam Fluorescence," AIAA Paper 94-2742, June 1994.

Pobst, J. A., Wysong, I. J. and Spores, R. A., "Laser Induced Fluorescence of Ground State Hydrogen Atoms at the Nozzle Exit of an Arcjet Thruster," AIAA Paper 95-1973, June 1995a.

Pobst, J. A., Wysong, I. J. and Spores, R. A., "Laser Induced Fluorescence of Ground State Hydrogen Atoms in an Arcjet Plume," International Electric Propulsion Conference Paper 95-28, Sept. 1995b.

Poissant, G. and Dudeck, M., "Velocity Profiles in a Rarefied Argon Plasma Stream by Crossed Electrostatic Probes," *Journal of Applied Physics*, Vol. 58, No. 5, pp. 1772-1779, 1985.

Ruyten, W. M., Burtner, D. and Keefer, D., "Spectroscopic Investigation of a Low-Power Arcjet Plume," AIAA Paper 93-1790, June 1993.

Sankovic, J. M., "Investigation of the Arcjet Plume Near Field Using Electrostatic Probes," NASA TM-103638, Nov. 1990.

Sankovic, J. and Jankovsky, R., "An Experimental Investigation of the Effective Current Collecting Area of a Spherical Langmuir Probe in an Arcjet Thruster Exhaust," AIAA Paper 90-0073, Jan. 1990.

Schott, L., "Electrical Probes," in Plasma Diagnostics, edited by W. Lochte-Holtgreven, John Wiley and Sons, New York, pp. 671-673, 1968.

Spores, R. A., Pobst, J. A., Schilling, J. H. and Erwin, D. A., "Performance Effects of Interaction Between a Low-Power Arcjet and its Power Processing Unit," AIAA Paper 92-3238, July 1992.

Storm, P.V. and Cappelli, M. A., "Axial Emission Measurements on a Medium Power Hydrogen Arcjet Thruster," AIAA Paper 94-2743, June 1994.

Storm, P.V. and Cappelli, M. A., "Laser-Induced Fluorescence Measurements Within an Arcjet Thruster Nozzle," AIAA Paper 95-2381, June 1995.

Sutton, G. P., Rocket Propulsion Elements, Fifth Edition, John Wiley and Sons, Inc., 1986.

Swift, J. D. and Schwar, M. J. R., Electrical Probes for Plasma Diagnostics, American Elsevier Publishing Company, Inc., New York, 1969.

Szuszczewicz, E. P. and Holmes, J. C., "Surface Contamination of Active Electrodes in Plasmas: Distortion of Conventional Langmuir Probe Measurements," *Journal of Applied Physics*, Vol. 46, No. 12, pp.5134-5136, 1975.

Tiliakos, N. T., Burton, R. L. and Krier, H., "Application of Internal Langmuir Diagnostics for Arcjets," AIAA Paper 95-2386, July 1995.

Tilley, D. L., Kelly, A. J. and Jahn, R. G., "The Application of the Triple Probe Method to MPD Thruster Plumes," AIAA Paper 90-2667, July 1990.

Tilley, D. L., Gallimore, A. D., Kelley, A. J. and Jahn, R. G., "The Adverse Effect of Perpendicular Ion Drift Flow on Cylindrical Triple Probe Electron Temperature Measurements," *Rev. Sci. Instrum.*, Vol. 65, No. 3, pp. 678-681, 1994.

Wilbur, P. J., Jahn, R. G. and Curran, F. C., "Space Electric Propulsion Plasmas," IEEE Transactions on Plasma Science, Vol. 19, No. 6, pp. 1167-1179, 1991.

Zube, D. M., and Myers, R. M., "Techniques for Spectroscopic Measurements in an Arcjet Nozzle," *Journal of Propulsion and Power*, Vol. 8, No. 1, pp. 254-256, 1992.

Zube, D. M., and Myers, R. M., "Thermal Nonequilibrium in a Low-Power Arcjet Nozzle," *Journal of Propulsion and Power*, Vol. 9, No. 4, pp. 545-552, 1993.

Zube, D. M. and Auweter-Kurtz,. M., "Spectroscopic Arcjet Diagnostic Under Thermal Equilibrium and Nonequilibrium Conditions," AIAA Paper 93-1792, June 1993.

Zube, D. M. and Messerschmid, E. W., "Spectroscopic Temperature and Density Measurements in a Low Power Arcjet Plume," AIAA Paper 94-2744, June 1994.

Vita

Scott Allen Bufton was born in Beloit, Wisconsin on March 14, 1966, the first child of Richard L. and Ardis L. Bufton. He was raised with his brother Steve and sister Sheri in Machesney Park, near Rockford, Illinois. He attended Harlem Senior High School and graduated sixth in his class in 1984. He then enrolled in mechanical engineering at the University of Illinois at Urbana-Champaign. In May of 1988, he received a Bachelor of Science degree in mechanical engineering with high honors. Scott continued his education at the University of Illinois by pursuing graduate degrees in mechanical engineering. During his M.S. work, he held the DuPont University Science and Engineering Grant for two years and was supported as a teaching assistant. As a result of his teaching experience, Scott was named on several occasions to the "Incomplete List of Instructors Ranked as Excellent by their Students." In August of 1992, he completed an experimental thesis in the area of two-phase turbulent flow under the guidance of Professor B. G. Jones and was awarded the Master of Science degree in mechanical engineering. Scott continued his graduate studies at the University of Illinois as a doctoral candidate working with Professors R. L. Burton and H. Krier in the area of electric propulsion. His dissertation work consists of plasma diagnostics studies of a low-power arcjet thruster for satellite maneuvering applications. During his work in this area, he has been supported as a research assistant with funding from the Air Force Office of Scientific Research. On one of his finest days, he was married to Tara Elizabeth Lopez on December 31, 1993. Scott has accepted a position as a Research Engineer, and will join the technical staff at Exxon Production Research Company in Houston, Texas upon completion of his Ph.D.